UNIVERSITAT POLITÈCNICA DE CATALUNYA
BARCELONATECH
Escola Superior d'Enginyeries Industrial,
Aeroespacial i Audiovisual de Terrassa

School of Industrial, Aerospace and Audiovisual Engineering
of Terrassa (ESEIAAT)

Study of the boundary layer flow control using synthetic jets by means of spectro-consistent discretizations

Final Master's Degree Project

Author: David Duran Pérez

Advisors: Dr. Ivette Maria Rodríguez Pérez & Dr. Manel Soria Guerrero

Master's Degree in Aerospace Engineering

June 20, 2017 - Spring 2017 Call

Barcelona, Spain

This page intentionally left blank

To my dear family

Contents

List of Tables

List of Figures

Abstract

This report presents a study of the interaction of AFC (specifically, synthetic jets) with the laminar boundary layer of a NACA 0012 airfoil.

First of all, in order to understand the phenomenology of Navier-Stokes equations, a spectro-consistent Computational Fluid Dynamics (CFD) code has been developed from scratch. By using a spectro-consistent discretization, the fundamental symmetry properties of the underlying differential operators are preserved. This code also helps to understand how the energy is transported from big to small scales.

After solving a paradigmatic problem (TGV) using the aforementioned code, a mature CFD code (*Alya*) is used to simulate the flow around the NACA 0012 airfoil. *Alya* software also uses a spectro-consistent code but in Finite Element Method (FEM).

Once the reference cases are solved for different angles of attack, a boundary condition representing an idealized synthetic jet is implemented. A systematic parametrization of the synthetic jet has been performed in order to assess the level of flow control in the boundary layer.

Results demonstrate that, by selecting a correct combination of actuator frequency and momentum coefficient, the lift coefficient increases while the drag coefficient decreases producing a better lift-to-drag ratio. This aerodynamic improvement implies that a better circulation control is achieved, less noise is produced and less fuel consumption is required.

It is also worth noting that, for high angles of attack, it is necessary to perform 3D flow simulations in order to capture the entire physics of the problem.

Glossary

This list presents the definition of the most important terms used during this report. Some of the definitions have been obtained from CFD Online web. These cases have a cross-reference to reference [4].

Dirichlet A Dirichlet boundary condition imposes the value of the solution on a specific boundary. 31

Incompressible flow [4] A flow is said to be incompressible if the density of a fluid element does not change during its motion. It is a property of the flow and not of the fluid. The flow is incompressible if the divergence of the velocity field is identically zero. 8, III

Laminar flow An ordered and smooth flow that occurs when a fluid flows in parallel layers. Laminar flows have a high momentum diffusion and low momentum convection. 77

Neumann A Neumann boundary condition imposes a differential equation on a specific boundary 31

Periodic problem A periodic problem is one dealing with a velocity distribution that repeats its values in regular intervals that coincide with the boundaries of the problem. 10

Staggered grid [4] On a staggered grid, the scalar variables (pressure, density, total enthalpy...) are stored in the cell centers of the control volumes, whereas the velocity or momentum variables are located at the cell faces. 10

Streamline [4] A line in the fluid whose tangent is everywhere parallel to the local velocity vector (u, v, w) instantaneously is a streamline. Streamlines cannot intersect since the velocity at any point is unique. 40, 60

Acronyms

AFC Active Flow Control vi, viii, 1, 3, 4, 5, 6, 42, 51, 60, 61, 62, 63, 76, 79

AOA Angle Of Attack 33

BSC Barcelona Supercomputing Center 1, 32

CFD Computational Fluid Dynamics viii, 1, 10, 26, 79

CV Control Volume 10, 11, 12, 17

DOF Degree Of Freedom 3, 24, 25, 38, 47

FEM Finite Element Method viii

NS Navier-Stokes 1, 8, 9, 10, VIII

RMSE Root Mean Squared Error 16, 17, 22

TGV Taylor-Green Vortices v, viii, 3, 17, 18, 23, 26

TU Time Unit 24

TUAREG Turbulence And Aerodynamics In Mechanical And Aerospace Engineering Research Group 1, 32, 71

UPC Universitat Politècnica De Catalunya 1, 32, 71

WBS Work Breakdown Structure 66

Nomenclature

In this section, the most important variables used throughout the report are defined.

u_i	Component *i* of velocity (m/s)
$\boldsymbol{u}$	Discretized velocity vector (m/s)
x_i	Component *i* of position (m)
p	Pressure (Pa)
$\boldsymbol{p}$	Discretized pressure vector (Pa)
ν	Kinematic viscosity (m^2/s)
$\mathbb{S}$	Source term
ρ	Density (kg/m^3)
t	Time (s)
Ω	Volume of the control volumes (m^3)
$C(\boldsymbol{u})$	Convection operator
D	Diffusion operator
G	Gradient matrix
M	Divergence matrix
L	Laplacian matrix
μ	Dynamic viscosity $(Pa \cdot s)$
S	Surface (m^2)
δ	Distance between two mesh nodes (m)
λ	Eigenvalues
Q	Fourier transformation
N	Number of control volumes in a given direction
Δ	Spacing of the grid in a given direction (m)
CFL	Courant-Friedrich-Levy condition
E_k	Total kinetic energy (m^2/s^2)
ϵ	Kinetic energy dissipation rate (m^2/s^3)
$\vec{\omega}$	Vorticity $(1/s)$
ε	Enstrophy $(1/s^2)$
α	Angle of attack (deg)
AOA	Angle of attack (deg)
Re	Reynolds number (-)
L	Lift (N)
C_l	2D Lift coefficient (-)
$C_{l_{rms}}$	2D RMS lift coefficient (-)
D	Drag (N)
C_d	2D Drag coefficient (-)
$C_{d_{rms}}$	2D RMS drag coefficient (-)
U_∞	Free-stream velocity (m/s)
c	Airfoil chord (m)
St	Strouhal number (-)
f	Frequency (Hz)
F^+	Dimensionless frequency (-)
C_μ	Momentum coefficient (-)
p_0	Reference pressure (Pa)
x_{te}/c	Distance to the trailing edge (-)
x_{le}/c	Distance to the leading edge (-)
h/c	Actuator width (-)

Chapter 1: Introduction

In this section, the problem to be solved in this project is presented by defining its objectives and justification. The scope and specifications of the thesis are also detailed.

1.1 Objective

Synthetic jets have emerged as fluid devices for active control boundary layer separation and turbulence. The aim of this project is to study the interaction of a modeled synthetic jet with the laminar boundary layer of a NACA 0012 airfoil. The main goals of the study are:

- Numerical simulations of synthetic jets into a laminar boundary layer.
- Perform a systematic parametrization of the synthetic jet in order to characterize the level of flow control in the boundary layer.

In order to achieve these objective, the first step is to completely understand the incompressible Navier-Stokes equations by implementing a spectro-consistent CFD code from scratch. This code also helps to understand in a better way how the energy is transported from big scales to small ones.

Although the implemented CFD code is really useful to understand the basic concepts behind Navier-Stokes (NS) equations, it does not enable to solve the NACA 0012 airfoil simulations since only uniform staggered orthogonal meshes are permitted. To do so, a mature code developed through several years is necessary: *Alya* software (developed at Barcelona Supercomputing Center (BSC) [5]). The usage permission of this code has been granted due to an agreement between the *Alya* development team and the Turbulence and aerodynamics in mechanical and aerospace engineering research Group (TUAREG) (Universitat Politècnica de Catalunya (UPC)).

1.2 Scope

The activities developed to achieve the main aim of this project are:

- Brief literature review on AFC in boundary layers.
- Study of the Navier-Stokes equations.

- Implementation of a spectro-consistent CFD code.
- Definition of the cases to be considered. Definition of the boundary conditions, number of jets, initial conditions, period...
- Numerical resolution of the simulations without Active Flow Control. Mesh refinement study. Analysis of the results.
- Numerical resolution of the simulations with Active Flow Control using the knowledge from previous results.
- Analysis of the results and main conclusions.

1.3 Requirements and specifications

The basic specifications and hypothesis of this study are summarized below:

- Incompressible Navier-Stokes equations are used. No compressibility effects are foreseen.
- No turbulence model is applied to the simulations.
- Most part of the simulations of this study are restricted to 2D. The self-designed code can perform 3D simulations (such as Taylor-Green vortices), but only with uniform staggered orthogonal meshes. However, for the simulations of the NACA 0012 airfoil, both unstructured 2D and 3D meshes have been used.
- The Reynolds number is set to 5,000 in all simulations.
- The study is limited to the NACA 0012 airfoil.
- The geometry of the synthetic jet is not included in the simulations. The synthetic jet is set by imposing a boundary condition.

In order to make clear which code has been developed by the author, all the software that has been used during this project can be seen in Table 1.1, where the author is specified.

Scripts, codes and tools that have been developed by the author could be provided in a separate folder if required.

Software description	Author(s)	Where used?
Spectro-consistent CFD code	The author (David Duran)	Fist half of the project: TGV simulations
Vanilla CFD code in C	Dr. Manel Soria Guerrero (+ some modifications by the author)	To obtain 128 and 256 Degree of Freedoms (DOFs) TGV simulations
Alya CFD software	*Alya* development team	NACA 0012 airfoil simulations
ICEM meshing	ANSYS	Development of NACA 0012 airfoil meshes
Converter ICEM-Alya	Dr. Manel Soria Guerrero	To convert ICEM meshes to Alya format
NACA auto-generator meshing	Dr. Manel Soria Guerrero and Engr. Arnau Miró	To automatically generate meshes for NACA airfoils
Postprocessing scripts	The author (David Duran)	Postprocess the NACA 0012 airfoil simulations
Paraview	Paraview development team	Postprocessing

Table 1.1: Software used during this project

1.4 Justification of the project

Active Flow Control research projects have dramatically increased over the last decades. This type of flow control has several advantages such as drag reduction and lift enhancement. Circulation control is also a fundamental benefit of the usage of this technology, which enables to delay the transition to turbulent flow. As commented in chapter 9, all these advantages produce a positive impact on the environment.

AFC is still a novel technology and more studies are required to consolidate it for real-world applications. Most of the studies have been performed on airfoils with a trailing edge stall and at high Reynolds ($Re > 10^5$). The main objective of this

project is to contribute to the advance of active flow control by simulating one of its available technologies: synthetic jets at a low Reynolds number ($Re = 5,000$). This Reynolds number is of special interest for Mars missions because of the severe restrictions on size and weight, and the low density of the atmosphere [6]. Moreover, an advantage of this Re is that it does not require so much computational power as higher Reynolds numbers.

To achieve the objective of contributing to the advance of AFC, numerical simulations analyzing the effect of active flow control on laminar boundary layer are performed. It is also fundamental to completely understand the incompressible Navier-Stokes equations prior running all the required simulations.

Chapter 2: Literature review on Active Flow Control

The field of AFC has experimented a dramatic growth in the recent years, specially in the aeronautic field (despite being a multidisciplinary field). Active flow control consists of techniques in which energy is actively expended to modify the flow around a specific surface. It has the potential to significantly change the lift and drag of an airfoil [7]. Some of the advantages of AFC are:

- Lift enhancement
- To delay transition to turbulent flow
- Circulation control
- Drag reduction
- To maneuver without control surface deflection
- To achieve a minimum radar cross-section
- To reduce mechanical complexity
- To reduce noise and weight

Despite the aforementioned advantages and the recent interest on this field, the number of instances in which active flow control has successfully transitioned from a laboratory prototype, such as the one described in [8] and [9], to a real-world application is small. Some of the reasons that could explain this is that the aerospace industry is really conservative besides the fact that most control techniques require large amounts of power.

However, although passive technologies offer simplicity on non-critical conditions, active flow control enables optimization at off-design conditions or when it is necessary to react to rapidly changing flow conditions [10]. As discussed in reference [11], it is a 'cost-effective technology that has the potential for revolutionary advances in aerodynamic performance and maneuvering compared to conventional approaches' (traditional control surfaces or spoilers).

One example of this off-design condition is when an engine failure occurs during takeoff or at low speed climb. In order to overcome this instance, bigger vertical tails than necessary for cruise are installed on the aircraft. J.C.Lin et al. [12] have

studied that implementing a rudder with AFC would delay flow separation over a highly deflected rudder. This rudder with AFC would produce an increase of side force, which would allow a smaller vertical tail and a more efficient aircraft during the whole flight. Only more energy would be consumed in the rare event of an engine failure during takeoff.

AFC varies from brute-force techniques (based on the amplitude) to more efficient approaches that seek to leverage flow instabilities using small-amplitude perturbations [1]. These latest approaches are smarter but it is worth noting that Gilarranz et al. [8] have observed a weak dependency on frequency for angles of attack less than 10 degrees.

In order to simulate synthetic jets (a type of active flow control), You & Moin [13] apply a sinusoidal velocity boundary condition to the cavity side wall depending on the angle of attack α:

$$(u, v, w) = A_p \sin(2\pi f t) U_\infty [\cos\alpha, -\sin\alpha, 0] \tag{2.0.1}$$

An important parameter is the amplitude, which comes from the momentum coefficient. Mccormick [14] shows that, to have a positive effect on the lift coefficient, the momentum coefficient must be at least 0.002 for a $Re = 5 \times 10^5$. A similar study has been carried out in this project with similar results.

In general (i.e. [7]), placing actuators (jets) very near the airfoil leading edge on the suction surface has performance benefits. A significant increase in lift and decrease in drag are achieved. Obviously, these performance improvements depend on the Reynolds number and compressibility effects, as Seifert and G. Pack show in [15].

Several research activities at NASA have been carried out related to AFC [10]. The aims of these activities are to protect the environment, increase mobility, explore new aerospace mission and reduce aircraft noise and emissions.

NASA has also carried out an exhaustive study of synthetic jet actuators for active flow control [11]. Several actuators have been analyzed with important findings such as the maximum achieved jet velocities or the required momentum coefficient to be applied in order to be effective.

There are various types of actuators for AFC. In Figure 2.1, a useful classification from reference [1] is given. The most common type of actuator is **fluidic**, whose primary function is to inject fluid without having moving parts. **Moving body** actuators have the purpose of inducing local fluid motion without the need of adding mass. Finally, **plasma actuators** have been studied recently due to their fast time response; they do not having moving parts and they do not inject fluid. Each actuator type has its pros and drawbacks; no perfect actuator exists.

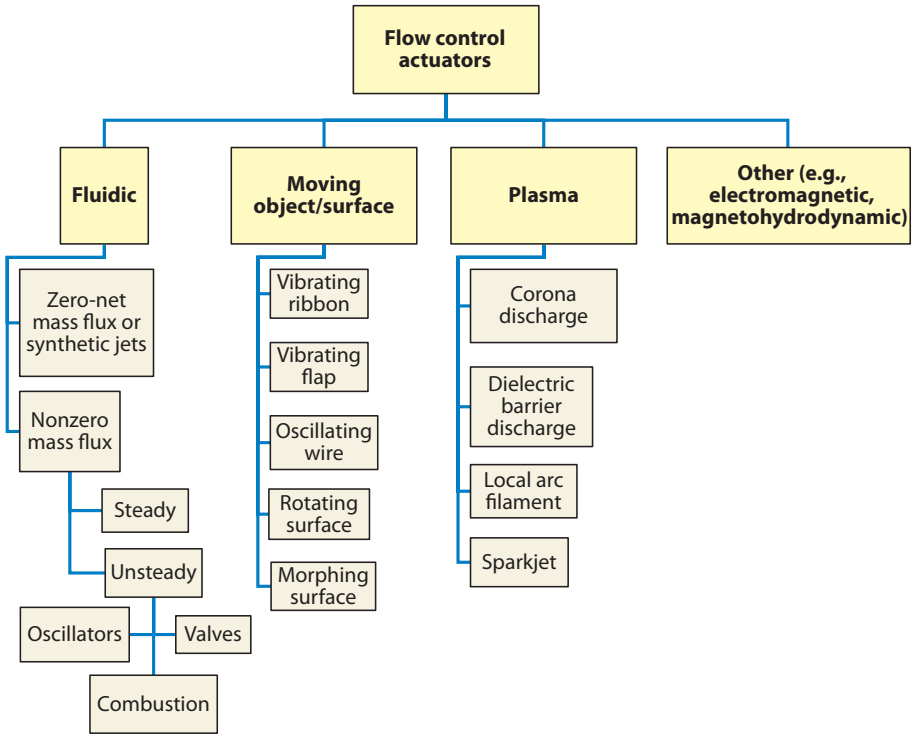

Figure 2.1: Classification of flow control actuators (Source: [1])

Most of the aforementioned studies have been performed at a high Reynolds number ($> 10^5$) and, usually, with thicker airfoils, which produce a trailing edge stall. The proposed numerical simulations of this report aims to study the effect of active flow control on the boundary layer of a NACA 0012 airfoil in a low Reynolds number ($Re = 5000$). This Reynolds number is of special interest for Mars missions because of the severe restrictions on size and weight, and the low density of the atmosphere [6]. Moreover, an advantage of this Re is that it does not require so much computational power as higher Reynolds numbers.

Chapter 3: Mathematical formulation of Navier-Stokes equations

In this project, only incompressible flow is studied. The NS equations describing the incompressible flow may seem easier, but incompressible flow is complicated in the sense that any perturbation in the flow is transported immediately through all the analyzed domain. As it can be deduced from this statement, incompressible flows go against the Einstein's principle that there is a maximum speed (speed of light). However, true incompressible flows do not exist in nature; they are a concept to simplify the equations.

Using Einstein summation convention, the incompressible Navier-Stokes equations (both continuity and momentum) are:

$$\frac{\partial u_i}{\partial x_i} = 0 \tag{3.0.1}$$

$$\frac{\partial u_j}{\partial t} + u_i \frac{\partial u_j}{\partial x_i} = -\frac{1}{\rho}\frac{\partial p}{\partial x_j} + \nu \frac{\partial^2 u_j}{\partial x_i \partial x_i} + \mathbb{S}_i(x,t) \tag{3.0.2}$$

The momentum equation has the following well-known terms:

- **Time derivative term**: $\frac{\partial u_j}{\partial t}$
- **Convection term**: In the previous equation, it is written in the so-called conservative form (see [16]):

$$\frac{\partial (u_i u_j)}{\partial x_i} = \cancel{\frac{\partial u_i}{\partial x_i} u_j} + u_i \frac{\partial u_j}{\partial x_i} = u_i \frac{\partial u_j}{\partial x_i} \tag{3.0.3}$$

- **Diffusion term**: $\nu \frac{\partial^2 u_j}{\partial x_i \partial x_i}$
- **Pressure gradient**: $-\frac{1}{\rho}\frac{\partial p}{\partial x_j}$
- **Source term**: $\mathbb{S}_i(x,t)$

The above equations can be expressed in a clearer way using an expanded form:

$$\frac{\partial u_1}{\partial x_1} + \frac{\partial u_2}{\partial x_2} + \frac{\partial u_3}{\partial x_3} = 0 \tag{3.0.4}$$

$$\begin{aligned}
\frac{\partial u_1}{\partial t}+u_1\frac{\partial u_1}{\partial x_1}+u_2\frac{\partial u_1}{\partial x_2}+u_3\frac{\partial u_1}{\partial x_3} &= -\frac{1}{\rho}\frac{\partial p}{\partial x_1}+\nu\left(\frac{\partial^2 u_1}{\partial x_1^2}+\frac{\partial^2 u_1}{\partial x_2^2}+\frac{\partial^2 u_1}{\partial x_3^2}\right)+\mathbb{S}_1(x,t)\\
\frac{\partial u_2}{\partial t}+u_1\frac{\partial u_2}{\partial x_1}+u_2\frac{\partial u_2}{\partial x_2}+u_3\frac{\partial u_2}{\partial x_3} &= -\frac{1}{\rho}\frac{\partial p}{\partial x_2}+\nu\left(\frac{\partial^2 u_2}{\partial x_1^2}+\frac{\partial^2 u_2}{\partial x_2^2}+\frac{\partial^2 u_2}{\partial x_3^2}\right)+\mathbb{S}_2(x,t)\\
\frac{\partial u_3}{\partial t}+u_1\frac{\partial u_3}{\partial x_1}+u_2\frac{\partial u_3}{\partial x_2}+u_3\frac{\partial u_3}{\partial x_3} &= -\frac{1}{\rho}\frac{\partial p}{\partial x_3}+\nu\left(\frac{\partial^2 u_3}{\partial x_1^2}+\frac{\partial^2 u_3}{\partial x_2^2}+\frac{\partial^2 u_3}{\partial x_3^2}\right)+\mathbb{S}_3(x,t)
\end{aligned} \tag{3.0.5}$$

In 2D, the existence and smoothness of Navier-Stokes solutions have been proven for a long time [17]. However, in three dimensions, it has not been possible to show that this kind of solutions exist. In fact, nowadays, the main scientific advances in the field of fluid dynamics have came not from solving NS equations but from either developing more powerful computers or implementing smarter and faster solver algorithms.

The aim of this report regarding NS equations is to implement or apply schemes which are energy-preserving. Thus, we are aiming to achieve two aspects of the discretization: convection discretizations that redistribute the energy over the scales of motion without dissipation; and diffusion discretizations which dissipate energy from a scale without transporting energy to other scales of motion (see [18]).

Chapter 4: Implementation of a spectro-consistent CFD code

In this section, the main steps to implement the current CFD code are explained. This spectro-consistent code has been developed up to the point of being able to solve the Taylor-Green Vortices problem.

4.1 Spectro-consistent discretization of Navier-Stokes equations

By discretizing the NS equations (see chapter 3) in space, the following general expressions can be obtained [2]:

$$\rho\Omega\frac{d\boldsymbol{u}}{dt}+C(\boldsymbol{u})\boldsymbol{u}+D\boldsymbol{u}+\Omega G\boldsymbol{p}=\Omega\mathbb{S} \tag{4.1.1}$$

$$M\boldsymbol{u}=0 \tag{4.1.2}$$

Where $\boldsymbol{u}$ and $\boldsymbol{p}$ represent the discrete approximations of u and p. $\boldsymbol{u}$ is a vector containing all the three velocity components. Thus, if N is the number of Control Volumes (CVs) on a given direction, assuming to have the same number of CVs on all directions, $\boldsymbol{p}$ is a N^3 component vector while $\boldsymbol{u}$ is a $3N^3$ component vector. In this case, the order of the velocity vector is:

$$\boldsymbol{u}=\begin{bmatrix}u_1 & u_2 & \dots & u_{N^3} & v_1 & \dots & v_{N^3} & w_1 & \dots & w_{N^3}\end{bmatrix}^t \tag{4.1.3}$$

Where the domain is usually analyzed with three loops (an outer loop for the z component, an inner for the y component and the most inner loop for the x component).

In this project, we have applied a staggered grid: velocities are staggered while pressure is centered. Moreover, since the cases to be solved with this code are restrained to periodic problems in all directions, halo cells have been added for computational convenience (so that all 'true' cells have neighbors). These halos are updated at each temporal iteration. The type of mesh (2D for simplicity) used herein can be seen in Figure 4.1.

The velocities are represented by arrows while the pressures by dots. As it can be seen, the halo variables (in red) can be obtained applying periodicity (green arrows) from the 'true' variables (in black).

The matrices of Equation 4.1.1 and Equation 4.1.2 are defined below:

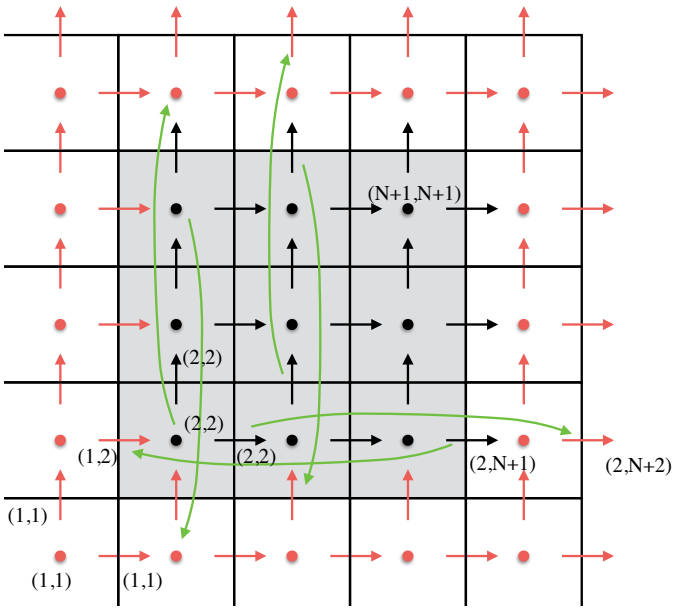

Figure 4.1: Example of a 3x3 2D mesh using the methodology of the implemented code (Source: [2])

- Ω: Diagonal $3N^3$ x $3N^3$ matrix with the volume of each CV in the staggered mesh.
- C: $3N^3$ x $3N^3$ matrix (function of $\boldsymbol{u}$) that expresses the convection operator.
- D: $3N^3$ x $3N^3$ constant matrix that expresses the diffusion operator.
- G: $3N^3$ x N^3 representing the gradient operator.
- M: N^3 x $3N^3$ representing the divergence operator.

Since we are implementing a spectro-consistent solution [18], the matrices need to obey some properties, which can be deduced from the study of the total discrete kinetic energy:

$$|\boldsymbol{u}|^2 = \boldsymbol{u}^t \Omega \boldsymbol{u} \tag{4.1.4}$$

Using the Chain rule:

$$\frac{d}{dt}(\boldsymbol{u}^t \Omega \boldsymbol{u}) = \boldsymbol{u}^t \left(\Omega \frac{d\boldsymbol{u}}{dt}\right) + \left(\frac{d\boldsymbol{u}^t}{dt}\Omega\right)\boldsymbol{u} = \boldsymbol{u}^t \left(\Omega \frac{d\boldsymbol{u}}{dt}\right) + \left(\Omega \frac{d\boldsymbol{u}}{dt}\right)^t \boldsymbol{u} \tag{4.1.5}$$

Evaluating the term $\Omega \frac{d\boldsymbol{u}}{dt}$ according to Equation 4.1.1 and using the algebraic property that $(AB)^t = B^t A^t$, the following expression can be obtained (see section A.1 for further details):

$$\frac{d}{dt}(\boldsymbol{u}^t \Omega \boldsymbol{u}) = -\boldsymbol{u}^t (C + C^t)\boldsymbol{u} - \boldsymbol{u}^t (D + D^t)\boldsymbol{u} - (\boldsymbol{u}^t \Omega G \boldsymbol{p} + \boldsymbol{p}^t G^t \Omega^t \boldsymbol{u}) \tag{4.1.6}$$

Analyzing Equation 4.1.6, the following properties can be deduced (see [18] for further details):

- Convection term: It has to be zero since convection only transports kinetic energy from scale to scale without dissipating energy. **Thus $C(\boldsymbol{u})$ has to be a skew-symmetric matrix for any divergence-free (incompressible) velocity field.**
- Diffusion term: It can only dissipate energy according to the 2nd principle of thermodynamics. Thus, D **has to be a definite positive (due to negative sign) matrix**.
- $\nabla \boldsymbol{p}$ term: Its contribution must be 0. **Then, G and M have to be related by** $\Omega G = -M^t$. In this way, if $M\boldsymbol{u} = 0$ (continuity equation), the last term is 0.
- Temporal term: It has to be equal to the diffusion term from the above deductions.

4.1.1 Ω, M, G and L matrices

As said below, Ω matrix can be computed setting the diagonal to the value of the volume of the staggered cell. In matrix M, each row represents a CV and it gives a scalar if multiplied by the velocity. On the other hand, in matrix G, each column is a CV and it gives a vector if multiplied by a scalar. Finally, the laplacian matrix can be calculated as:

$$L = M \cdot G \tag{4.1.7}$$

In Figure 4.2, the sparsity pattern of the aforementioned matrices is given for a 3x3x3 mesh. As it can be seen, each row of M (or each column of G) has exactly 6 dots, which represent the neighbors of each CV.

In order to validate these matrices in the code, the following has been tested with success (activating the boolean 'checkMatrices'):

- The computed matrix G is the same as the one computed with $G = -\Omega \cdot inv(M^t)$.
- Matrix L is symmetric within machine precision. This is done by computing that the difference between L and L^t is 0.
- Matrix L is semi-definite negative. Thus, all the eigenvalues have to be negative or 0.
- Matrix L is singular. The sum of all the elements in a row must be 0.

After carrying out these tests, it is safer to say that Ω, M, G and L matrices are correct since they are all involved in the aforementioned tests.

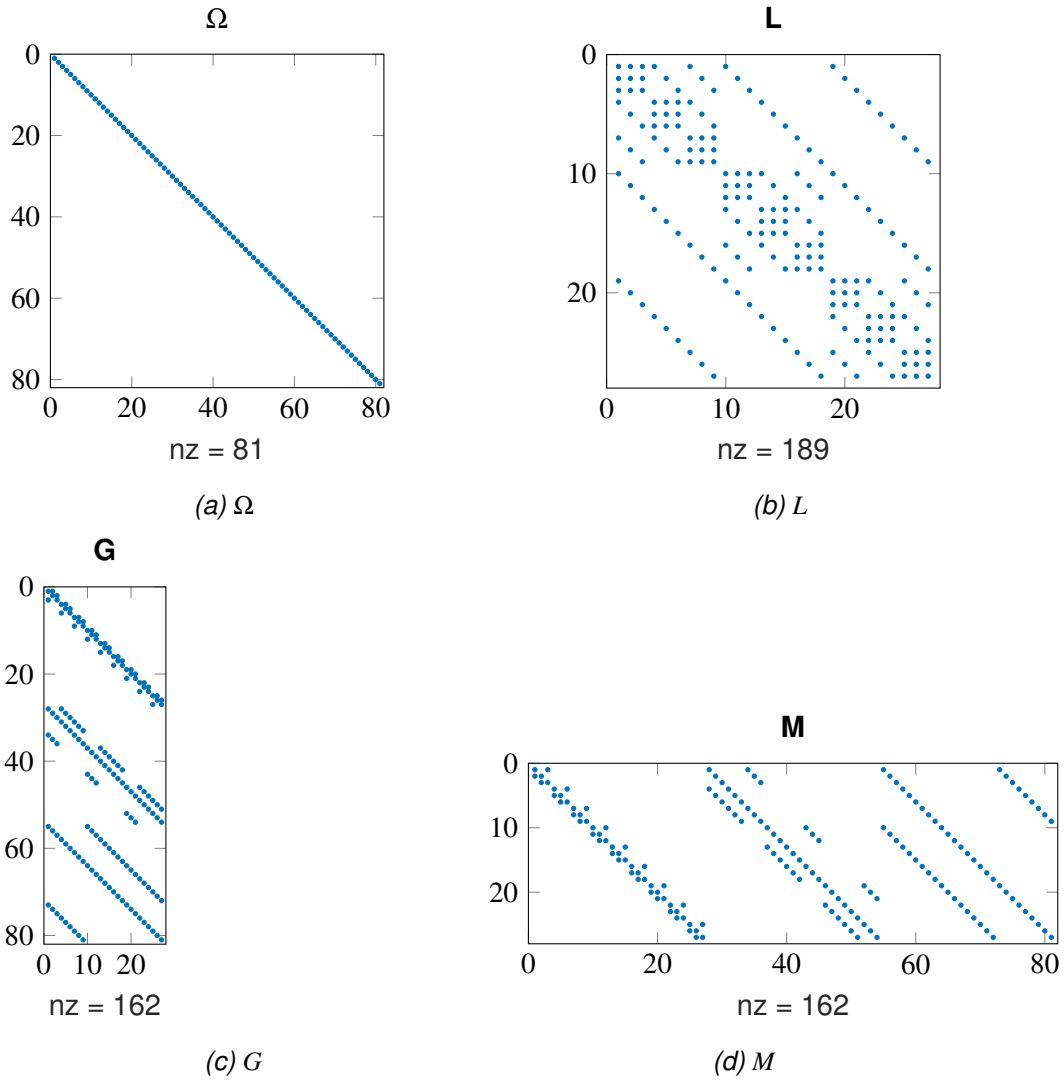

(a) Ω *(b)* L

(c) G *(d)* M

Figure 4.2: Sparsity of matrices Ω, M, G *and* L *with periodic boundary conditions*

4.1.2 Diffusion operator

A schematic for computing the diffusion operator (2D) in the x direction can be seen in Figure 4.3. In 3D, it is similar but adding an 'up' and 'down' velocity. For instance, for computing the diffusion in the x direction, the following equations are needed in 3D:

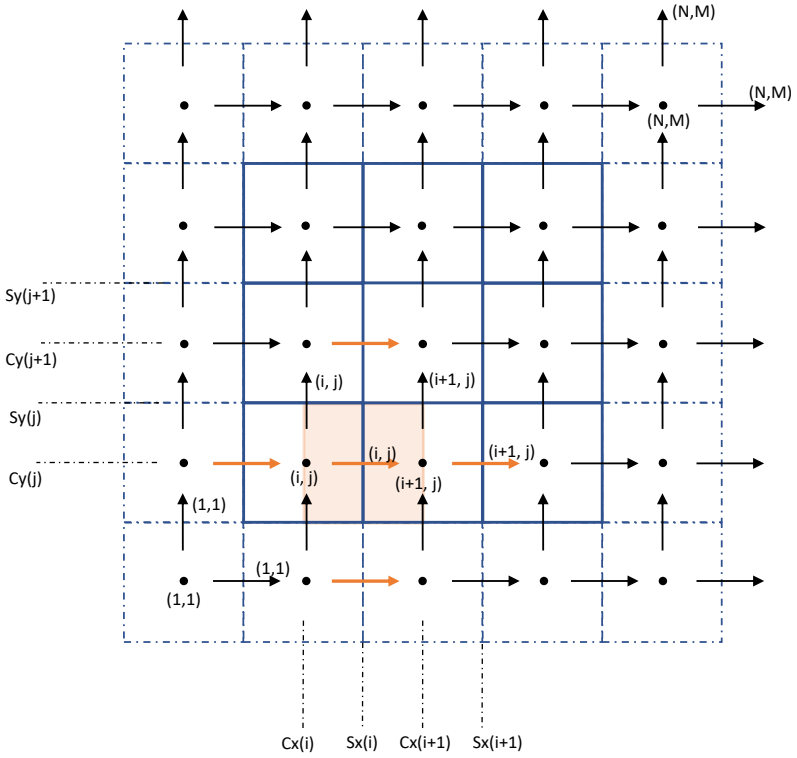

Figure 4.3: Example of a 3x3 2D schematic for computing the diffusion in the x direction

$$
\begin{aligned}
d_e &= \Gamma \cdot \frac{u(k,j,i+1) - u(k,j,i)}{\delta_e} \cdot S_e \\
d_w &= \Gamma \cdot \frac{u(k,j,i) - u(k,j,i-1)}{\delta_w} \cdot S_w \\
d_n &= \Gamma \cdot \frac{u(k,j+1,i) - u(k,j,i)}{\delta_n} \cdot S_n \\
d_s &= \Gamma \cdot \frac{u(k,j,i) - u(k,j-1,i)}{\delta_s} \cdot S_s \\
d_u &= \Gamma \cdot \frac{u(k+1,j,i) - u(k,j,i)}{\delta_u} \cdot S_u \\
d_d &= \Gamma \cdot \frac{u(k,j,i) - u(k-1,j,i)}{\delta_d} \cdot S_d
\end{aligned}
\tag{4.1.8}
$$

Where δ is the difference between the center of the cell and neighbor in the required direction. Thus, it is a difference between centered positions except in the staggered direction (x in this case), where it is a difference between staggered positions. On the other hand, S represents the cross surface respect to the required direction. For the momentum equations, $\Gamma = \mu$.

Thus, the diffusion operator on a given cell is computed as:

$$
D_x(k,j,i) = d_e - d_w + d_n - d_s + d_u - d_d \tag{4.1.9}
$$

The above expressions are evaluated at each cell (via three loops). After computing

the diffusion in the x direction, y and z directions are evaluated analogously with the corresponding mesh staggered on the correct direction.

It is important to highlight that, here and in the next subsection, we are computing operators and not matrices. The difference is that the operators are function of the velocity, while matrices are multiplied by the velocity vector and do not change within each iteration. Computationally speaking, it is much faster to compute an operator than a matrix, which occupies a huge amount of space in the RAM memory.

4.1.3 Convection operator

Computing the convection is more complicated than the diffusion since it depends on all the components of the velocity (due to mass fluxes). However, the procedure is quite similar. A 2D schematic for computing convection in the x direction can be seen in Figure 4.4. First of all, the mass flows are computed:

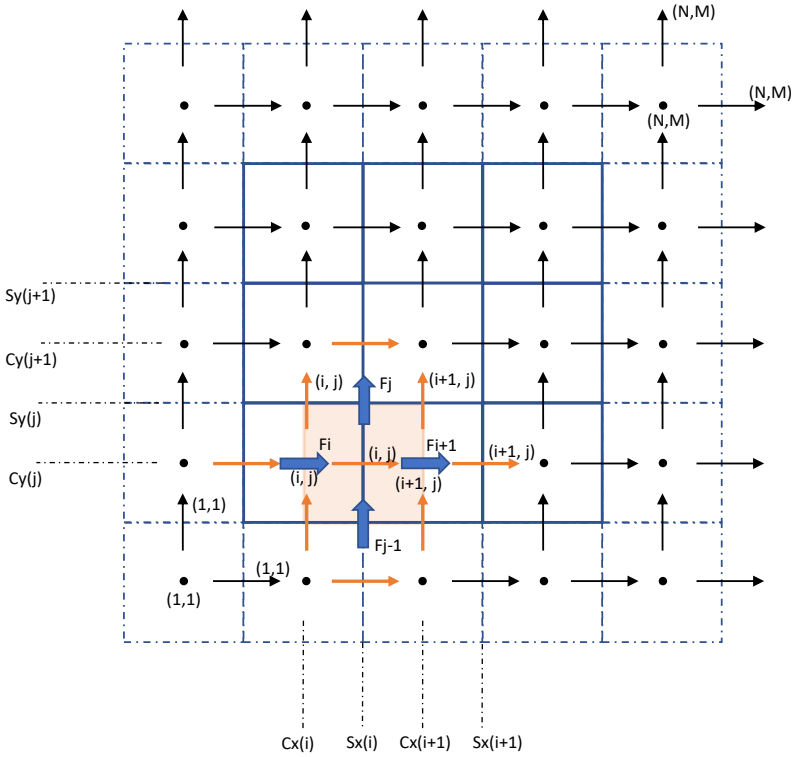

Figure 4.4: Example of a 3x3 2D schematic for computing the convection in the x direction

$$
\begin{aligned}
F_i &= \frac{1}{2}\rho(u_w S_w + u_c S_c) \\
F_{i+1} &= \frac{1}{2}\rho(u_c S_c + u_e S_e) \\
F_j &= \frac{1}{2}\rho(v_{sw} S_{sw} + v_{se} S_{se}) \\
F_{j+1} &= \frac{1}{2}\rho(v_{nw} S_{nw} + v_{ne} S_{ne}) \\
F_k &= \frac{1}{2}\rho(w_{dw} S_{dw} + w_{de} S_{de}) \\
F_{k+1} &= \frac{1}{2}\rho(w_{uw} S_{uw} + w_{ue} S_{ue})
\end{aligned}
\tag{4.1.10}
$$

Being S the transverse surface. The v and w velocities (in the case of the convection in the x direction) are the ones located on the corners of the staggered cell.

In the current code, there are two schemes implemented: **upwind** and **consistent**. The *upwind* takes the value upwind the flow while the *consistent* computes the faced velocities as a mean between the centered velocity and the neighbor one (no interpolation is performed **regardless not being a uniform mesh**). After this, the faced velocities (identified herein with the sub-index 'f') are used to compute the value of the convection at the given cell:

$$
C_x(k,j,i) = F_{i+1} \cdot u_{f_e} - F_i u_{f_w} + F_{j+1} u_{f_n} - F_j u_{f_s} + F_{k+1} u_{f_u} - F_k u_{f_d} \tag{4.1.11}
$$

The above expressions are evaluated at each cell (via three loops). After computing the convection in the x direction, y and z directions are evaluated analogously.

4.1.4 Validation of diffusion and convection operators

In order to validate both the diffusion and convection operators, the error respect to the exact solution (evaluated at specific points without discretizing) is analyzed. For the diffusion operator, the Root Mean Squared Error (RMSE) that should tend to 0 when increasing the mesh is:

$$
\begin{aligned}
RMSE_{Du} &= \sqrt{\frac{\sum_{k=1}^{N}\sum_{j=1}^{N}\sum_{i=1}^{N}\left|\frac{D_x(k,j,i)}{vol} - \mu\Delta_u\right|^2}{N^3}} \\
RMSE_{Dv} &= \sqrt{\frac{\sum_{k=1}^{N}\sum_{j=1}^{N}\sum_{i=1}^{N}\left|\frac{D_y(k,j,i)}{vol} - \mu\Delta_v\right|^2}{N^3}} \\
RMSE_{Dw} &= \sqrt{\frac{\sum_{k=1}^{N}\sum_{j=1}^{N}\sum_{i=1}^{N}\left|\frac{D_z(k,j,i)}{vol} - \mu\Delta_w\right|^2}{N^3}}
\end{aligned}
\tag{4.1.12}
$$

where vol is the volume of each cell and Δ is the laplacian of the given velocity component.

For the convection operator, the RMSE can be expressed by the following expressions:

$$
\begin{aligned}
RMSE_{Cu} &= \sqrt{\frac{\sum_{k=1}^{N}\sum_{j=1}^{N}\sum_{i=1}^{N}|\frac{C_x(k,j,i)}{vol} - \rho(u\frac{\partial u}{\partial x} + v\frac{\partial u}{\partial y} + w\frac{\partial u}{\partial z})|^2}{N^3}} \\
RMSE_{Cv} &= \sqrt{\frac{\sum_{k=1}^{N}\sum_{j=1}^{N}\sum_{i=1}^{N}|\frac{C_y(k,j,i)}{vol} - \rho(u\frac{\partial v}{\partial x} + v\frac{\partial v}{\partial y} + w\frac{\partial v}{\partial z})|^2}{N^3}} \\
RMSE_{Cw} &= \sqrt{\frac{\sum_{k=1}^{N}\sum_{j=1}^{N}\sum_{i=1}^{N}|\frac{C_z(k,j,i)}{vol} - \rho(u\frac{\partial w}{\partial x} + v\frac{\partial w}{\partial y} + w\frac{\partial w}{\partial z})|^2}{N^3}}
\end{aligned}
\tag{4.1.13}
$$

It is worth noting that the above expressions come from Equation 3.0.5. Finally, besides observing that the error of both operators is reduced when the mesh increase in number of CVs, it is important to see that both operators have a quadratic trend.

In Figure 4.5 and Figure 4.6, the reader can observe that both operators follow a quadratic convergence. As expected, when the upwind scheme is applied, the trend is linear.

This error convergence has been checked both for a 2D velocity distribution ($w = 0$) and for a full 3D velocity distribution in order to validate the convection and diffusion operator on most possible circumstances. The exact used velocity distributions (free-divergence) have been:

- 2D initial distribution (TGV): Domain from $-\pi L$ to πL

$$
\begin{aligned}
u &= V_0 \cdot \sin\left(\frac{x}{L}\right) \cdot \cos\left(\frac{y}{L}\right) \cdot \cos\left(\frac{z}{L}\right) \\
v &= -V_0 \cdot \cos\left(\frac{x}{L}\right) \cdot \sin\left(\frac{y}{L}\right) \cdot \cos\left(\frac{z}{L}\right) \\
w &= 0
\end{aligned}
\tag{4.1.14}
$$

- 3D distribution: Domain from 0 to 1

$$
\begin{aligned}
u &= 2\cos(2\pi x)\sin(2\pi y)\sin(2\pi z) \\
v &= -\sin(2\pi x)\cos(2\pi y)\sin(2\pi z) \\
w &= -\sin(2\pi x)\sin(2\pi y)\cos(2\pi z)
\end{aligned}
\tag{4.1.15}
$$

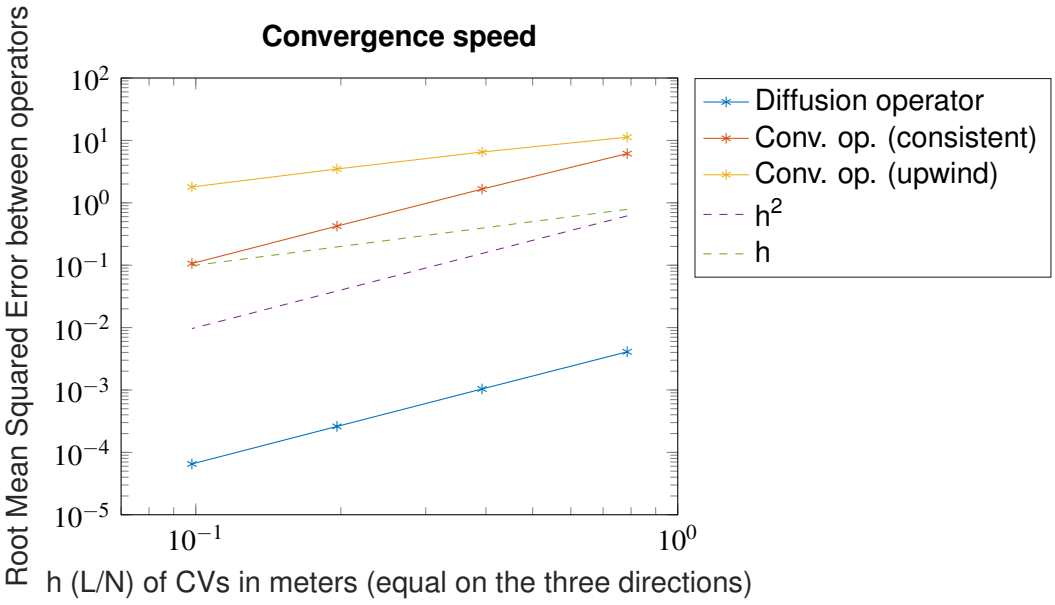

Figure 4.5: Error convergence for an initial 2D velocity distribution (TGV)

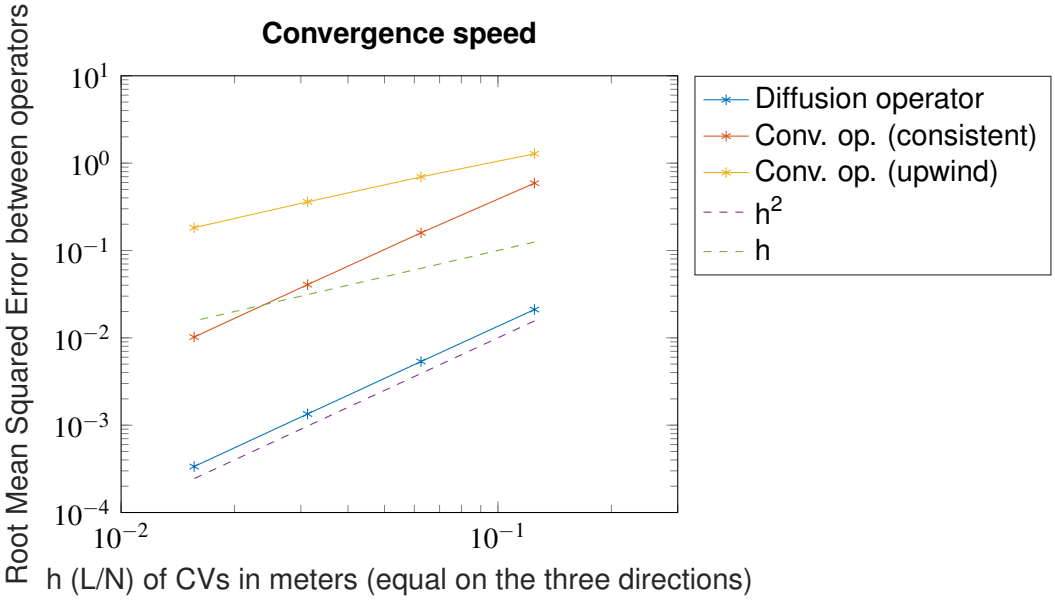

Figure 4.6: Error convergence for a 3D velocity distribution

4.2 Pressure-velocity coupling

An arbitrary vector $\boldsymbol{u}^p$ can be transformed into a divergence-free vector $\boldsymbol{u}$ after the addition of the gradient of a suitable scalar field $\boldsymbol{p}$:

$$\boldsymbol{u} = \boldsymbol{u}^p - G\boldsymbol{p} \tag{4.2.1}$$

Imposing the divergence-free condition (continuity equation):

$$M\boldsymbol{u} = M\boldsymbol{u}^p - MG\boldsymbol{p} = 0 \tag{4.2.2}$$

Thus, we get the linear Poisson equation for the field $\boldsymbol{p}$:

$$L\boldsymbol{p} = M\boldsymbol{u}^p \tag{4.2.3}$$

From the above equations, we can get a divergence-free velocity and the pressure field from the predicted velocity. However, this step is the most costly one computationally since the inverse of the Laplacian operator has to be evaluated (it is a full matrix). Moreover, the laplacian matrix is singular, which makes even more complex to get the solution of the Poisson equation.

In order to solve the aforementioned equations, the current code offers the two possibilities that are commented below.

4.2.1 Using the inverse operator

The most immediate way of solving the Poisson equation is by *perturbing* one of the diagonal elements of the singular laplacian matrix. For instance, the first element of the diagonal can be increased a 10%. By doing so, the laplacian matrix is not anymore a singular matrix and the inverse operator can be applied:

$$\begin{aligned} L_{ns} &= L \\ L_{ns}(1,1) &= 1.10 \cdot L_{ns}(1,1) \\ \boldsymbol{p} &= L_{ns}^{-1}\, M\boldsymbol{u}^p \end{aligned} \tag{4.2.4}$$

The issue about using the inverse operator is that its computational cost is $\mathcal{O}(N^3)$ for a 3D case. On the other hand, Fourier solver can achieve $\mathcal{O}(N)$ if applied to all directions, besides allowing parallel computing.

4.2.2 Using the Fourier solver

Fourier transform can be applied when, at least, one direction is uniform. In this case, the three directions are uniform. Therefore, Fourier can be applied in all the directions. This solver is the best option for sequential computers and provide solutions for parallel computing of three-dimensional flows [3].

Fourier solver is not trivial to implement, but by following reference [3] and [19], it has been possible to add it as a new functionality for the developed code. It is not the aim of this report to explain all the details behind Fourier transform methods, but a brief description of the implementation is given herein and in Appendix B.

The aim is to solve an equation of the following type of equation (Poisson equation):

$$L \cdot X = B \tag{4.2.5}$$

As it can be seen in the sparsity pattern of the Laplacian matrix (see Figure 4.2b), L is an hepta-diagonal matrix in the case of a three-dimensional flow. Since the grid is uniform in the three directions, the matrix L can be expressed as:

$$L = [a, c, d, b, a, c, d]_p \tag{4.2.6}$$

Where a represents the east-west two diagonals (1st component), b the main diagonal, c the north-south diagonals (2nd component) and d the up-down diagonals (3rd component).

The details of the implementation of the 3D Fourier solver can be found in Appendix B. It is important to bear in mind that this solver achieves $\mathcal{O}(N)$ with the mesh size, while using inverse operation would be $\mathcal{O}(N^3)$.

4.3 Time discretization

In order to discretize in time, the momentum equation is written as follows:

$$\rho \frac{d\boldsymbol{u}}{dt} = R(\boldsymbol{u}) - G\boldsymbol{p} \tag{4.3.1}$$

Where R is:

$$R(\boldsymbol{u}) = -\Omega^{-1}(C(\boldsymbol{u})\boldsymbol{u} + D\boldsymbol{u}) + \mathbb{S} \tag{4.3.2}$$

To carry out the temporal discretization, each term is treated as indicated in [2]:

- **Time derivative**: Central difference (2nd order)
- R: Second-order Adams-Bashforth
- **Pressure gradient**: Implicit first order (Poisson equation)

As it can be observed, although we try to carry out explicit schemes, the pressure gradient has to be solved implicitly. The time-discrete system becomes:

$$\begin{aligned} \rho \frac{\boldsymbol{u}^{n+1} - \boldsymbol{u}^n}{\Delta t} &= \frac{3}{2} R^n - \frac{1}{2} R^{n-1} - G\boldsymbol{p}^{n+1} \\ M\boldsymbol{u}^{n+1} &= 0 \end{aligned} \tag{4.3.3}$$

Where n is the current instant of time. Introducing the *predictor velocity* $\boldsymbol{u}^p$:

$$\boldsymbol{u}^p = \boldsymbol{u}^n + \frac{\Delta t}{\rho}\left(\frac{3}{2} R^n - \frac{1}{2} R^{n-1}\right) \tag{4.3.4}$$

the momentum equation is left as:

$$\boldsymbol{u}^{n+1} = \boldsymbol{u}^p - G\tilde{\boldsymbol{p}} \tag{4.3.5}$$

The solution to this equation has been explained in section 4.2. It is worth noting that a modified pressure is obtained:

$$\tilde{\boldsymbol{p}} = \Delta t \boldsymbol{p}^{n+1} \tag{4.3.6}$$

In the first iteration, $\boldsymbol{u}^{n-1}$ is not available. Thus, $\boldsymbol{u}^{n-1} = \boldsymbol{u}^n$ is imposed.

Since we are dealing with an explicit discretization, stability has to be ensured. Two conditions have to be verified:

- **Diffusion terms**:

$$\Delta t_d \leq \frac{1}{2} \min\left(\frac{\Delta^2}{\nu}\right) \tag{4.3.7}$$

  Where Δ is the spacing of the grid on each dimension.

- **Convection terms**:

$$\Delta t_c \leq \min\left(\frac{\Delta}{|\boldsymbol{u}|}\right) \tag{4.3.8}$$

Then, the time is chosen as:

$$\Delta t = CFL \cdot \min(\Delta t_d, \Delta t_c) \tag{4.3.9}$$

Theoretically, CFL should be below 1.0 but, in practice, with this scheme, the values have to be lower, about 0.3. It can be changed by the user, but usually 0.1 has been used herein.

4.4 Computation of the main variables

Besides the velocity and pressure distribution, there are some important parameters that also need to be computed for a complete post-processing:

- **Kinetic energy**:

$$E_k = \frac{1}{\Omega}\int_{\Omega}\frac{\boldsymbol{u}\cdot\boldsymbol{u}}{2}d\Omega \tag{4.4.1}$$

The temporal evolution of the kinetic energy must follow a decreasing trend to comply with the 1st principle of the thermodynamics.

- **Kinetic energy dissipation rate**:

$$\epsilon = -\frac{dE_k}{dt} \tag{4.4.2}$$

- **Vorticity**: Since the velocity is known at each iteration, vorticity can be computed with the curl operator:

$$\vec{\omega} = \nabla\times\vec{u} = \left(\frac{\partial w}{\partial y}-\frac{\partial v}{\partial z},\frac{\partial u}{\partial z}-\frac{\partial w}{\partial x},\frac{\partial v}{\partial x}-\frac{\partial u}{\partial y}\right) \tag{4.4.3}$$

Since the velocities are staggered, to numerically compute these partial derivatives is not trivial. Indeed, both interpolations of the velocity and the derivatives are necessary to obtain the centered vorticities. The exact details of the code are out of the scope, but the reader is encouraged to dig into the code for further details. In order to test the function computing the vorticity from the velocity, the RMSE respect to analytical vorticity has been computed for different mesh sizes for the velocity distribution of Equation 4.1.15. All the components of vorticity decrease quadratically as it can be observed in Figure 4.7 (several rotations have been tested since there is always one vorticity component which is 0 in the used velocity distribution).

- **Enstrophy**: Computed similarly to the energy but with the vorticity:

$$\varepsilon = \frac{1}{\Omega}\int_{\Omega}\frac{\boldsymbol{\omega}\cdot\boldsymbol{\omega}}{2}d\Omega \tag{4.4.4}$$

As said in reference [20], enstrophy is an important diagnostic since, in incompressible flows, the following must be verified:

$$\epsilon = 2\frac{\mu}{\rho}\varepsilon \tag{4.4.5}$$

The reader is encouraged to check a proof of this relation in section A.2.

- **Q-criterion**: This magnitude, developed by Hunt et al. [21], locates regions where rotation dominates strain in the flow. It is mathematically defined as:

$$Q = \frac{1}{2}\left(||\boldsymbol{\Omega}||^2 - ||\boldsymbol{S}||^2\right) \tag{4.4.6}$$

Where $\boldsymbol{\Omega}$ and $\boldsymbol{S}$ are the symmetric and antisymmetric parts of $\nabla\boldsymbol{u}$. $||\cdot||$ is the Frobenius matrix norm.

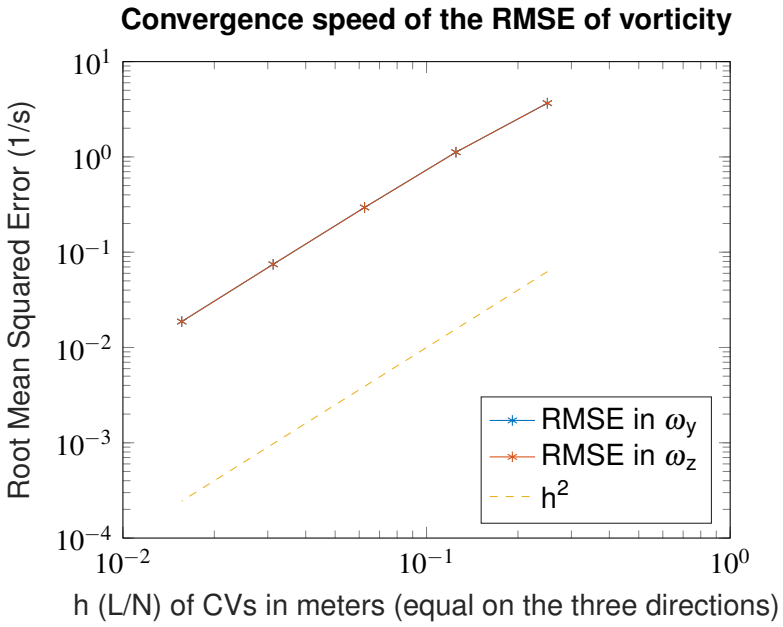

Figure 4.7: RMSE convergence of the vorticity

4.5 Global code validation

The code explained above has been validated by several means in Appendix C. Basically, the following aspects of the code have been globally tested:

- Validation with a fully 2D velocity distribution.
- Validation of the 3D code with rotations from a known 2D velocity distribution.
- Verification that the different terms are in accordance with the imposed convective scheme.

The code has been successful on all the aforementioned validations.

4.6 3D Taylor-Green Vortices solution

Although no analytical solution exists for the 3D TGV, the problem has been solved several times to test the accuracy and performance of high-order methods (see, for instance, reference [22], [23] and [24]). It is a useful problem because of the creation of small scales which need to be correctly solved. Moreover, no boundary condition is required to solve it.

As stated in [20], the initial velocity distribution is given by the following expres-

sions:

$$\begin{aligned} u &= V_0 \sin\left(\frac{x}{L}\right)\cos\left(\frac{y}{L}\right)\cos\left(\frac{z}{L}\right) \\ v &= -V_0 \cos\left(\frac{x}{L}\right)\sin\left(\frac{y}{L}\right)\cos\left(\frac{z}{L}\right) \\ w &= 0 \end{aligned} \tag{4.6.1}$$

Where both V_0 and L have been set 1.

The conditions of the problem are:

- $Re = 1600$: Imposed by setting the density and viscosity in accordance with the other variables $\left(Re = \frac{\rho V_0 L}{\mu}\right)$.
- Physical duration of the problem from Time Unit (TU)=0 to TU=20, where $TU = t \cdot V_0/L$.
- The domain is a periodic square box defined as $-\pi L \leq x, y, z \leq \pi L$.

Since the current code has been developed for a single core, simulations with the current code are limited to 64^3 grids due to computational limits. Note that according to [20], 256^3 DOFs should be used to completely solve all the implied structures. However, spectro-consistent code has proven to be really close to the solution with 64^3 DOFs, as the reader can observe hereafter. Since the implemented code in Matlab is limited to 64^3 control volumes, a code developed in C (also for a single core) from Dr. Manel Soria has been modified and used to obtain the results for 128^3 and 256^3 simulations.

In order to validate the results obtained for the Taylor-Green vortices, most of the variables mentioned in section 4.4 are plotted against literature results.

4.6.1 Volume-averaged kinetic energy

In Figure 4.8, it can be observed the volume-averaged normalized kinetic energy for both the spectro-consistent and upwind scheme respectively. The reference solution (using the DRP scheme on 512^3 DOFs [24]) is plotted with black dots. Note that the normalization has been performed using the kinetic energy at the first instant of time. The upwind scheme simulations are plotted with dashed lines while the spectro-consistent simulations with continuous lines. The simulations performed with the code in C are marked with an asterisk in the legend.

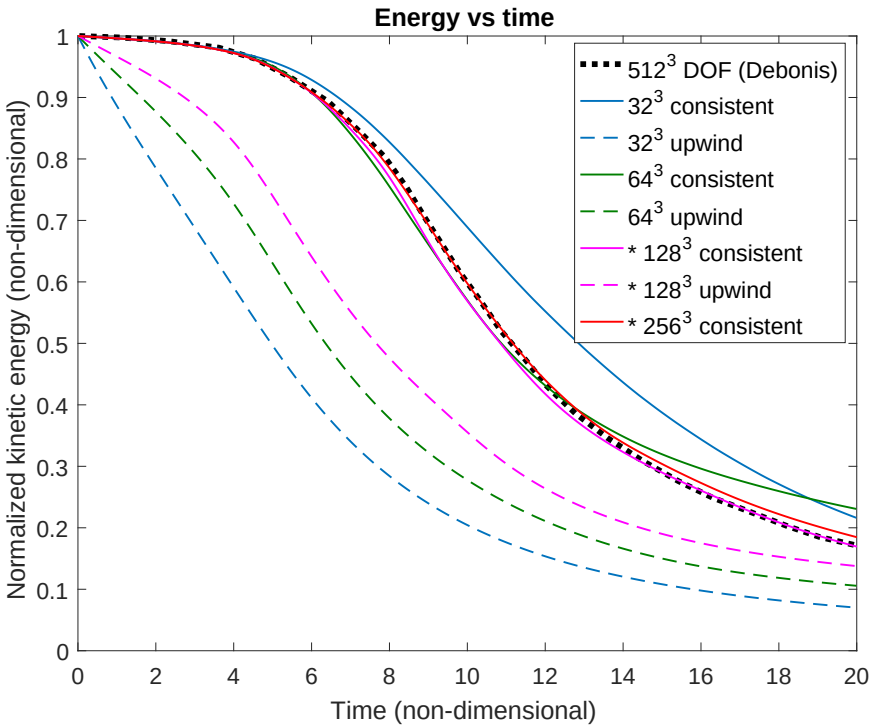

Figure 4.8: Evolution of normalized kinetic energy

As it can be seen, the upwind scheme is much further away from the reference solution than the spectro-consistent scheme for the same amount of control volumes. Obviously, the finer the mesh, the closer to the reference solution. However, it is interesting to note that spectro-consistent scheme already gives quite accurate results for 64^3 control volumes.

4.6.2 Energy dissipation rate

In Figure 4.9, the dissipation rate for both the spectro-consistent and upwind scheme can be respectively observed. The reference solution (using a pseudo-spectral 512^3 DOFs [20]) is plotted in black dots. The upwind scheme simulations are plotted with dashed lines while the spectro-consistent simulations with continuous lines. A different reference from previous section has been used in order to compare the obtained solutions with more diverse data.

The simulations performed with the code in C (128^3 and 256^3 control volumes) are marked with an asterisk.

In Figure 4.10, the difference (normalized) between the dissipation rate and the diffusion term uDu is also plotted to show that the upwind scheme (discontinuous lines) loses energy due to the convection term. The spectro-consistent scheme is

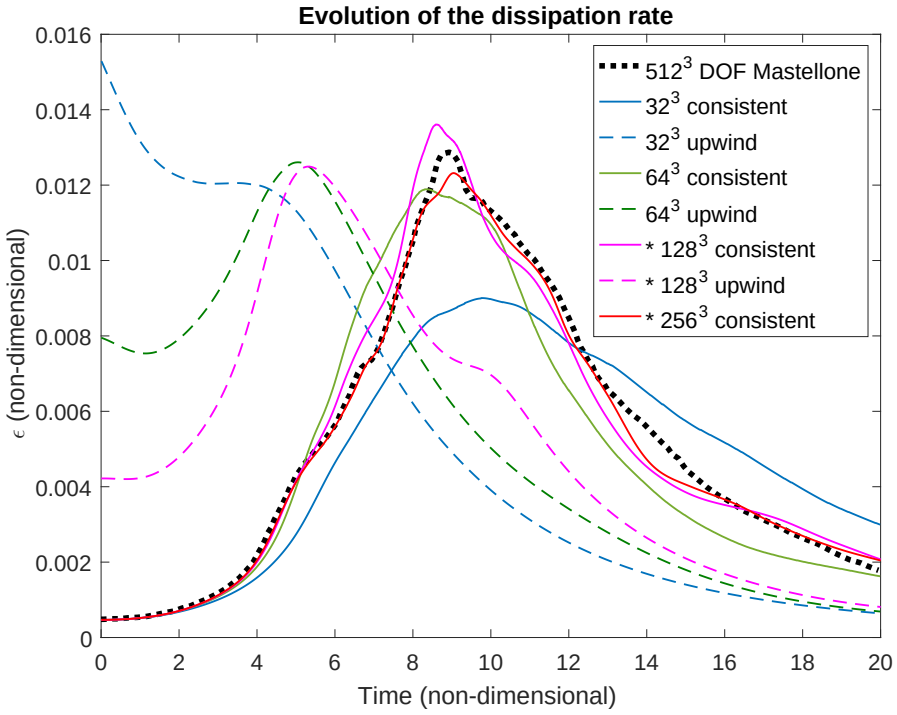

Figure 4.9: Evolution of energy dissipation rate

not depicted in the figure since there is no difference between the dissipation rate and the diffusion term.

Thus, it has been proved that the spectro-consistent scheme preserves the different energy schemes. This is not achieved in all the CFD codes. For instance, *Code_Saturne* [25] dissipates energy when solving the TGV problem as it can be also seen in continuous lines in Figure 4.10 (*Code_Saturne* data from Bachelor's Final Project of Jordi Amat [26]). The dissipation rate computed from the kinetic energy is close to the reference solution, but *Code_Saturne* does not completely comply the relation $\epsilon = 2\frac{\mu}{\rho}\varepsilon$ proved in section A.2. This means, that the convective scheme of *Code_Saturne* dissipates energy in a similar fashion to the upwind scheme (despite being less than the upwind scheme).

To sum up, while for the spectro-consistent scheme, the diffusive term is equal to the change of energy, it is not the case for the upwind scheme. Moreover, it can be clearly seen that the upwind scheme does not correctly solve all the implied scales in the TGV. It is worth noting that the 64x64x64 mesh gives quite accurate results (the peak is correctly located in time around 8 time units) for the spectro-consistent scheme.

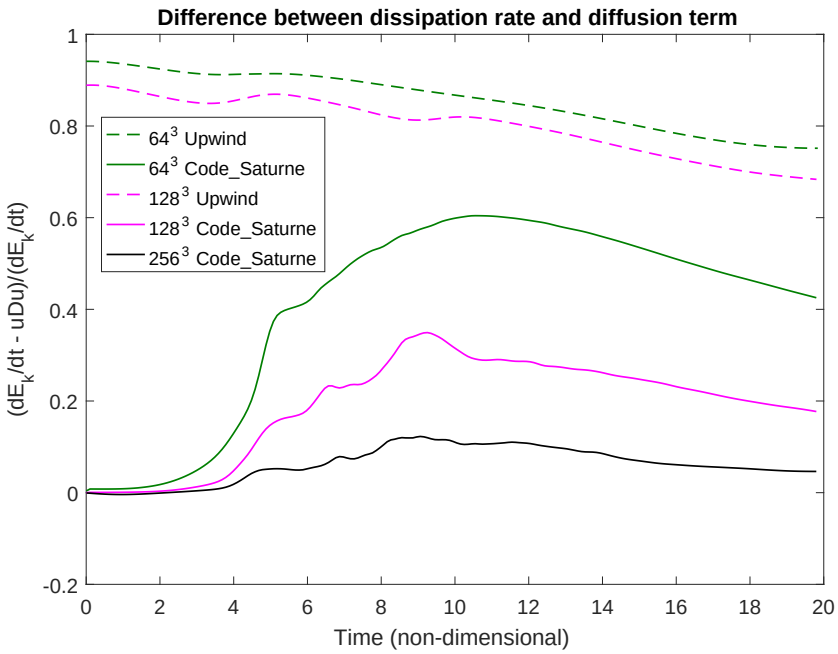

Figure 4.10: Difference between dissipation rate and diffusive term (dimensionless)

4.6.3 Instantaneous iso-surfaces plots

Iso-surfaces plots are useful in order to grasp an idea of the different scales implied in the problem. In this subsection, iso-surfaces of the 64x64x64 mesh using the spectro-consistent scheme (self-developed code) are given.

In Figure 4.11, we can observe the iso-surfaces of Q criterion (see section 4.4 for its definition) colored by velocity magnitude for the spectro-consistent scheme. The reader is encouraged to compare these plots with reference [23]; despite having a coarser mesh, the iso-surfaces plots are quite similar. On the other hand, in Figure 4.12, it is proved that the upwind scheme does not correctly solve all the implied structures of the problem.

The iso-surfaces of the z-component of the vorticity can be observed in Figure 4.13. These plots are really similar to the ones given in [20].

To sum up, even with a not too fine mesh, spectro-consistent scheme is able to obtain results close to the reference solutions given in the literature. This gives an idea of the potential of such type of discretization even for relatively coarse meshes.

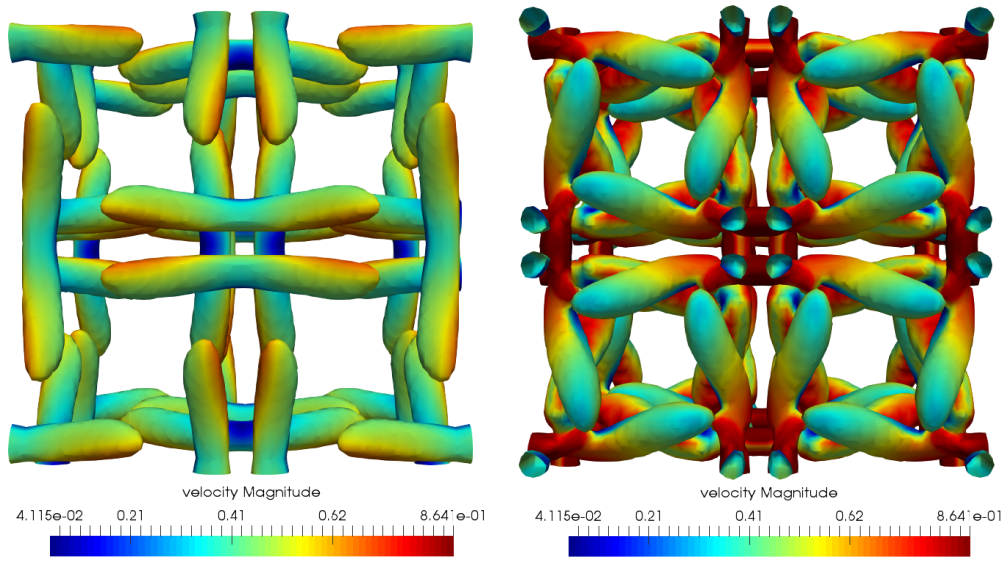

(a) $t \approx 2.5$ (b) $t \approx 5$

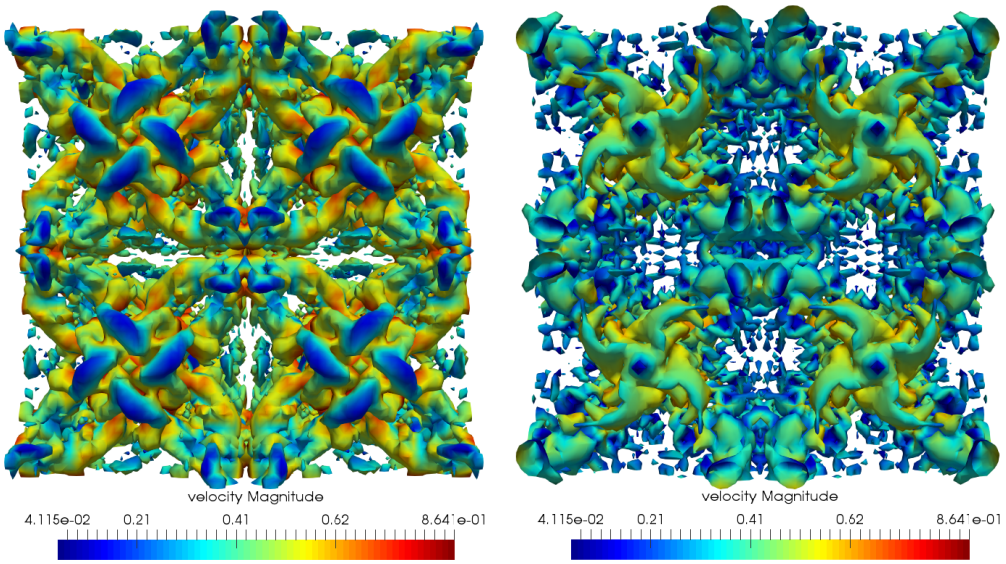

(c) $t \approx 8$ (d) $t \approx 10.75$

Figure 4.11: Iso-surfaces of Q=0.5 colored by velocity magnitude at different times (Spectro-consistent scheme with 64^3 CVs)

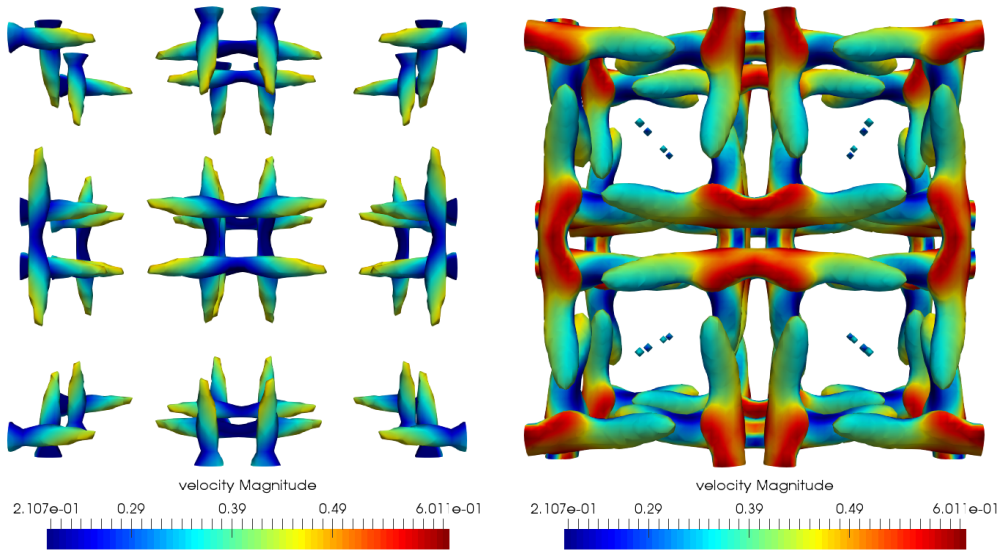

(a) $t \approx 2.5$ *(b)* $t \approx 5$

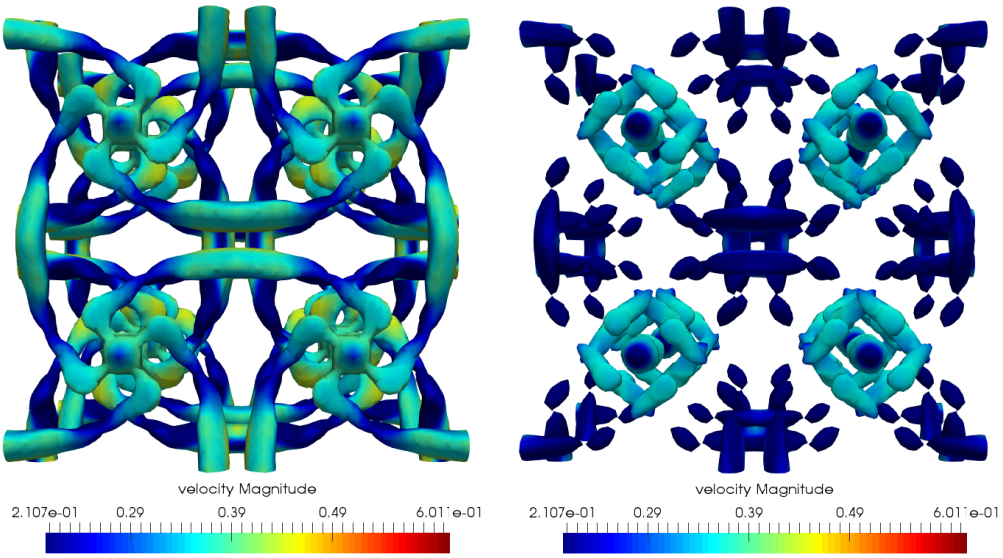

(c) $t \approx 8$ *(d)* $t \approx 10.75$

Figure 4.12: Iso-surfaces of Q=0.5 colored by velocity magnitude at different times (Upwind scheme with 64^3 *CVs)*

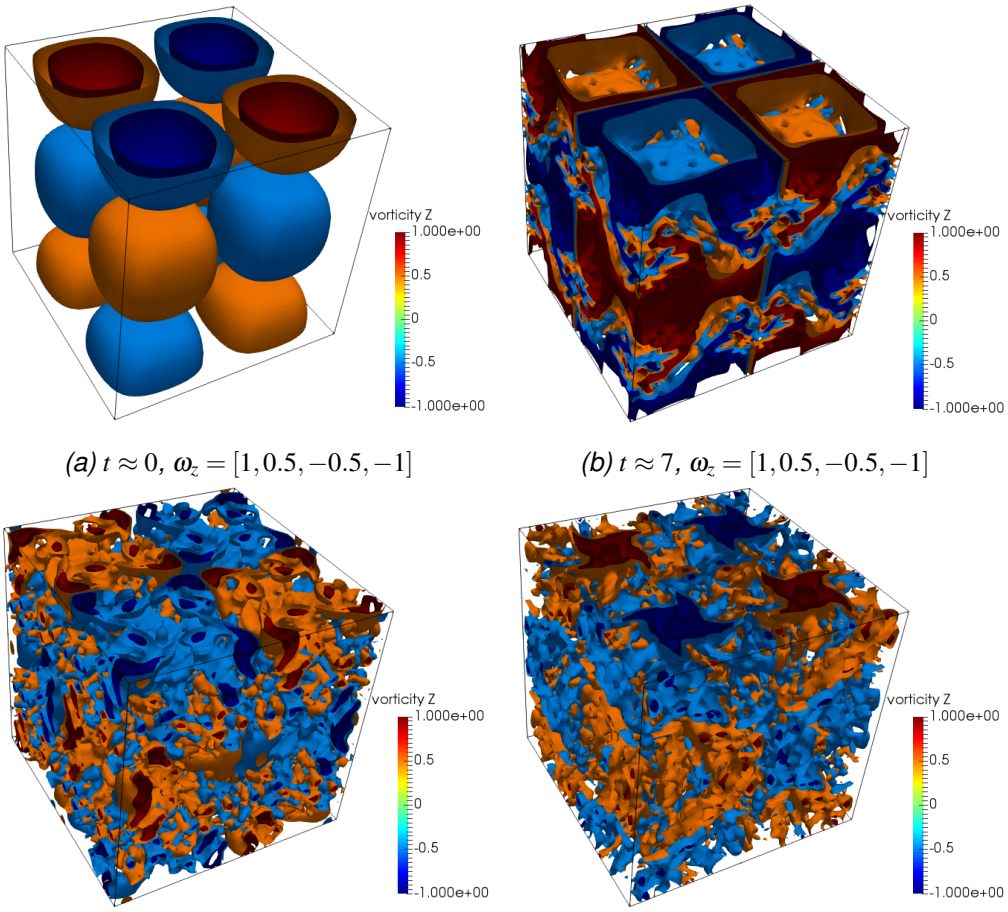

(a) $t \approx 0$, $\omega_z = [1, 0.5, -0.5, -1]$ *(b)* $t \approx 7$, $\omega_z = [1, 0.5, -0.5, -1]$

(c) $t \approx 14$, $\omega_z = [1, 0.5, -0.5, -1]$ *(d)* $t \approx 20$, $\omega_z = [1, 0.5, -0.5, -1]$

Figure 4.13: Iso-surfaces of z-component of vorticity for 64^3 *CVs*

Chapter 5: Computational Setup for the NACA 0012 airfoil simulations

In this section, the computational setup for the 2D simulations performed with the NACA 0012 airfoil is explained. NACA 0012 airfoil is not used herein because of having a particular interest in commercial aircraft but because several studies have been performed with this type of profile (i.e. [27], [7], [28], [29], [6], [15]). Thus, the behavior and data of the NACA 0012 airfoil is quite well-known.

5.1 Flow configuration

The flow configuration for the reference cases is shown in Figure 5.1. This type of domain is tailored to be suitable for different angles of attack (α), as long as the inclination is not so big as forcing the flow to exit by the inlet condition. Note that an angle of attack is achieved by only modifying the inlet flow so that the airfoil sees a flow inclination.

There are only three types of boundary conditions:

- **Inlet**: Uniform free-stream velocity (Dirichlet condition). Specifically, the norm of this velocity has been fixed to be $U_\infty = 1$ (dimensionless).
- **Outlet**: A pressure is fixed. Velocity given by Neumann condition. In this case, $P/P_{ref} = 0$ is used.
- **Non-slip wall**: $(u, v) = (0, 0)$ on the airfoil surface.

When adding the active flow control, a new boundary condition for the actuator is added on the airfoil. The exact details of this case can be found in chapter 7.

Several meshes have been tested. The size of the domain is such that the boundary conditions do not affect the flow over the airfoil. However, in all the cases, aC, bC and cC are between $10C$ and $20C$ (being C the airfoil chord) so that the minimum interference with the boundary conditions occurs.

Last but not least, all the simulations are performed for a $Re = 5,000$. This Reynolds number is of special interest for Mars missions because of the severe restrictions on size and weight [6]. Moreover, an advantage of this Re is that it does not require so much computational power as higher Reynolds numbers.

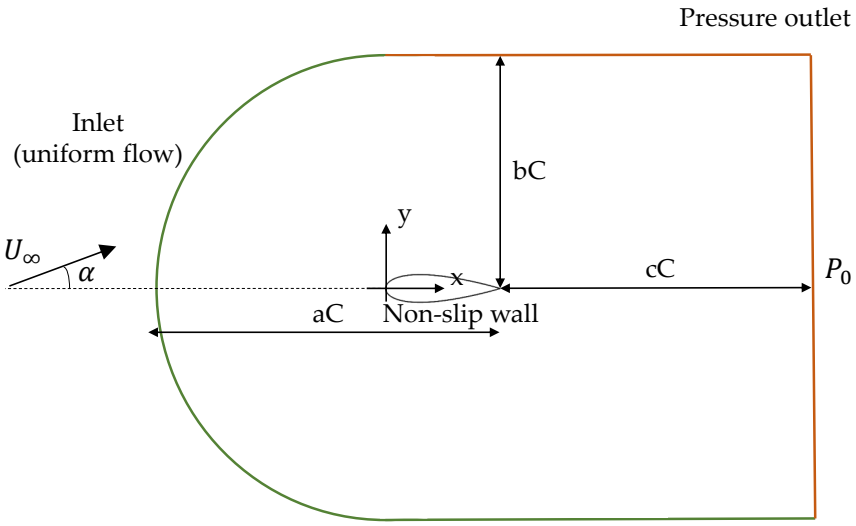

Figure 5.1: Domain configuration and boundary conditions for the NACA 0012 airfoil

5.2 Numerical parameters

The simulations of the NACA 0012 airfoil performed in this project have been carried out by using *Alya* software (developed at BSC [5]), whose usage permission has been granted due to an agreement between the *Alya* development team and the TUAREG (UPC) research group.

Alya is a high performance computational mechanics code to solve engineering coupled problems. The different physics solved by Alya are: incompressible/-compressible flow, solid mechanics, chemistry, particle transport, heat transfer, turbulence modeling, electrical propagation, etc. Alya was specially designed for massively parallel supercomputers. Parallelization is hybrid, using both MPI and OpenMP paradigms to take advantage of distributed and shared memory architectures, respectively. Accelerators like GPU are also exploited at the iterative solver levels to further enhance the performance of the code. Recently, dynamic load balance techniques have been introduced as well to better exploit computational resources at the node level. Alya implements a low dissipation finite element (FE) scheme, based on the same principles followed by Verstappen and Veldman [18], generalized for unstructured finite volumes by Jofre et al. [30] and extended to finite element (FE) schemes by Lehmkuhl et al. [31].

The basic idea behind this approach remains the same as described in chapter 4: to mimic the fundamental symmetry properties of the underlying differential operators, i.e., the convective operator is approximated by a skew-symmetric matrix and the diffusive operator by a symmetric, positive-definite matrix. The final set of equations is time integrated using an explicit third order Runge-Kutta method. The

pressure stabilization is achieved by means of a non-incremental fractional step. The chosen low dissipation FE scheme presents good accuracy compared to other low dissipation finite volume and finite difference methods with the advantage of being able to increase the order of accuracy at will without breaking the fundamental symmetry properties of the discrete operators. For more details, the reader is referred to [5].

The aforementioned **spectro-consistent discretization** is not available for other general purpose codes such as *Code_Saturne* [25] or *Open Foam* [32].

The used type of flow is laminar one. For those cases in which a steady state is reached ($AOA \leq 2$ deg) the simulations are stopped once the relative difference between two outer iterations of the independent variables is 10e-6. For the oscillatory solutions, first the flow is initialized at $(u, v) = (\cos\alpha, \sin\alpha)$ and then the flow is advanced until a quasi-steady state is reached, i.e., the average solution of the drag and lift coefficients do not vary in time. After that, average flow is computed by time integrating the variables until the end of the simulation (at least 15 time periods are recommended). For instance, at Angle of Attack (AOA)=10 deg (see Figure 6.1), quasi-steady state conditions are reached after 15 time units and then the flow is averaged from there until the end of the simulation.

Besides these numerical parameters, it is worth mentioning that 101 witness points have been set around the airfoil surface (computed with a Matlab script) to obtain the pressure coefficient distribution. Moreover, two witness points have been located in the wake: one near the leading edge and another one above the trailing edge of the airfoil. The location of these two last points depend on the angle of attack so that the full wake behavior is captured (see Table 5.1).

Angle of attack (deg)	1st probe $(x/c, y/c)$	2nd probe $(x/c, y/c)$
2	(0.6677, 0.0887)	(1.2802, 0.0380)
4	(0.6677, 0.0887)	(1.2802, 0.0380)
6	(0.6677, 0.0887)	(1.2802, 0.0380)
8	(0.2911, 0.1262)	(1.0669, 0.1308)
9	(0.2911, 0.1262)	(1.0669, 0.1308)
10	(0.2911, 0.1262)	(1.0669, 0.1308)
12	(0.2911, 0.1262)	(1.0669, 0.1308)
20	(0.2196, 0.1789)	(1.0800, 0.1943)

Table 5.1: Location of witness points depending on the angle of attack

5.3 Computational Mesh

Several meshes have been tested in this project so that their influence on the final solution could be seen. Hereafter, the two most used unstructured meshes are presented.

The first mesh is a coarse one of **42,648 elements** and it can be seen in Figure 5.2. $\Delta x_{min}/c$ and $\Delta y_{min}/c$ around the airfoil are 3×10^{-3} (679 elements around the airfoil). All the boundary conditions are located at $20C$ from the trailing edge of the airfoil. This mesh has been created from scratch manually.

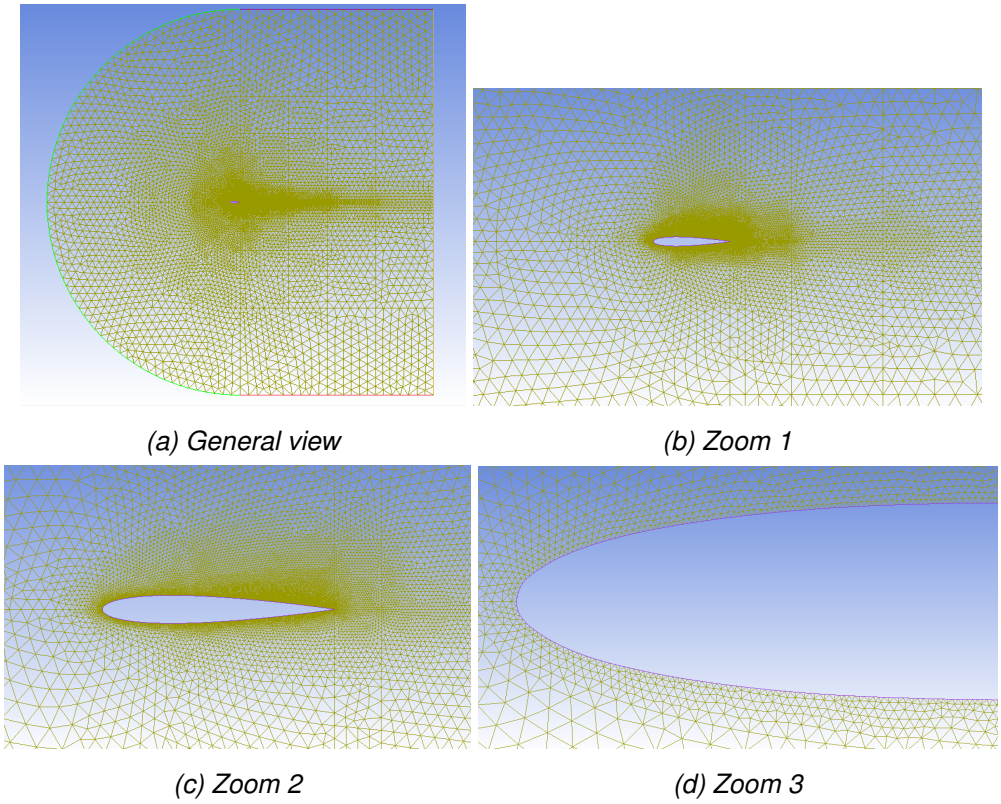

(a) General view *(b) Zoom 1*

(c) Zoom 2 *(d) Zoom 3*

Figure 5.2: Coarse mesh screenshots

The second mesh has been generated by a Matlab script created by Dr. Manel Soria and Engr. Arnau Miró. By modifying several parameters, the mesh is generated automatically. The result can be seen in Figure 5.3. It is a finer mesh than the previous one, with a total of **123,015 elements**. $\Delta x_{min}/c = 5.5 \times 10^{-3}$ and $\Delta y_{min}/c = 5 \times 10^{-3}$ around the airfoil (376 elements around the airfoil). The inlet is located at $10C$ from the airfoil, while the outlet at $15C$.

Although the coarse mesh is a little bit finer in the airfoil surface, it is expected that the finer mesh behaves better (specially at high angles of attack) since the wake is better defined there.

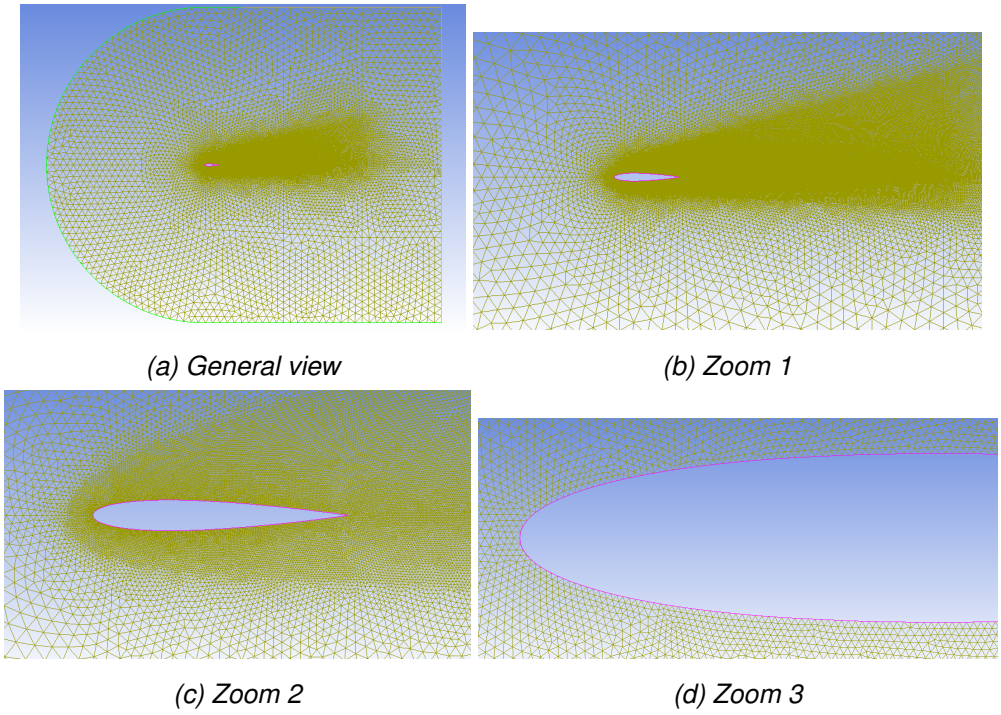

(a) General view *(b) Zoom 1*

(c) Zoom 2 *(d) Zoom 3*

Figure 5.3: Fine mesh screenshots

Since the flow is laminar, it is worth noting that the element dimension around the airfoil is not so important as long as the boundary layer is correctly characterized.

5.4 Diagnostics

Several diagnostic quantities can be computed from the flow as it evolves in time, allowing to validate the obtained results.

First of all, the lift and drag coefficients can be obtained. *Alya* returns both the pressure F_p and viscous F_v forces on a given boundary condition (i.e. the airfoil surface). Then, the **lift coefficient** can be computed as follows:

$$L = (F_{v_x} + F_{p_x})\sin\alpha + (F_{v_y} + F_{p_y})\cos\alpha \rightarrow C_l = \frac{L}{\frac{1}{2}\rho U_\infty^2 c} \tag{5.4.1}$$

Where c is the chord and ρ the density. The values of these variables are such that $Re = 5{,}000$ is set.

On the other hand, the **drag coefficient** is computed as:

$$D = (F_{v_x} + F_{p_x})\cos\alpha - (F_{v_y} + F_{p_y})\sin\alpha \rightarrow C_d = \frac{D}{\frac{1}{2}\rho U_\infty^2 c} \tag{5.4.2}$$

Both the lift and drag coefficient depend on time. By analyzing them, one can conclude from which time step (i_{steady}) the **simulation is steady** (oscillating around

a given value). From that moment on, the average C_l and C_d can be obtained as follows:

$$\begin{aligned} \bar{C}_l &= \frac{1}{\Delta_{t_{avg}}} \sum_{i=i_{steady}}^{N_f} C_{l_i} \cdot (t_i - t_{i-1}) \\ \bar{C}_d &= \frac{1}{\Delta_{t_{avg}}} \sum_{i=i_{steady}}^{N_f} C_{d_i} \cdot (t_i - t_{i-1}) \end{aligned} \tag{5.4.3}$$

Then, the root mean square coefficients can be also computed with the following expressions:

$$\begin{aligned} C_{l_{rms}} &= \sqrt{\frac{1}{\Delta_{t_{avg}}} \sum_{i=i_{steady}}^{N_f} (C_{l_i} - \bar{C}_l)^2 (t_i - t_{i-1})} \\ C_{d_{rms}} &= \sqrt{\frac{1}{\Delta_{t_{avg}}} \sum_{i=i_{steady}}^{N_f} (C_{d_i} - \bar{C}_d)^2 (t_i - t_{i-1})} \end{aligned} \tag{5.4.4}$$

From the values of C_l and C_d since the time to average (steady solution), the *plomb* Matlab function can be also used to obtain the **Lomb-Scargle power spectral density** as explained in [33]. See that *fft* cannot be used since the time steps are not constant. From the frequency f_{max} at which maximum energy density is obtained (using C_l), **Strouhal number** is obtained as:

$$St = f_{max} \frac{c}{U_\infty} \tag{5.4.5}$$

The power spectral density is also computed for the two probes located in the wake (see section 5.2) based on both components of the velocity.

It is important to note that all the plots are given in non-dimensional time:

$$TU = t \frac{U_\infty}{c} \tag{5.4.6}$$

Finally, since 101 witness points are located at the surface of the airfoil, pressure can be saved at each instant of time. Then, the pressure is averaged for each witness point and the **pressure coefficient** can be obtained at each location (x value) using the following formula:

$$c_p = \frac{p - p_0}{\frac{1}{2}\rho U_\infty^2} \tag{5.4.7}$$

Where p_0 is the reference pressure.

Chapter 6: NACA 0012 airfoil simulations: Without Active Flow Control

In order to have some reference cases (without active flow control), several angles have been simulated for the two aforementioned meshes (coarse and fine). Hereafter, several studies are carried out to show the correctness of the obtained results and the averaged flow patterns.

All the simulations performed without active flow control (2D flow) have had a total of 30,000 iterations, except at angle of attack of 0 degrees, where no oscillation occurs and it finishes before achieving 30,000 iterations.

6.1 Temporal stabilization

To decide when the flow is statistically stable and when we are able to integrate the results, C_l or C_d evolution in time can be used. When a steady oscillation is achieved on both aerodynamic parameters, it means that the flow is statistically stable. For instance, in Figure 6.1, it is safe to say that the flow is statistically stable from 20 time units.

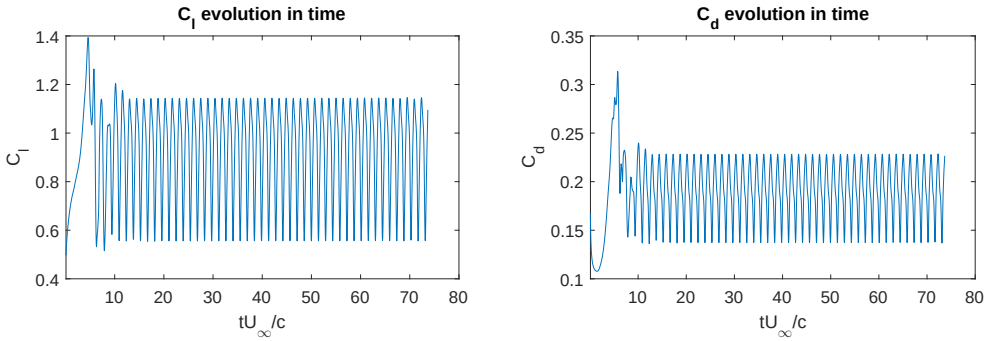

(a) Lift coefficient *(b) Drag coefficient*

Figure 6.1: Evolution of aerodynamic parameters in time for AOA=10 deg (fine mesh); (a) lift coefficient; (b) drag coefficient

It is worth highlighting that statistical steady state is reached at different time depending on the angle of attack. Stabilization usually occurs at later time instants for higher angles of attack. Anyway, temporal stabilization is decided case by case.

6.2 Mesh refinement study: Comparison of the main aerodynamic coefficients

In order to compare the different meshes, the following plots for different angles of attack are obtained:

- Averaged C_l vs α: See Figure 6.2.
- Averaged C_l vs C_d: See Figure 6.3a.
- Strouhal vs α: See Figure 6.3b.

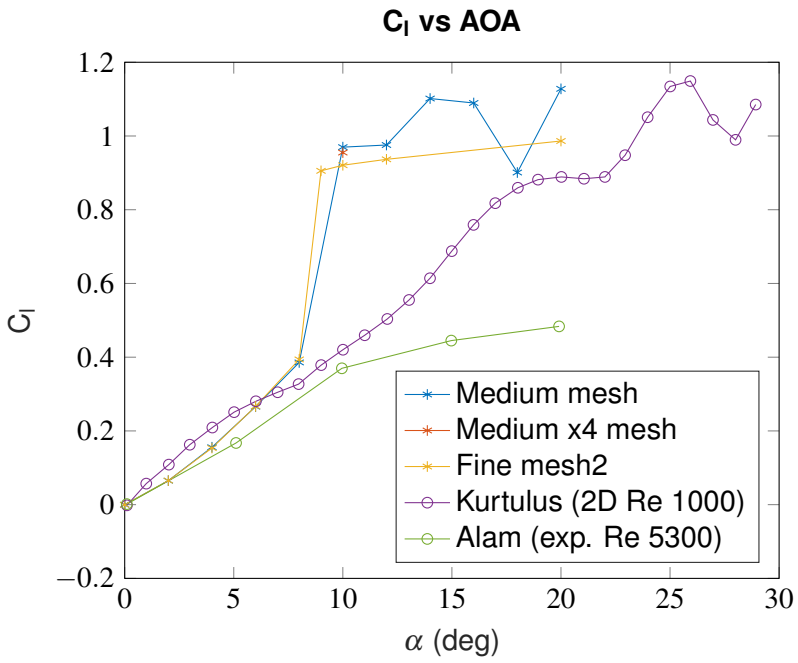

Figure 6.2: Cl vs AOA

In Figure 6.2, reference solutions are given (lines with circles): 2D at Re 1000 (Kurtulus [28]) and 3D experimental at Re 5300 (Alam et al. [27]). The other lines correspond to the present work for different type of meshes. Note that, from an angle of attack of 10 degrees, the present 2D solutions are quite different than the literature. However, it is important to highlight that we are comparing against either a different Reynolds number (Kurtulus [28]) or the experimental case, which is a 3D flow (Alam et al. [27]).

The fine mesh gives better results for high angles of attack. For small α, the results are nearly exact.

We have tested 10 degrees with several meshes (the red dot is the medium mesh with 4 times more DOFs) and similar results have been obtained (C_l around 0.9). These similar results can be observed in Table 6.1.

Thus, it is concluded that, at high angles of attack, the 2D solutions are not valid because the flow is fully 3D and the 2D case is not capable of reproducing the actual flow behavior.

In order to prove the theory that for high angles of attack, a 3D flow simulation has been performed by extruding the medium mesh (refined in the trailing edge) by 32 planes without any model. The lift coefficient evolution with time can be observed in Figure 6.11 (see section 6.4). Note how the 3D simulation gives an averaged lift (0.3735) which is nearly the same to the experimental 3D result (0.37) given by Alam et al. [27]. Thus, it seems quite clear that 2D flow is not valid for high angles of attack. However, it is worth noting that the 3D case also needs a mesh refinement study since only one mesh has been tested.

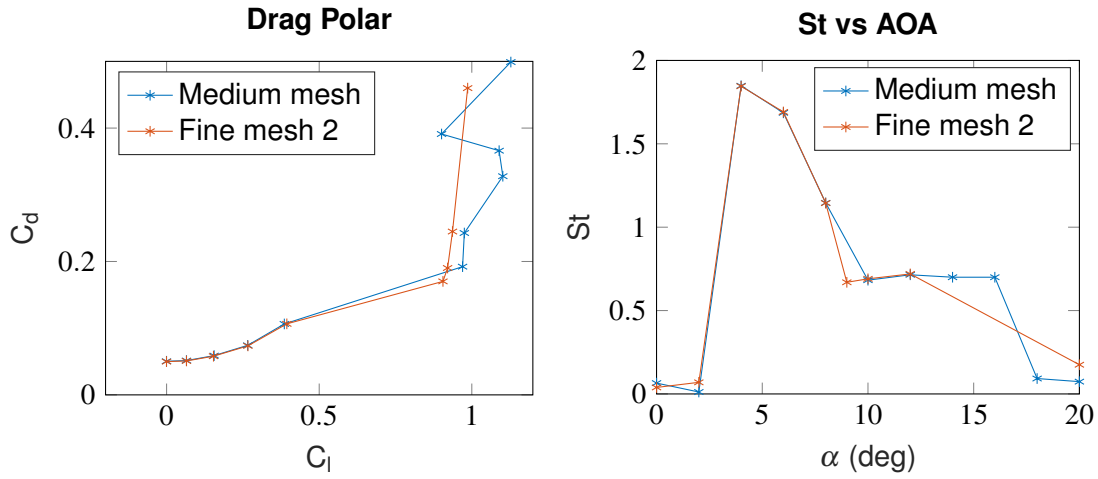

(a) Lift coefficient vs drag coefficient (drag polar)

(b) Non-dimensional vortex shedding frequency vs AOA

Figure 6.3: Drag polar and St for different angles of attack (two meshes)

Total elements	$\Delta_{x_{min}}$	$\Delta_{y_{min}}$	C_l	C_d
31,800	4.3×10^{-3}	4×10^{-3}	0.8958	0.1840
42,648 (coarse)	3×10^{-3}	3×10^{-3}	0.9698	0.1922
123,015 (fine)	5.5×10^{-3}	5×10^{-3}	0.9207	0.1902
170,592 (coarse x 4)	1.5×10^{-3}	1.5×10^{-3}	0.9550	0.1940

Table 6.1: Aerodynamic coefficients compared with different meshes (AOA=10 deg)

6.3 Numerical results

In this section, the main numerical results of the fine mesh are given. These results consist on the averaged flow patterns (via streamlines), instantaneous flowfields, pressure coefficient distributions and energy spectra analysis. The exact values of the aerodynamic coefficients are also provided.

In Table 6.2, the reader can observe the exact results (aerodynamic coefficients) of the fine mesh.

AOA	C_l	C_d	$C_{l_{rms}}$	$C_{d_{rms}}$	St
0	-3.28×10^{-4}	4.99×10^{-2}	3.28×10^{-4}	4.99×10^{-2}	3.90×10^{-2}
2	6.52×10^{-2}	5.09×10^{-2}	6.52×10^{-2}	5.09×10^{-2}	6.96×10^{-2}
4	1.54×10^{-1}	5.80×10^{-2}	1.54×10^{-1}	5.80×10^{-2}	1.85×10^{0}
6	2.66×10^{-1}	7.35×10^{-2}	2.69×10^{-1}	7.35×10^{-2}	1.69×10^{0}
8	3.94×10^{-1}	1.06×10^{-1}	4.20×10^{-1}	1.08×10^{-1}	1.14×10^{0}
9	9.11×10^{-1}	1.71×10^{-1}	9.37×10^{-1}	1.73×10^{-1}	6.64×10^{-1}
10	9.21×10^{-1}	1.90×10^{-1}	9.40×10^{-1}	1.92×10^{-1}	6.90×10^{-1}
12	9.37×10^{-1}	2.45×10^{-1}	9.53×10^{-1}	2.47×10^{-1}	7.20×10^{-1}
20	9.86×10^{-1}	4.60×10^{-1}	1.04×10^{0}	4.75×10^{-1}	1.75×10^{-1}

Table 6.2: Table of results for simulations without AFC (fine mesh)

As it can be seen, the root mean square values of both C_l and C_d are quite similar to the average values. It is also interesting to see that the maximum Strouhal number occurs at AOA=4 deg. Obviously, the bigger the angle of attack, the greater the lift and drag coefficients.

6.3.1 Averaged flow patterns

In order to completely understand the behavior of the flow around the airfoil, streamlines plots can be used. In Figure 6.4, it can be observed streamlines of the mean velocities for different angles. These plots correspond to the fine mesh, but they are really similar in the coarse mesh.

From these plots, it can be observed that a recirculation bubble is formed at low angles of attack at the trailing edge. As commented also by Kurtulus [28], this recirculation bubble moves towards the leading edge as the angle of attack increases. It can be seen that, for small angles, there is trailing edge separation. Around 12 degrees, we can consider that the flow has totally entered the stall regime.

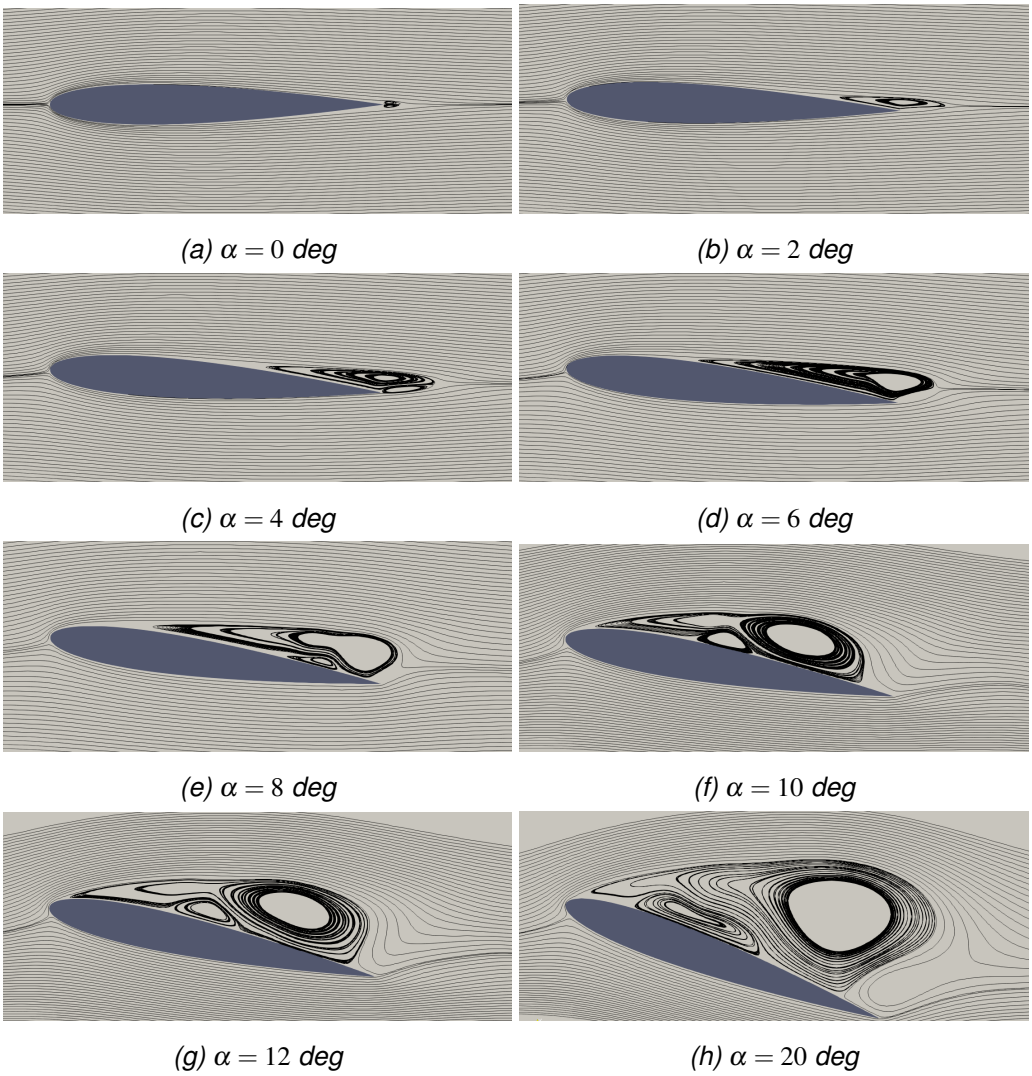

(a) $\alpha = 0$ *deg* *(b)* $\alpha = 2$ *deg*

(c) $\alpha = 4$ *deg* *(d)* $\alpha = 6$ *deg*

(e) $\alpha = 8$ *deg* *(f)* $\alpha = 10$ *deg*

(g) $\alpha = 12$ *deg* *(h)* $\alpha = 20$ *deg*

Figure 6.4: Streamlines of mean velocity field for different angles of attack (fine mesh)

6.3.2 Instantaneous flowfields

As an example of the flow when no active flow control is applied, the instantaneous flowfields at different instants for an angle of attack of 10 degrees are plotted in Figure 6.5. The selected instants are a representation of one cycle of the flow. As it can be seen, the flow is nearly stalled at this angle of attack. Note also the huge vortex located at the trailing edge, which is thought to be a numerical result of the 2D simulation.

6.3.3 Pressure coefficient distribution

Pressure coefficient plots are also of great usefulness to understand how much lift a given angle of attack produces. In Figure 6.6, the reader can observe pressure coefficient plots for several angles of attack (averaged in time for the fine mesh).

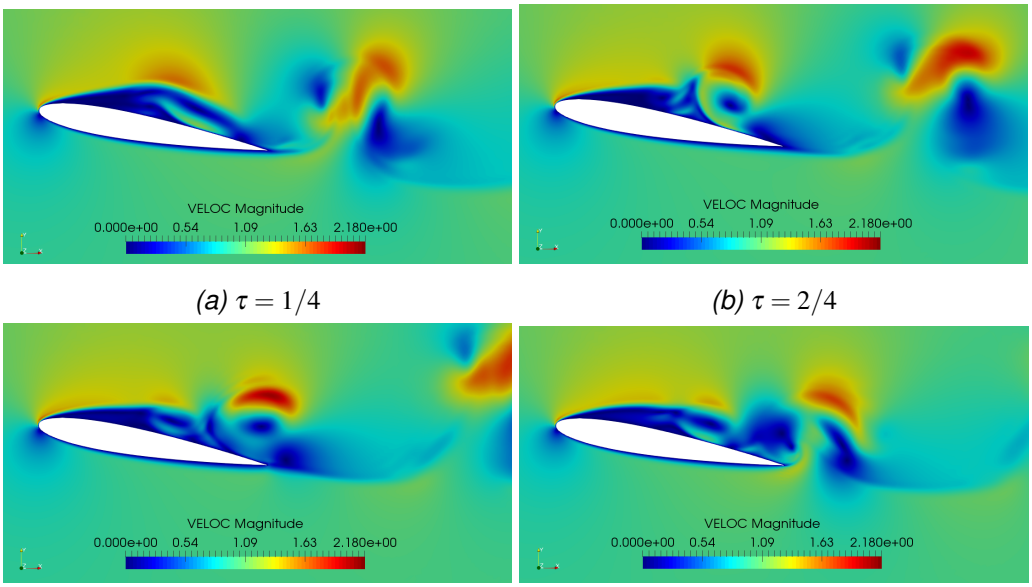

(a) $\tau = 1/4$ *(b)* $\tau = 2/4$

(c) $\tau = 3/4$ *(d)* $\tau = 4/4$

Figure 6.5: Instantaneous flowfields without using AFC for an AOA=10 deg

It is shown that for 0 degrees, both the suction and pressure sides have the same distribution as it is expected for a symmetric airfoil at AOA=0. The results obtained from potential flow theory are depicted in Figure 6.7. The main difference is located at the trailing edge since the potential theory does not predict the small separation of the flow that occurs close to the trailing edge of the airfoil. Note that the higher the angle of attack, the worse results predict the potential flow theory.

It is interesting to observe the inverse c_p distribution for both $\alpha = 2$ and $\alpha = 4$ degrees. This phenomenon has been also observed in the literature for this type of NACA airfoil (i.e. Kojima et al. [6]). The reasons explaining this inverse distribution are two: the large thickness of the airfoil (not observed on the NACA0002, for instance) and the trailing-edge separation that occurs for these angles; the flow from the pressure surface side goes to the suction surface side around the trailing edge leading to a negative c_p value.

Note also that for bigger angles of attack than 10 degrees, a bump on the suction side appears. This is mainly caused by the numerical anomalies caused by the 2D simulations, which should not be present on a 3D flow.

6.3.4 Streamwise velocity profiles

In order to analyze the size of the separated boundary layer and its reattachment, streamwise averaged velocity profiles are an excellent way. In this case, we have

inspected the streamwise velocity at four different locations (same as [34]): $x/c = 0.3$, $x/c = 0.6$, $x/c = 0.9$ and $x/c = 1.2$.

As it can be observed in Figure 6.8, the bigger the angle of attack, the closer to the leading edge the separation occurs; big angles of attack have separation at $x/c = 0.3$ and $x/c = 0.6$ while the smallest ones have more detachment near the trailing edge. See also that the size of the separated boundary is always smaller for small angles of attack.

6.3.5 Energy spectra

A probe has been located in the wake (above trailing edge) in order to capture the peaks of frequency due to the velocity. The result for the most significant angles of attack can be seen in Figure 6.9. Note that the probe has been moved to the correct place according to the angle of attack as it is shown in Table 5.1.

The present flow is known to be governed by two kinds of organized modes [29]: the von Kármán and the shear layer (Kelvin-Helmholtz instability) modes. With the aid of Figure 6.9, we can observe the first mode.

The period-doubling mechanism of the von Kármán mode appears repeatedly as the Reynolds number increases (at Re 800: one peak, at Re=1300: two peaks... [29]), yielding peaks in powers of 2. At $Re = 5000$, a multitude of subharmonic peaks appear as it can be observed in Figure 6.9 due to the von Kármán mode.

A simulation for an angle of attack of 10 degrees has been run at Reynolds 1600 to show that only 4 peaks should appear (probe located above trailing edge). As it can be observed in Figure 6.10, we have verified that only 4 peaks appear, as said by Hoarau et al. [29].

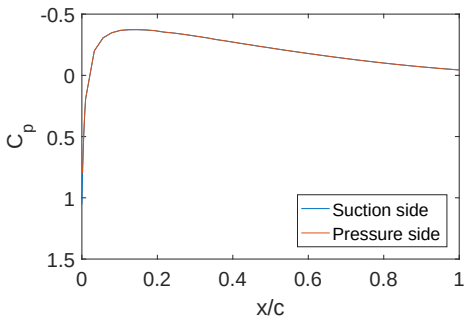

(a) $\alpha = 0$ *deg*

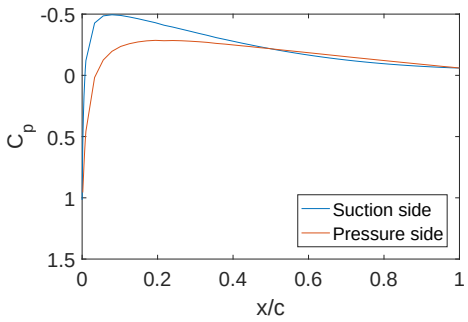

(b) $\alpha = 2$ *deg*

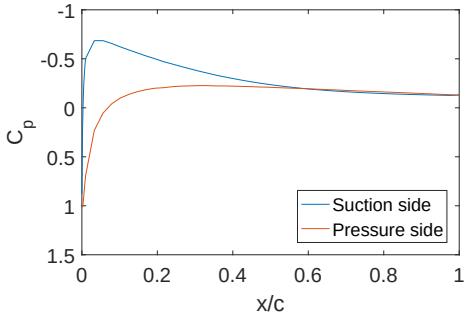

(c) $\alpha = 4$ *deg*

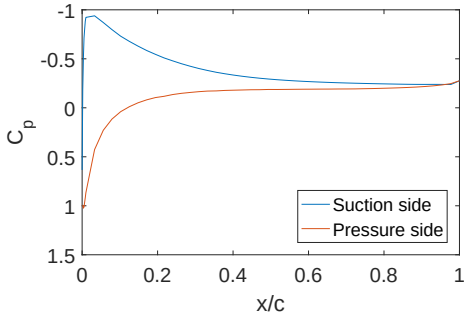

(d) $\alpha = 6$ *deg*

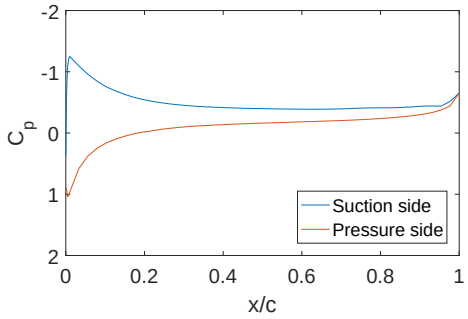

(e) $\alpha = 8$ *deg*

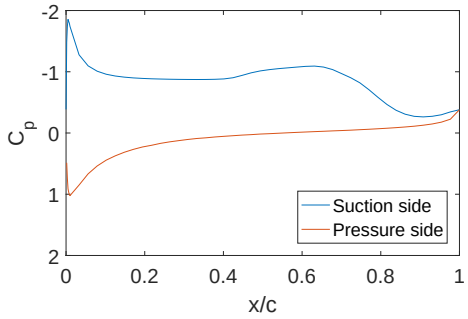

(f) $\alpha = 10$ *deg*

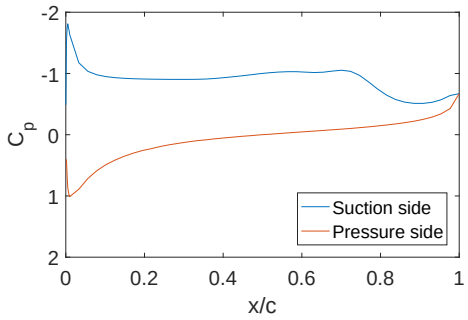

(g) $\alpha = 12$ *deg*

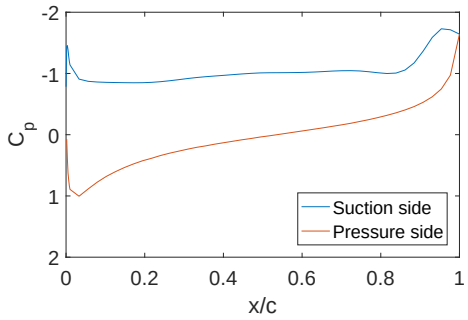

(h) $\alpha = 20$ *deg*

Figure 6.6: Pressure coefficient distributions for different angles (fine mesh)

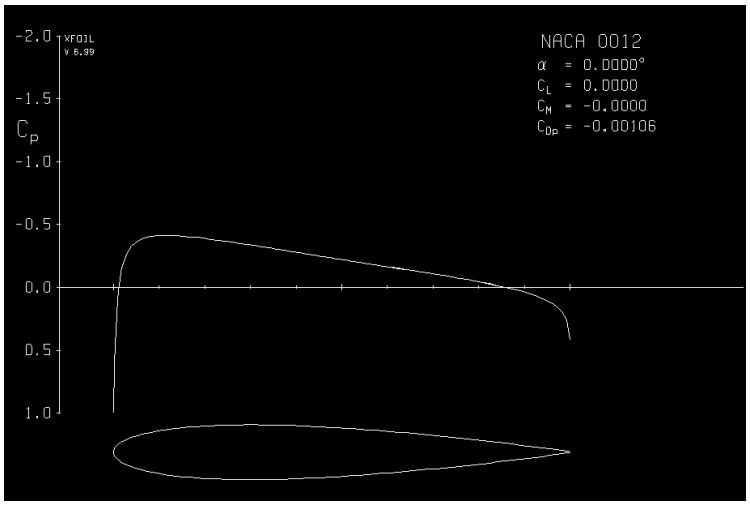

Figure 6.7: Pressure coefficient distribution at $\alpha = 0$ deg according to XFOIL

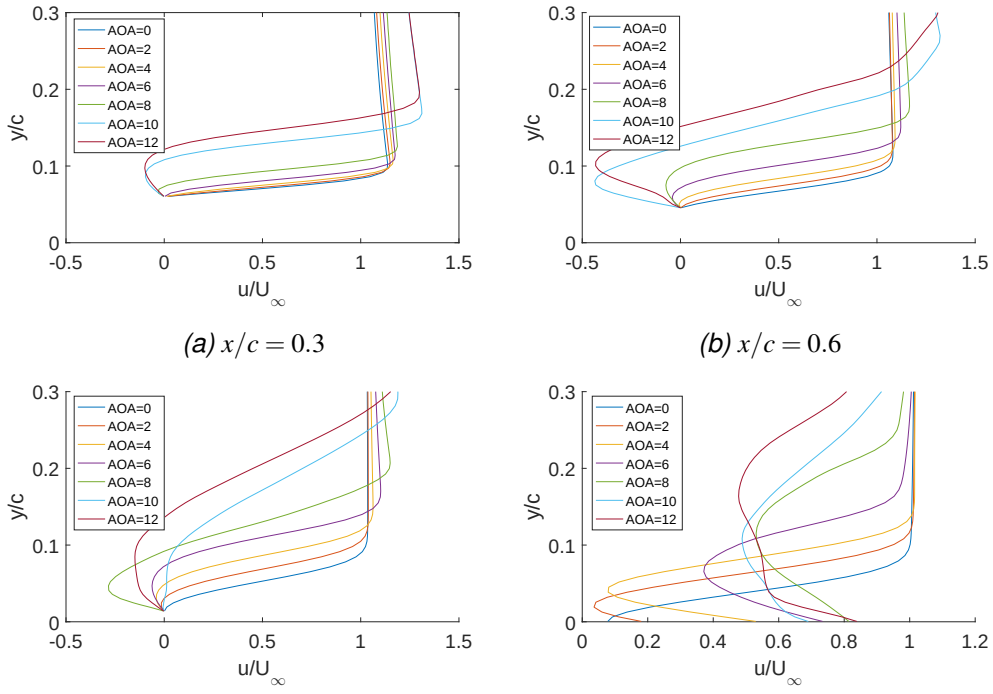

(a) $x/c = 0.3$ *(b)* $x/c = 0.6$

(c) $x/c = 0.9$ *(d)* $x/c = 1.2$

Figure 6.8: Streamwise velocity profiles (average flow) close to the airfoil surface (a,b,c) and in the near wake (d) (fine mesh)

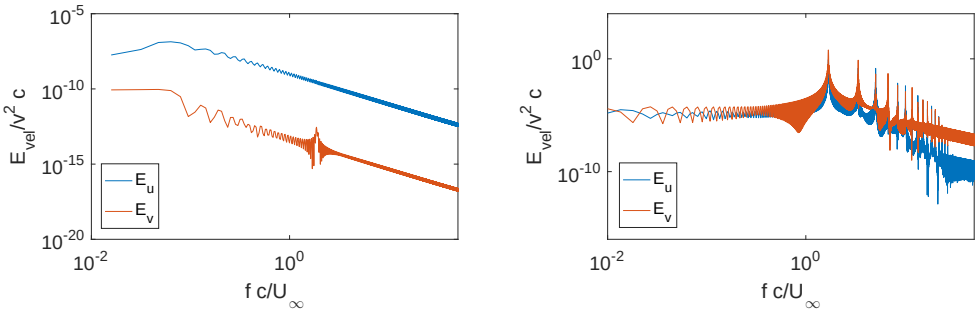

(a) $\alpha = 2$ deg

(b) $\alpha = 6$ deg

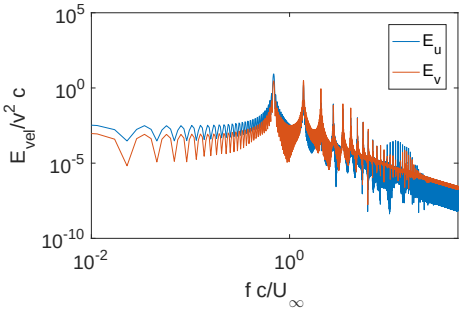

(c) $\alpha = 10$ deg

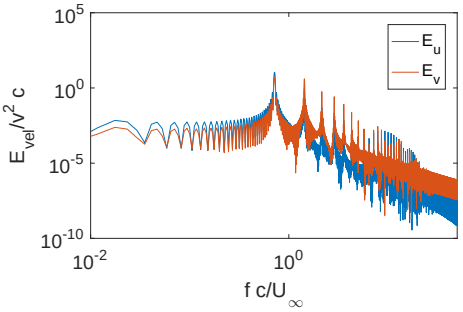

(d) $\alpha = 12$ deg

Figure 6.9: Single-Sided Amplitude Spectrum of velocities for a probe located in the wake (fine mesh)

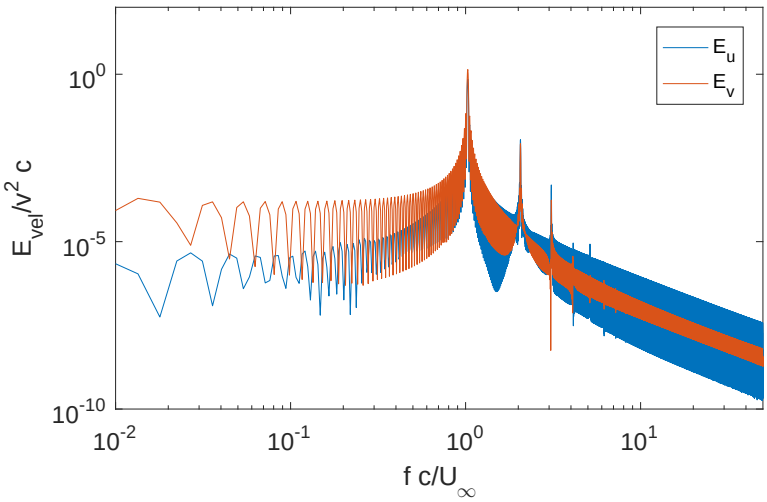

Figure 6.10: Energy spectrum for velocities at Re=1600 and AOA=10 deg (probe 2)

6.4 3D simulation

Since it has been observed that the 2D lift coefficient at AOA=10 deg departs from the experimental results, a 3D flow simulation is performed by extruding the medium mesh (refined in the trailing edge, which ends in a plane of 54000 DOFs) in 32 planes. This leads to a mesh with 1.7 million DOFs. Such a big mesh is costly to be simulated but it is necessary to extrude the mesh in at least 32 planes to obtain 3D structures.

The performed simulation has a skew-symmetric convective scheme and a time integration of RK-3. No turbulence model has been imposed.

The evolution of the lift coefficient can be observed in Figure 6.11. Note that the oscillatory response is not so perfect as in the 2D cases, but the averaged lift coefficient (**0.3735**) completely coincides with the experimental results of Alam et al. at $Re = 5,300$ [27] (0.37).

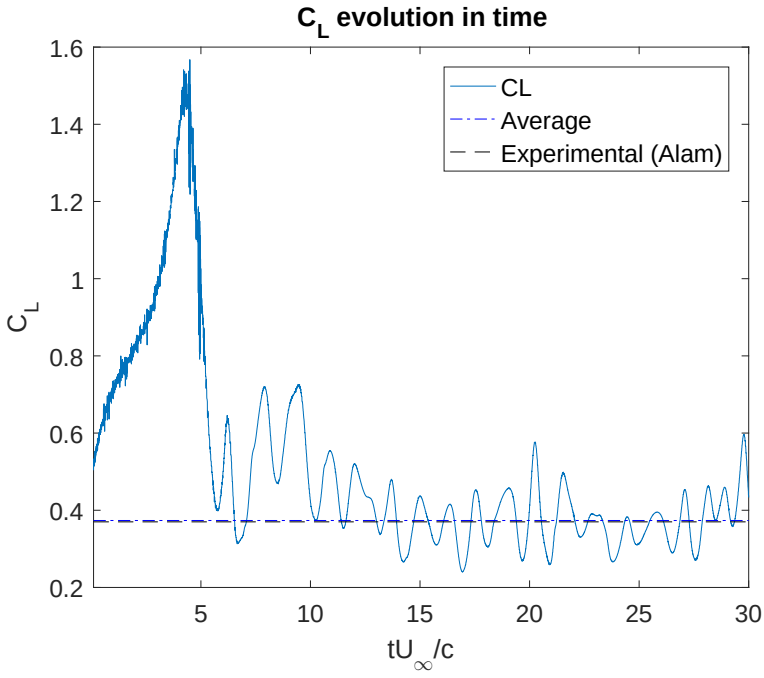

Figure 6.11: 3D lift coefficient vs time at AOA=10 deg

In Figure 6.12, both the drag coefficient and the single-sided amplitude spectrum can be observed. The exact averaged and root mean square aerodynamic coefficients are given in Table 6.3. All the aforementioned results are averaged from $TU = 15$.

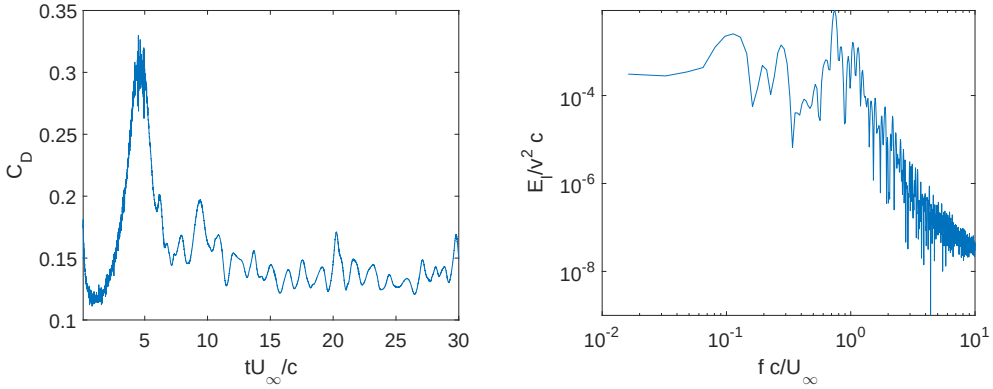

(a) 3D drag coefficient vs time *(b) 3D Single-Sided Amplitude Spectrum*

Figure 6.12: 3D drag coefficient and Strouhal spectrum at AOA=10 deg

Variable	Result
$\overline{C_L}$	3.7348×10^{-1}
$C_{L_{rms}}$	3.7960×10^{-1}
$\overline{C_D}$	1.3655×10^{-1}
$C_{D_{rms}}$	1.3690×10^{-1}
St	7.4506×10^{-1}

Table 6.3: Aerodynamic coefficients of the 3D simulation at an AOA=10 deg

Besides the fact that the 2D lift coefficient was completely wrong, the drag coefficient has been also reduced when a 3D flow has been considered (from 0.190 to 0.135). The Strouhal number has been slightly increased respect to the 2D simulation.

When looking into the pressure coefficient distribution, it is clear why the 2D simulation at an angle of attack of 10 degrees is completely wrong (see Figure 6.13). The absolute values of c_p are not correct for the 2D simulation. Moreover, the bump on the suction side is also due to the 2D anomalies.

The streamlines of the mean velocity field for the 3D simulation can be observed in Figure 6.15. As it can be observed, in contrast to the 2D simulation, the airfoil is already in stall at 10 degrees (no recirculation).

In Figure 6.14, the single-side spectrums of a probe located in the wake are depicted. The 2D spectrum clearly shows the vortex pairing, which is typical of a 2D flow, where the vortices do not dissipate by the vortex stretching mechanism. Therefore, there are infinite harmonics in the 2D spectrum. On the other hand, the vortex shedding (frequency at which the shear layer of the suction side interact

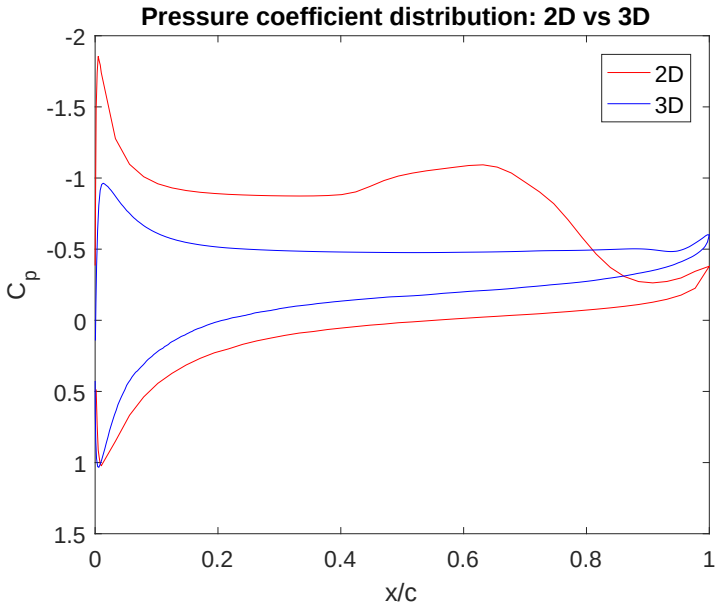

Figure 6.13: Pressure coefficient distribution (2D vs 3D) at an AOA=10 deg

with the ones of the trailing edge) can be seen on the 3D simulation. The non-dimensional vortex shedding frequency of the 3D simulation is 1.11 vs 0.69 of the 2D simulation. The frequency is higher in 3D since the shear layers are closer and the recirculation is less (interacting at a higher frequency than the 2D flow).

In bluff bodies, the vortex shedding frequency is somehow inversely proportional to the vertical separation between the shear layers. Thus, from the obtained energy spectra, it can be already deduced that the 3D wake would be more narrow than the 2D wake.

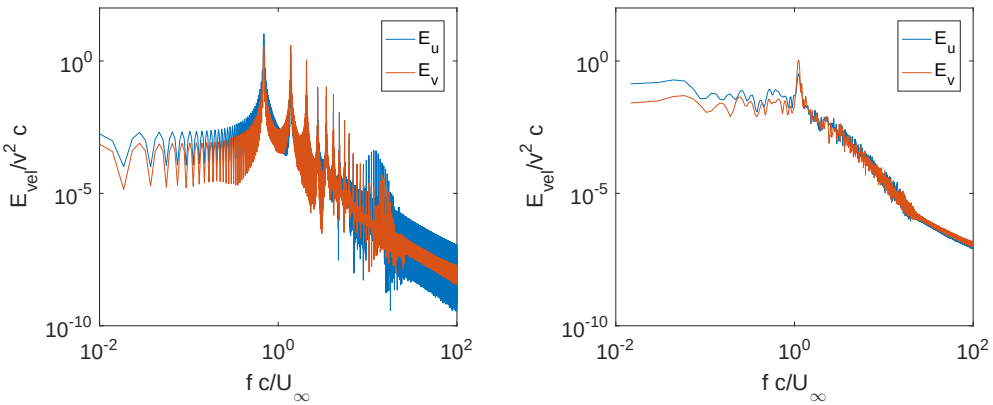

(a) 2D simulation *(b) 3D simulation*

Figure 6.14: Wake spectrum of velocities at AOA=10 deg

Finally, in order to better observe the 3D structures, the Q-criterion is depicted

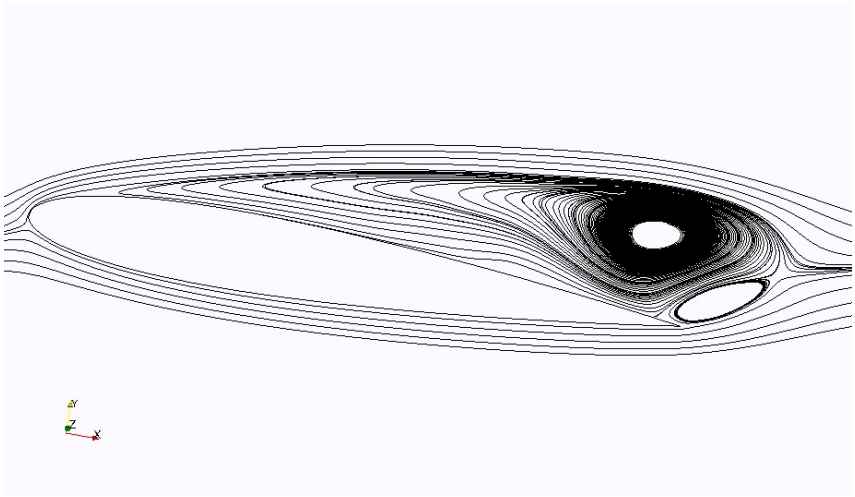

Figure 6.15: 3D streamlines of mean velocity field for an AOA=10 deg

in Figure 6.16 at a given instant of time ($TU = 33$). Note the 'rib' structures that always finish on the 'tunnel' vortices until they start to break.

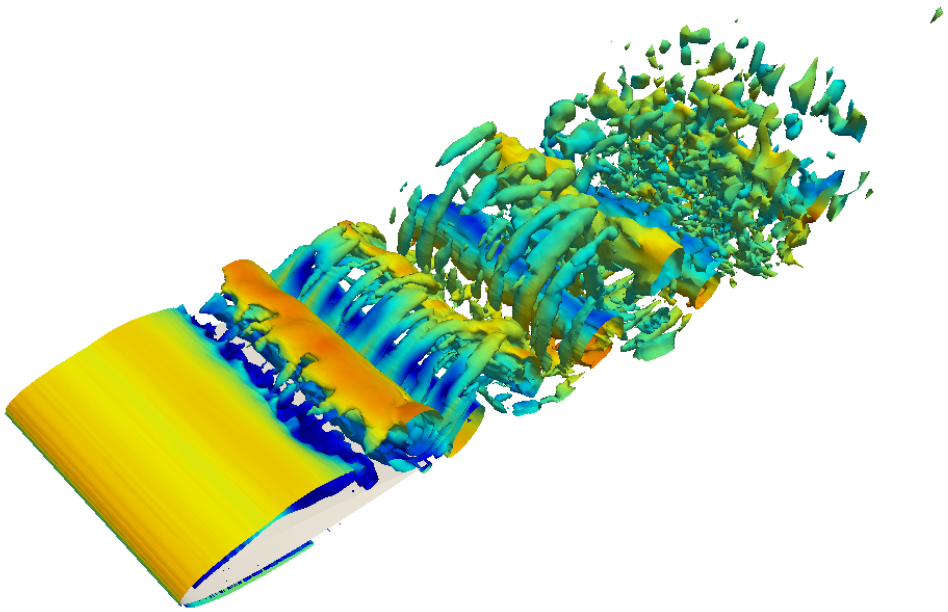

Figure 6.16: 3D instantaneous Q-criterion isocontour ($Q = 5$) colored by velocity magnitude for an AOA=10 deg

Chapter 7: NACA 0012 airfoil simulations: Active Flow Control

The aim of this section is to apply Active Flow Control to the studied NACA 0012 airfoil. Specifically, we consider angles of attack of 6 and 10 degrees. AOA=10 deg is the beginning of stall for this type of airfoil and 2D simulations depart from 3D ones at this angle of attack. Thus, AOA=6 deg cases are also simulated since they are more realistic. Note that, in order to be efficient, AFC has to be applied in the zone of maximum lift (stall region).

7.1 Computational Mesh

From the studied reference cases (see chapter 6), it can be observed that separation occurs at around $x/c = 0.06$ from the leading edge. Thus, the actuator has to be placed at that location or a little bit closer to the leading edge.

The mesh designed to simulate AFC can be seen in Figure 7.1. The exact location of the center of the actuator is $x/c = 0.057$ **from the leading edge**. The width of the actuator is $h/c = 0.00748$. In order to completely solve the region of the actuator, the number of nodes have been increased by a factor of 10 in that region with an hyperbolic transition to the surrounding airfoil surface.

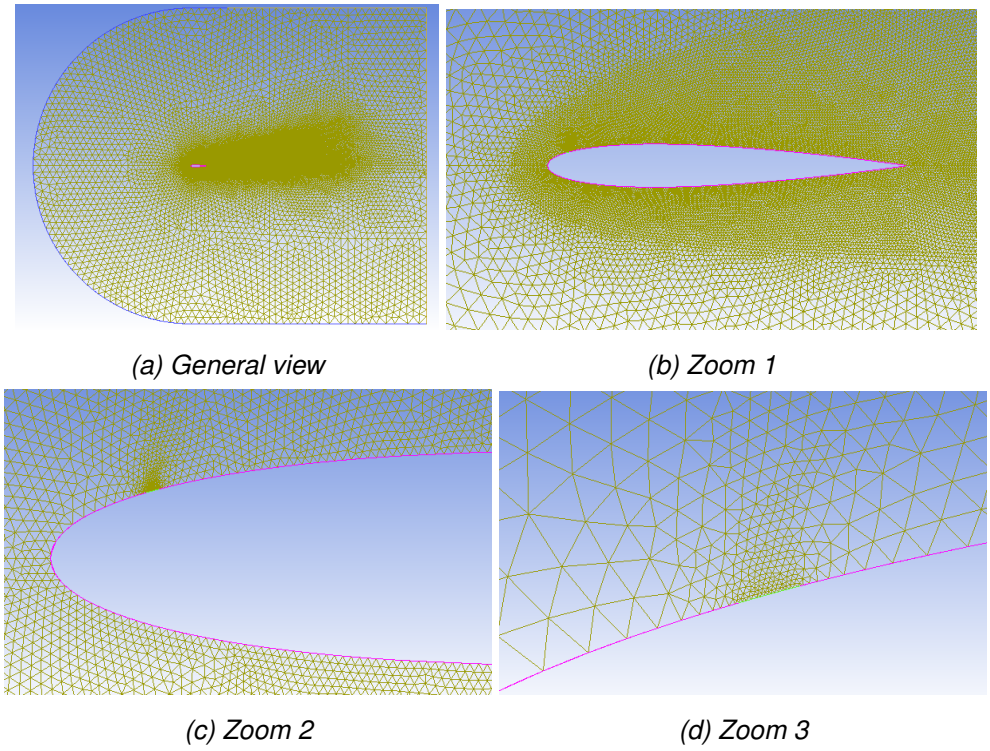

(a) General view *(b) Zoom 1*

(c) Zoom 2 *(d) Zoom 3*

Figure 7.1: Mesh for Active Flow Control (screenshots)

7.2 Implementation of the active flow control on the CFD code

There is quite controversy about the optimal non-dimensional frequency F^+. Some authors say that, for applications such as flow separation control over an airfoil, it should be in the order of 1 [9]. Others claim that up to order 10 should work [35]. In this report, several frequencies are tested as indicated in Table 7.1. The formula for the dimensionless frequency is the following one:

$$F^+ = f\frac{x_{te}}{U_\infty} \tag{7.2.1}$$

Thus, for a determined location of the actuator and known free-stream velocity, the actuation frequency f is readily set.

Moreover, as shown in the literature [14], jet momentum coefficients C_μ must be at least 0.002. In this report, we define C_μ as in You and Moin [13] and we have tested five values: $C_\mu = 0.001, 0.0025, 0.005, 0.0075, 0.01$ (see Table 7.1):

$$C_\mu = \frac{h(\rho u_{max}^2)\sin\theta_j}{c(\rho U_\infty^2)} \tag{7.2.2}$$

where h and θ_j are the width of the actuator cavity and the jet angle with respect to the airfoil surface. Taking a value of $\theta_j = 30$ deg, the necessary peak bulk jet

velocity u_{max} can be obtained.

You and Moin define the following boundary condition to mimic the oscillatory motion of a piston engine in the experiment of reference [9]. This is also the boundary condition that has been used in this study over the airfoil surface:

$$(u,v,w) = A_p U_\infty \sin(2\pi f t)[\cos\alpha, -\sin\alpha, 0] \tag{7.2.3}$$

The maximum of this function is given by the expression $A_p U_\infty$, which has to be equal to u_{max}. Thus, the exact implemented boundary condition depending on time t is:

$$(u,v,w) = u_{max} \sin(2\pi f t)[\cos\alpha, -\sin\alpha, 0] \tag{7.2.4}$$

7.3 Definition of the cases

In Table 7.1, the reader can observe all the simulated cases (both $\alpha = 6$ and $\alpha = 10$) with Active Flow Control. To characterize the level of flow control in the boundary layer, two main parameters are studied: the **momentum coefficient** C_μ and the **non-dimensional frequency** F^+.

AOA (deg)	C_μ	u_{max}/U_∞	F^+
6 & 10	0.005	1.1562	0.85
6 & 10	0.005	1.1562	1
6 & 10	0.005	1.1562	1.15
6 & 10	0.005	1.1562	2
6 & 10	0.005	1.1562	5
6 & 10	0.005	1.1562	10
6 & 10	0.005	1.1562	15
6	0.001	0.517088	1
6 & 10	0.0025	0.8176	1
6 & 10	0.0075	1.4161	1
6 & 10	0.01	1.6352	1

Table 7.1: Definition of the AFC cases

The results from the aforementioned cases are given in the following sections.

7.4 Methodology assessment

Before starting to analyze the results of the cases in detail, it is necessary to see if the results obtained with the present methodology are realistic. In Figure 6.2, we

have already seen that, for AOA=10 deg, the results depart from the 3D literature results. Thus, hereafter, we want to confirm that the results are not valid for this angle of attack when the 2D flow hypothesis is used.

In Figure 7.2 and Figure 7.3, the main aerodynamic coefficients depending on both the dimensionless frequency and momentum coefficient can be respectively seen for an angle of attack of 6 degrees. The dash lines represent the case without active flow control. These results have been averaged from $TU = 15$.

It can be clearly seen that only the cases of a dimensionless frequency less than 2 do increase the lift-to-drag relation in our case. This means, that these cases where F^+ is less than 2 produce a considerable increase of lift coefficient and decrease of drag coefficient. It is also interesting to observe that the Strouhal number follows quite well the dimensionless frequency. On the other hand, from the different tested momentum coefficients, $C_\mu = 0.0025$ produces a slightly better lift-to-drag relation. There is no sense in reducing less than 0.0025 the momentum coefficient.

The same plots have been depicted for an angle of attack of 10 degrees (see Figure 7.4 and Figure 7.5, averaged from $TU = 20$). However, there is no clear tendency on the aforementioned plots and we cannot trust them since 10 degrees simulations should be carried out considering 3D as previously mentioned (see section 6.4). Otherwise, the 3D structures that occur at this angle of attack are not correctly solved.

For the reasons mentioned above, it has been decided that the detailed results (section 7.5) will be only given for 6 degrees in the 2D simulations. The results for AOA=6 deg are valid even when simulating in 2D.

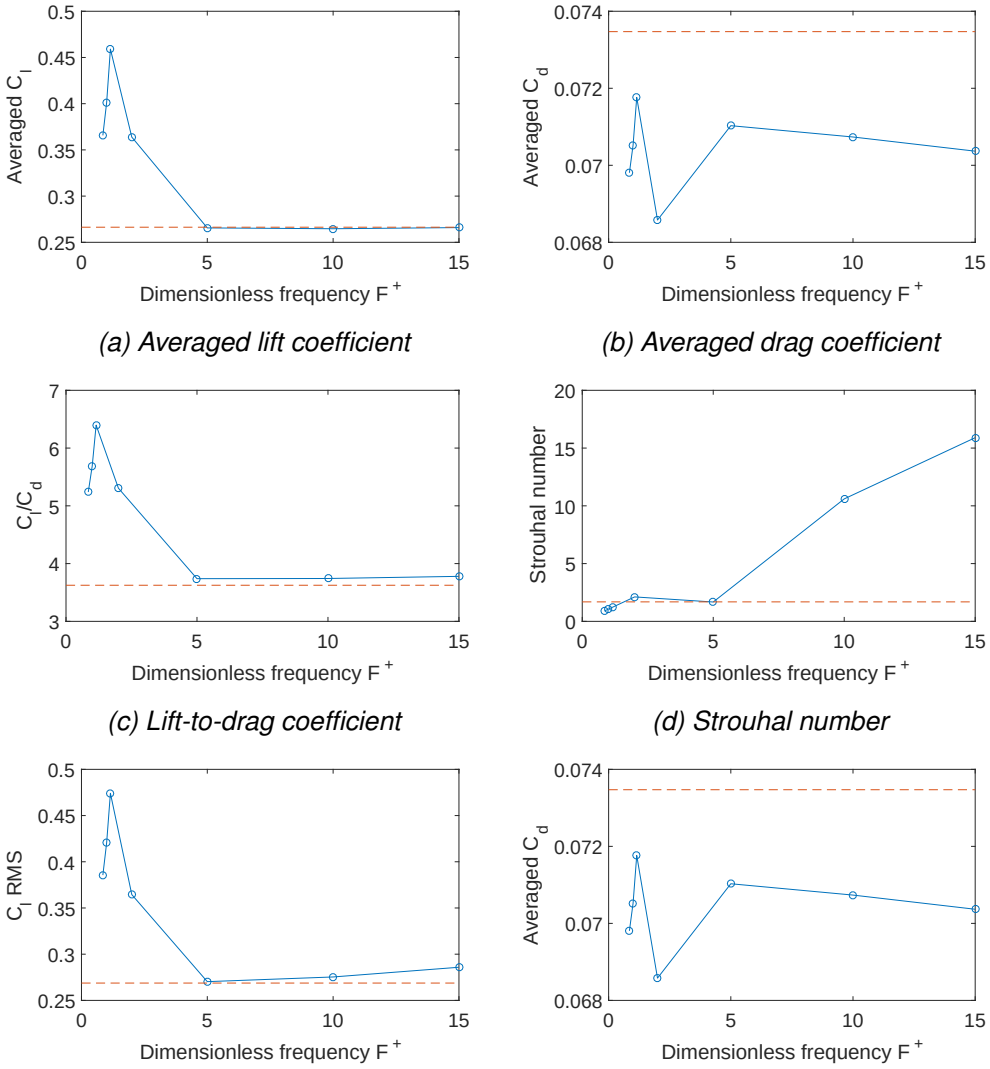

(a) Averaged lift coefficient

(b) Averaged drag coefficient

(c) Lift-to-drag coefficient

(d) Strouhal number

(e) Root mean square lift coefficient

(f) Root mean square drag coefficient

Figure 7.2: Effect of dimensionless frequency on main coefficients for AOA=6 deg ($C_\mu = 0.005$)

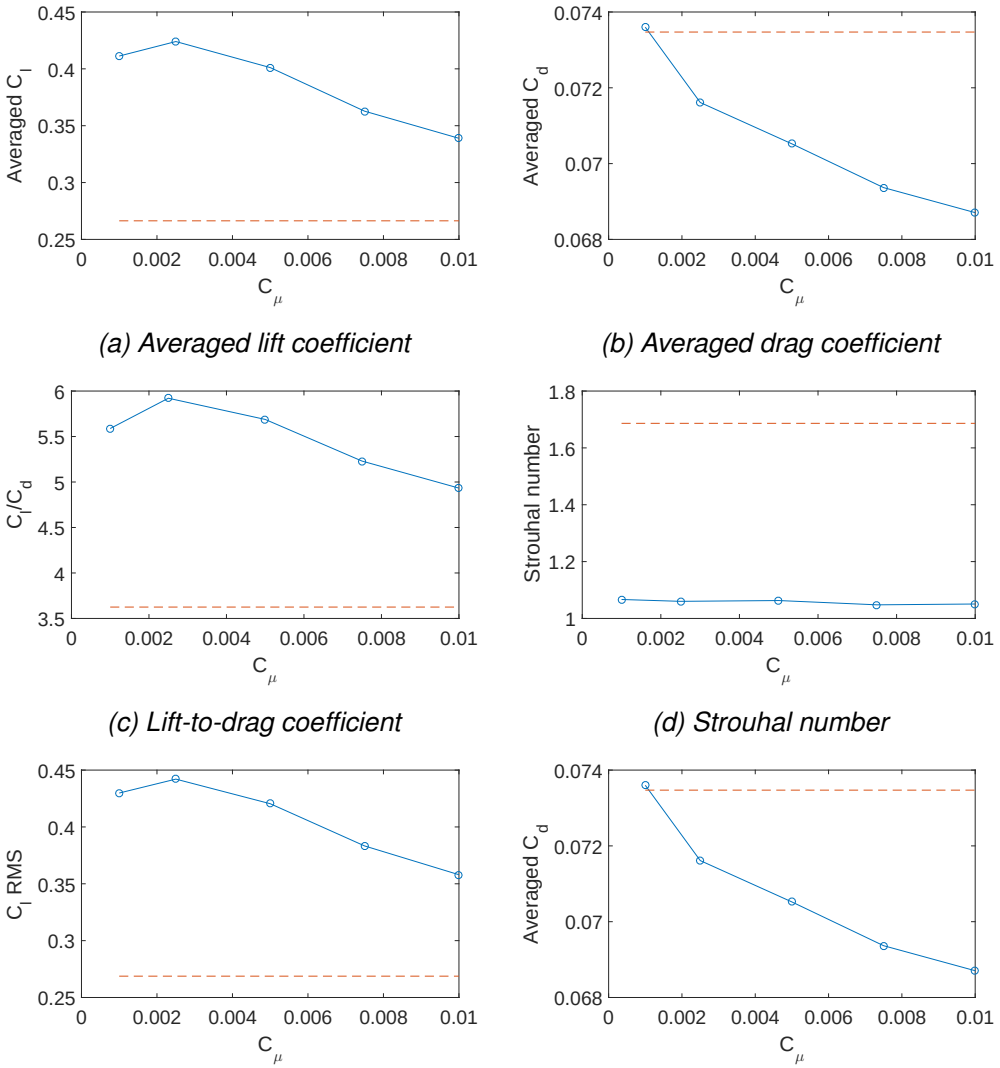

(a) Averaged lift coefficient

(b) Averaged drag coefficient

(c) Lift-to-drag coefficient

(d) Strouhal number

(e) Root mean square lift coefficient

(f) Root mean square drag coefficient

Figure 7.3: Effect of momentum coefficient on main coefficients for AOA=6 deg ($F^+ = 1$)

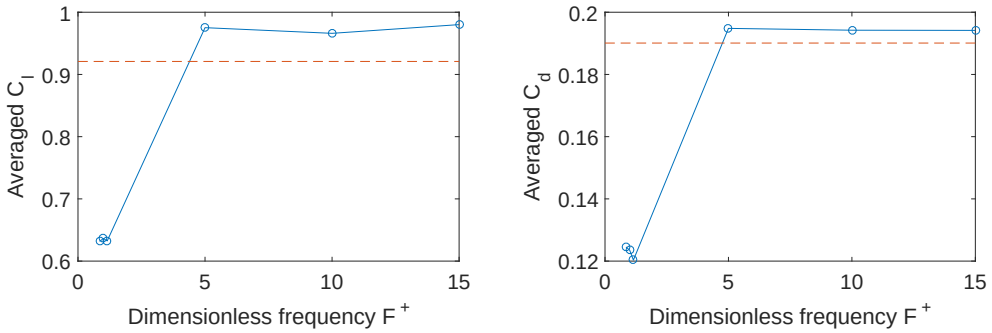

(a) Averaged lift coefficient

(b) Averaged drag coefficient

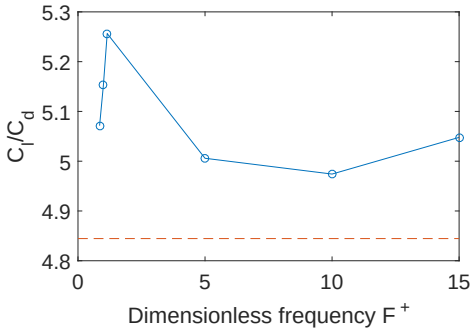

(c) Lift-to-drag coefficient

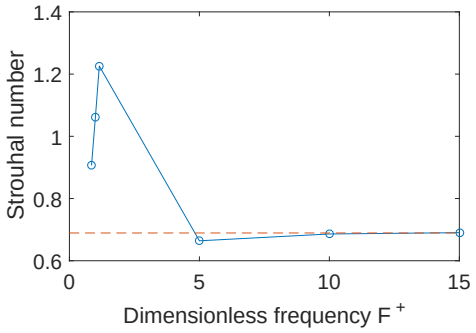

(d) Strouhal number

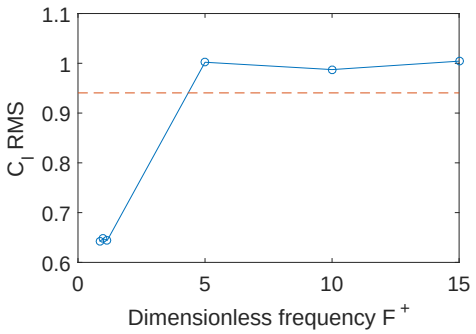

(e) Root mean square lift coefficient

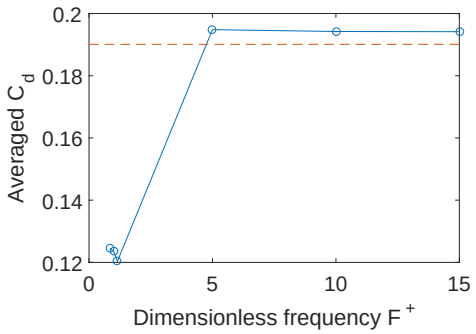

(f) Root mean square drag coefficient

Figure 7.4: Effect of dimensionless frequency on main coefficients for AOA=10 deg ($C_\mu = 0.005$)

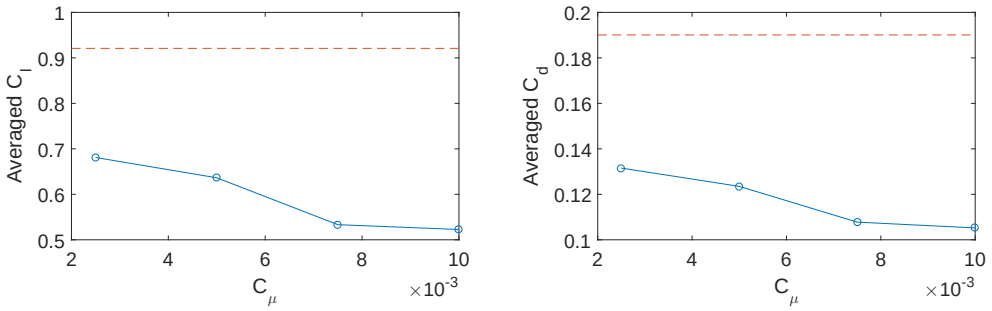

(a) Averaged lift coefficient

(b) Averaged drag coefficient

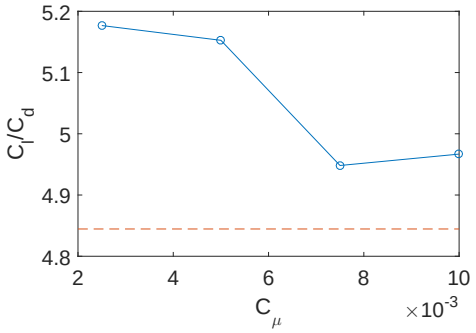

(c) Lift-to-drag coefficient

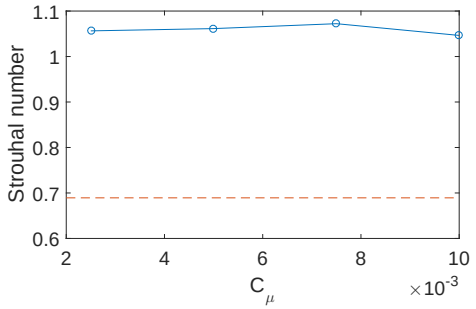

(d) Strouhal number

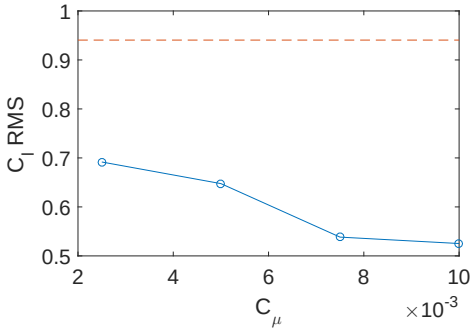

(e) Root mean square lift coefficient

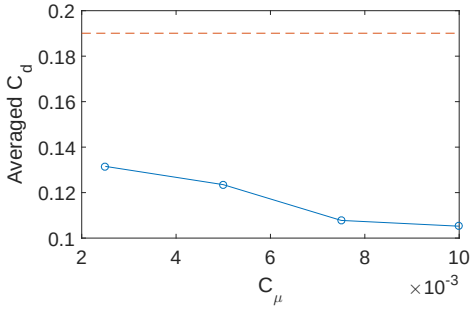

(f) Root mean square drag coefficient

Figure 7.5: Effect of momentum coefficient on main coefficients for AOA=10 deg ($F^+ = 1$)

7.5 Numerical results

In this section, the main numerical results from the cases presented in Table 7.1 are detailed. The same variables/plots as chapter 6 are studied.

In Table 7.2, the reader can observe the exact results (aerodynamic coefficients) of the cases presented in Table 7.1. Only the simulations of AOA=6 deg are provided since AOA=10 deg should be performed considering 3D flow.

C_μ	F^+	C_l	C_d	$C_{l_{rms}}$	$C_{d_{rms}}$	St
No AFC	-	2.66×10^{-1}	7.35×10^{-2}	2.69×10^{-1}	7.35×10^{-2}	1.69
0.001	1	4.11×10^{-1}	7.36×10^{-2}	4.30×10^{-1}	7.47×10^{-2}	1.07
0.0025	1	4.24×10^{-1}	7.16×10^{-2}	4.42×10^{-1}	7.30×10^{-2}	1.06
0.005	0.85	3.66×10^{-1}	6.98×10^{-2}	3.86×10^{-1}	7.09×10^{-2}	0.90
0.005	1	4.01×10^{-1}	7.05×10^{-2}	4.20×10^{-1}	7.22×10^{-2}	1.06
0.005	1.15	4.59×10^{-1}	7.18×10^{-2}	4.74×10^{-1}	7.26×10^{-2}	1.22
0.005	2	3.64×10^{-1}	6.86×10^{-2}	3.64×10^{-1}	6.89×10^{-2}	2.12
0.005	5	2.66×10^{-1}	7.10×10^{-2}	2.70×10^{-1}	7.15×10^{-2}	1.68
0.005	10	2.65×10^{-1}	7.07×10^{-2}	2.75×10^{-1}	7.17×10^{-2}	10.6
0.005	15	2.66×10^{-1}	7.04×10^{-2}	2.86×10^{-1}	7.22×10^{-2}	15.9
0.0075	1	3.63×10^{-1}	6.94×10^{-2}	3.83×10^{-1}	7.11×10^{-2}	1.05
0.01	1	3.39×10^{-1}	6.87×10^{-2}	3.58×10^{-1}	7.05×10^{-2}	1.05

Table 7.2: Table of results for simulations with AFC (AOA=6 deg)

These results have been discussed in the previous sections. However, observe that the RMS values are quite similar to the averaged ones. Note also that the Strouhal number usually follows the dimensionless frequency of the actuator.

The following conclusions can be obtained from the above table:

- The maximum lift coefficient is obtained with $C_\mu = 0.005$ and $F^+ = 1.15$, which produces an **increase on the lift coefficient of 72.56%** respect to the reference case. This case is followed by $C_\mu = 0.0025$ and $F^+ = 1$. $F^+ > 5$ does not produce any improvement on the lift coefficient.

- The minimum drag coefficient is obtained with $C_\mu = 0.005$ and $F^+ = 2$, which gives a **decrease of 6.67%** respect to the reference case. A really low momentum coefficient does not reduce the drag coefficient at all.

- From these results, the best lift-to-drag ratio is obtained with $C_\mu = 0.005$ and $F^+ = 1.15$, which achieves a 6.40 ratio vs 3.63 from the reference case (a **76.48% increase**).

- Similar results are obtained if looking into the root mean square values.

7.5.1 Averaged flow pattern comparison

By depicting the streamlines of the mean velocity for an angle of attack of 6 degrees, it can be seen that the maximum reattachment occurs for $F^+ = 1$ (Figure 7.6) and $C_\mu = 0.0025$ (Figure 7.7). On both figures, the non-actuated case is also shown.

In any case, besides the small differences when changing F^+ and C_μ values, all actuated cases behave quite well when reattaching the flow. This could have been also deduced from Figure 7.2 and Figure 7.3 or Table 7.2, where a reduction in drag and an increase in lift are observed.

The actuation with 10 degrees is also shown in Figure 7.8 ($F^+ = 1$ and $C_\mu = 0.005$). Although it can be also seen that the flow is reattached, the exact result figures cannot be trusted because of the effect of 2D simulations for such an angle of attack.

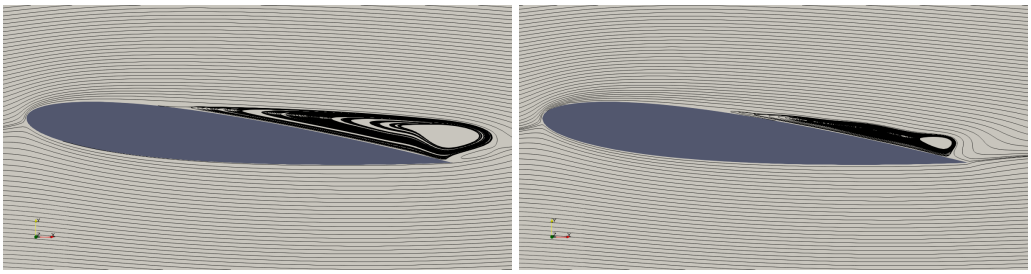

(a) No Active Flow Control *(b) $F^+ = 0.85$*

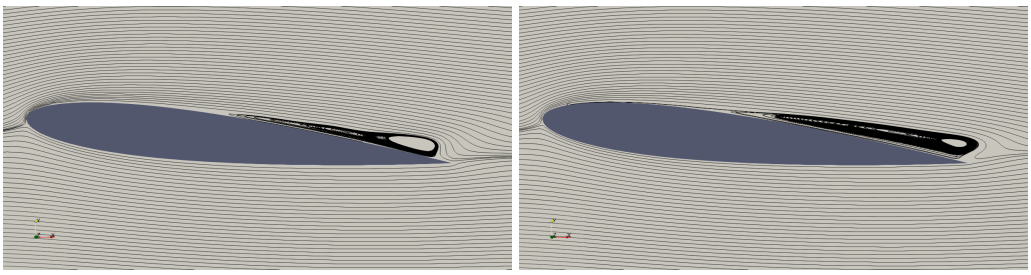

(c) $F^+ = 1$ *(d) $F^+ = 2$*

Figure 7.6: Streamlines of mean velocity field at AOA=6 deg for AFC with $C_\mu = 0.005$

7.5.2 Instantaneous flowfields

In Figure 7.9, the reader can observe that the actuator considerably attaches the flow to the airfoil surface if compared with Figure 6.5. The shown instants of time are representative of each cycle of the flow.

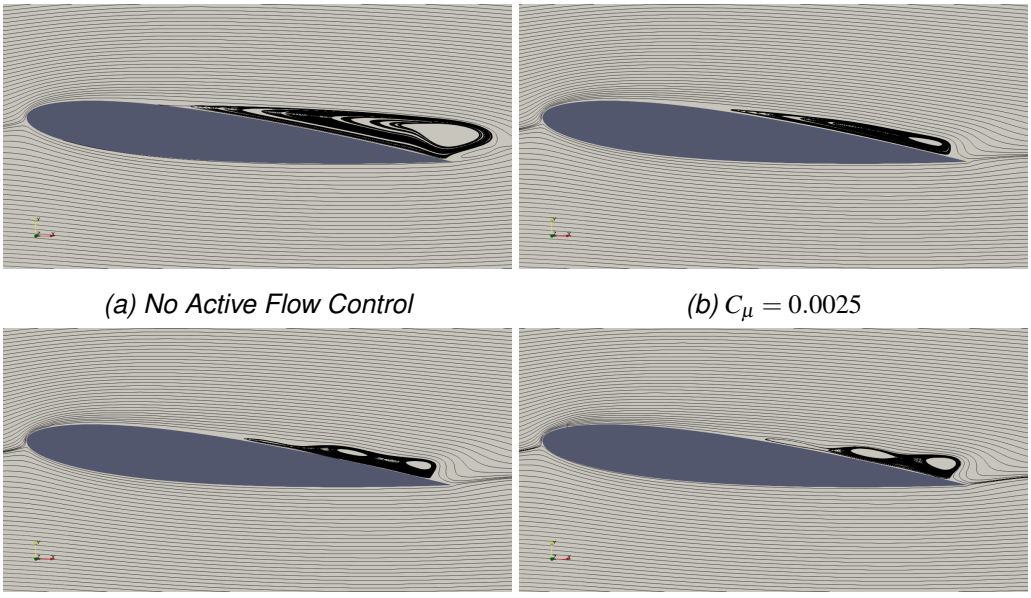

(a) No Active Flow Control *(b)* $C_\mu = 0.0025$

(c) $C_\mu = 0.0075$ *(d)* $C_\mu = 0.01$

Figure 7.7: Streamlines of mean velocity field at AOA=6 deg for AFC with $F^+ = 1$

In Figure 7.9d, it can be seen the actuator near the leading edge (discontinuity in velocity) expelling fluid. In Figure 7.9b, the fluid is suctioned by the actuator. It is quite impressive that so much reattachment can be achieved with an oscillatory motion of the same order of the free-stream velocity.

7.5.3 Pressure coefficient distribution

In Figure 7.11, it can be observed the pressure coefficient distribution for different values of F^+. All the cases increase the total lift coefficient (pressure and suction curves are further from each other). We can see that $F^+ = 1.15$ produces a slightly higher lift coefficient. Observe also the sudden decrease of C_p on the zone of the actuator (leading edge).

On the other hand, in Figure 7.12, the reader can observe how the momentum coefficient affects the pressure coefficient distribution. Note that the decrease of C_p on the zone of the actuator is smaller for less momentum coefficient (up to $C_\mu = 0.0025$), meaning that more lift coefficient can be produced.

Observing the pressure coefficient distributions, there is an increase in the lift coefficient, for all the actuated cases. However, it is clear that $F^+ = 1.15$ (for $C_\mu = 0.005$ Figure 7.11) and $C_\mu = 0.0025$ (for $F^+ = 1$ Figure 7.12) produce a better distribution. This is in line with all the results previously mentioned in this section.

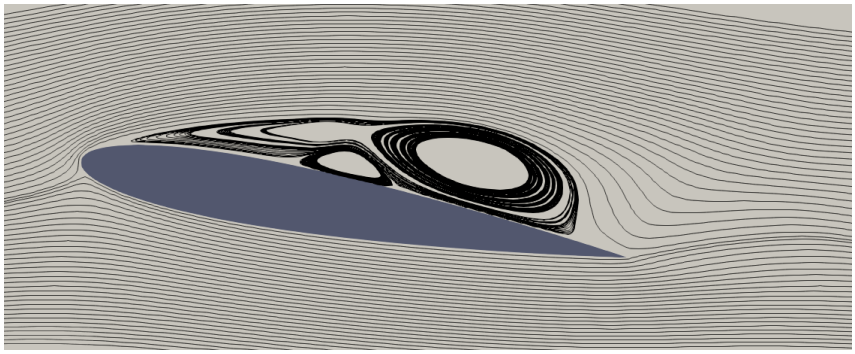

(a) Without Active Flow Control

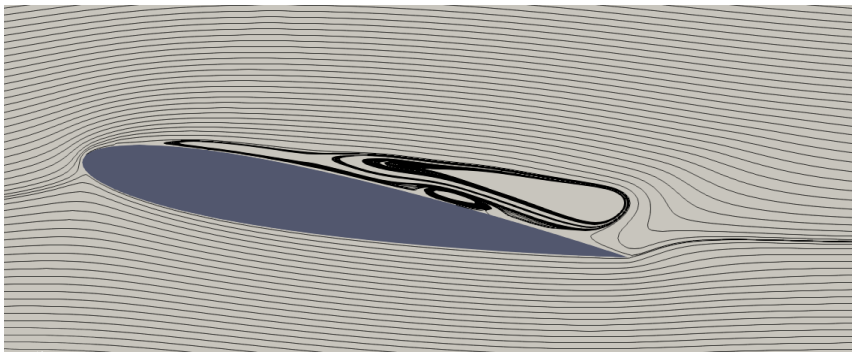

(b) With Active Flow Control

Figure 7.8: Streamlines of mean velocity field at AOA=10 deg with and without AFC

7.5.4 Streamwise velocity profiles

Similarly to subsection 6.3.4, the streamwise velocity profiles for the different actuated cases are compared with the non-actuated case (dashed line) for an angle of attack of 6 degrees. Figure 7.13 corresponds to different values of dimensionless frequency and Figure 7.14 to different values of momentum coefficient.

On both figures, it can be clearly seen that at $x/c = 0.3$, the flow is still fully attached to the airfoil for this angle of attack. On $x/c = 0.6$, only the non-actuated case is deattached while all the cases with active flow control produce an attached flow. From the rest of positions ($x/c = 0.9$ and $x/c = 1.2$) the worst frequency (of the depicted ones) is $F^+ = 5$, while the worst momentum coefficient is 0.01. These values produce a too big boundary layer. The values that produce the smallest size of the boundary layer is $F^+ = 1.15$ and $C_\mu = 0.0025$. This completely coincides with the results presented above in this section.

7.5.5 Energy spectra

Finally, in Figure 7.10, the reader can observe the energy spectra for two probes located on both the leading and trailing edge (see Table 5.1 for the exact location at

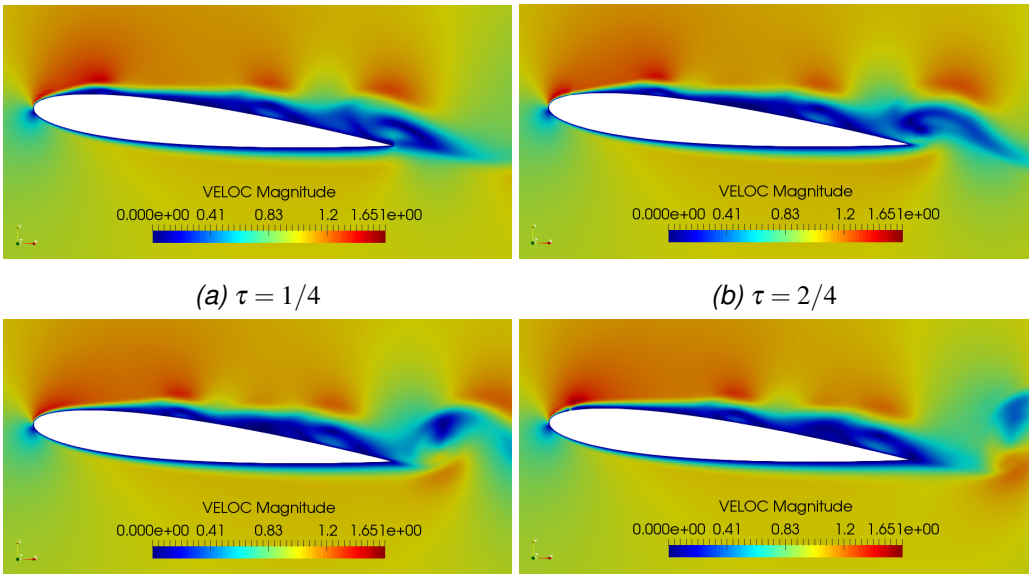

(a) $\tau = 1/4$ *(b)* $\tau = 2/4$

(c) $\tau = 3/4$ *(d)* $\tau = 4/4$

Figure 7.9: Instantaneous flowfields for AOA=6 deg using AFC ($F^+ = 1$ *and* $C_\mu = 0.005$*)*

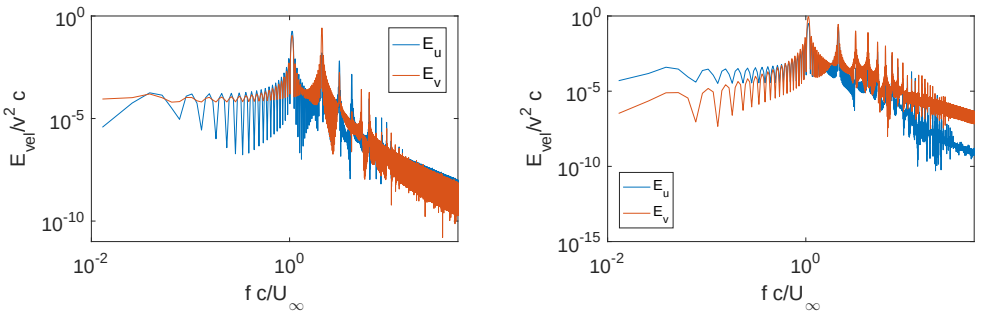

(a) Probe near the leading edge *(b) Probe near after the trailing edge*

Figure 7.10: Single-Sided Amplitude Spectrum of velocities for AOA=6 deg ($F^+ = 1$ *and* $C_\mu = 0.005$*)*

an angle of attack of 6 degrees). As it can be seen, a lot of frequencies are present due to the vortex pairing. The amplitude of the oscillations of the second probe is much bigger than the one located on the leading edge where the flow is completely attached to the airfoil surface.

The differences in the spectrum plots between different values of F^+ and C_μ are not so big to include all the plots herein, so only $F^+ = 1$ and $C_\mu = 0.005$ spectrum is provided. Note that the level of the peaks are slightly smaller than the ones without active flow control, if compared with the same angle of attack (see Figure 6.9b).

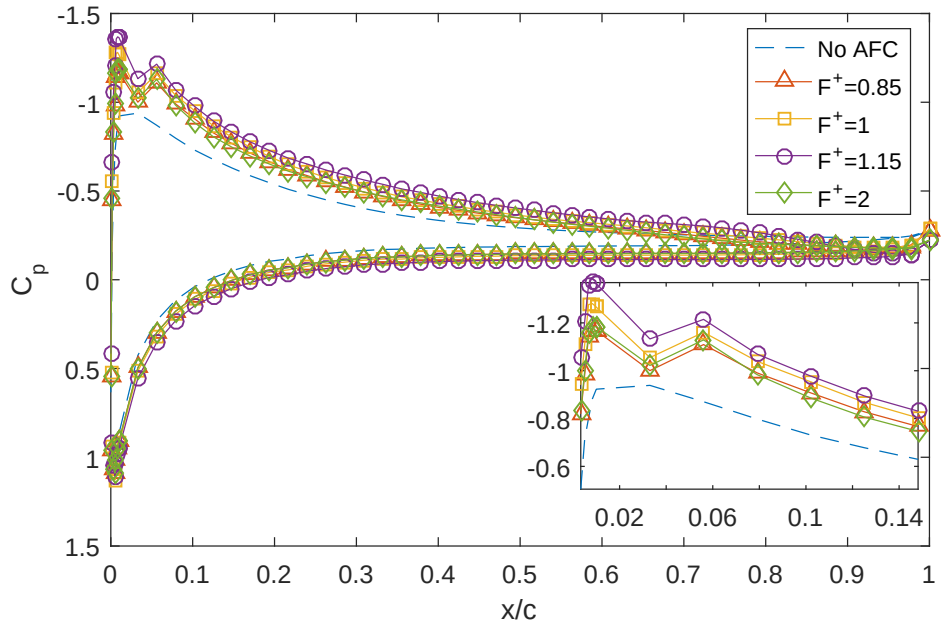

Figure 7.11: Pressure coefficient distribution using AFC (varying F^+ at $C_\mu = 0.005$) at $\alpha = 6$ deg

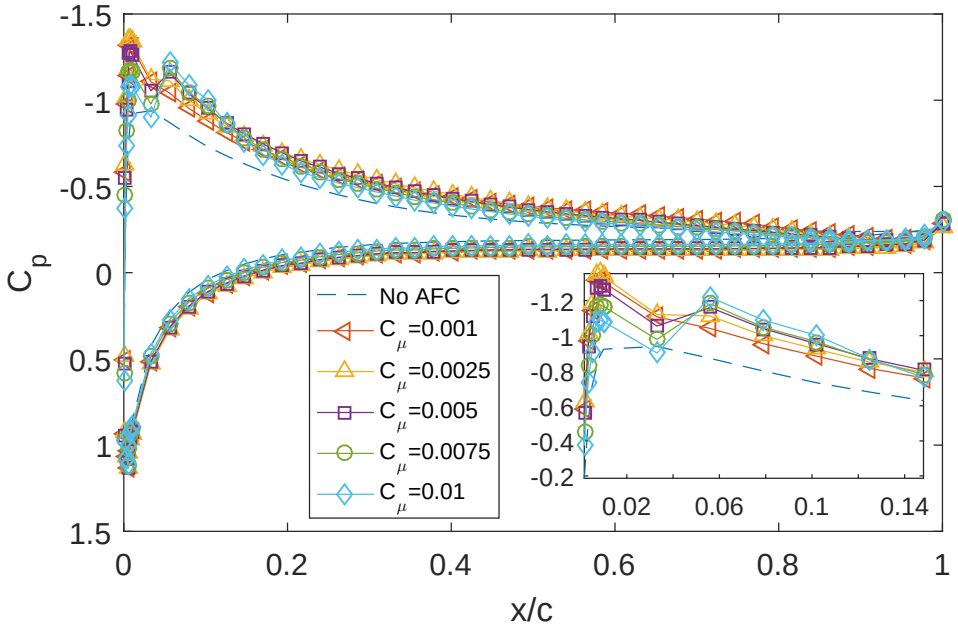

Figure 7.12: Pressure coefficient distribution using AFC (varying C_μ at $F^+ = 1$) at $\alpha = 6$ deg

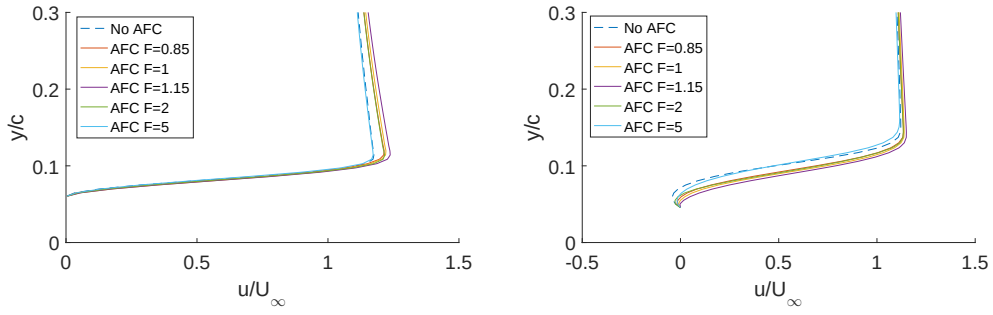

(a) $x/c = 0.3$ (b) $x/c = 0.6$

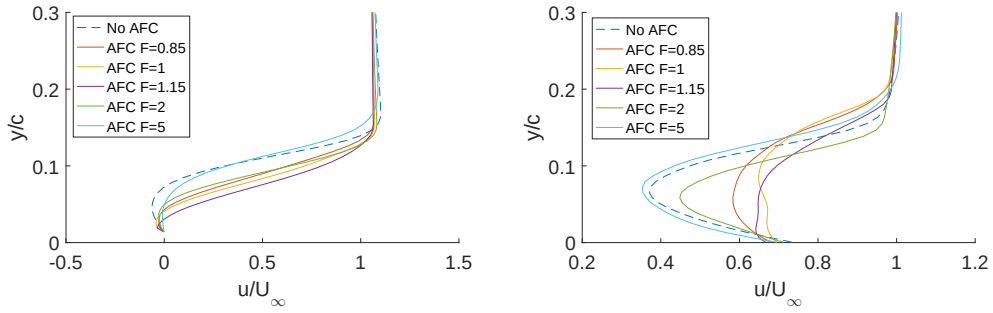

(c) $x/c = 0.9$ (d) $x/c = 1.2$

Figure 7.13: Streamwise velocity profiles (average flow) close to the airfoil surface (a,b,c) and in the near wake (d) for different F^+ values ($C_\mu = 0.005$) at AOA=6 deg

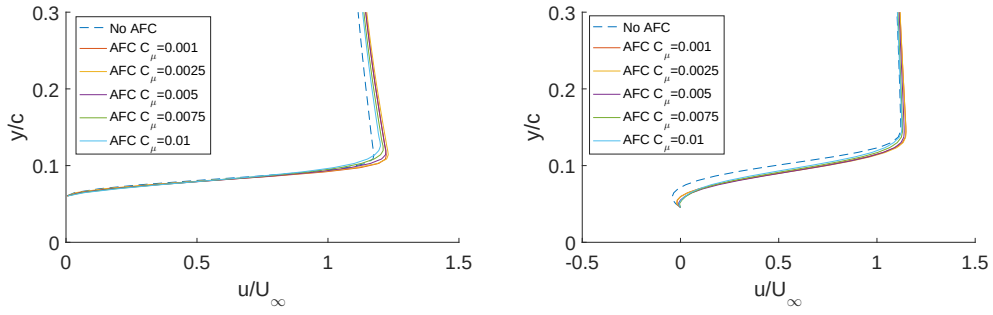

(a) $x/c = 0.3$ (b) $x/c = 0.6$

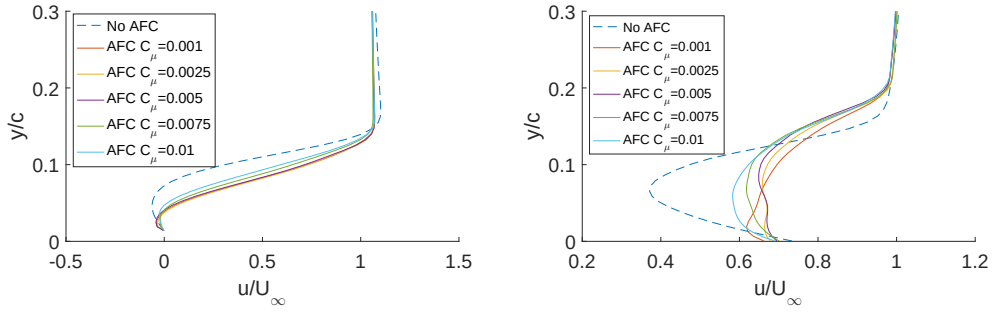

(c) $x/c = 0.9$ (d) $x/c = 1.2$

Figure 7.14: Streamwise velocity profiles (average flow) close to the airfoil surface (a,b,c) and in the near wake (d) for different C_μ values ($F^+ = 1$) at AOA=6 deg

Chapter 8: Project Management: Schedule, budget and communication

Any project requires some kind of management depending on its size. This project is not different and considerable management has been necessary to achieve the final results. In this chapter, four basic management areas of the project are explained: time (and scope), cost and communication. Other common areas of project management such as human resources and procurement do not apply to this study, while others such as risk and quality management are not detailed because of space limitations and importance to this study.

8.1 Time Management

In this section, the time management of the project is presented. First of all, the performed activities are detailed and, then, a schedule of the project is presented in a Gantt diagram.

8.1.1 Work Breakdown Structure (WBS)

The Work Breakdown Structure (WBS) of this project can be seen in Table 8.1. The WBS has been divided into two different levels of activity: the first level represents the major work packages of the project while the second one presents the detailed activities of each work package.

8.1.2 Project Schedule

The different tasks given in Table 8.1 can be also observed in the project schedule left in Figure 8.1. Both the starting and ending dates are detailed in the chart. Moreover, the different dependencies between the activities can be also observed. Finally, the two main milestones are also given: the report delivery day and the presentation day.

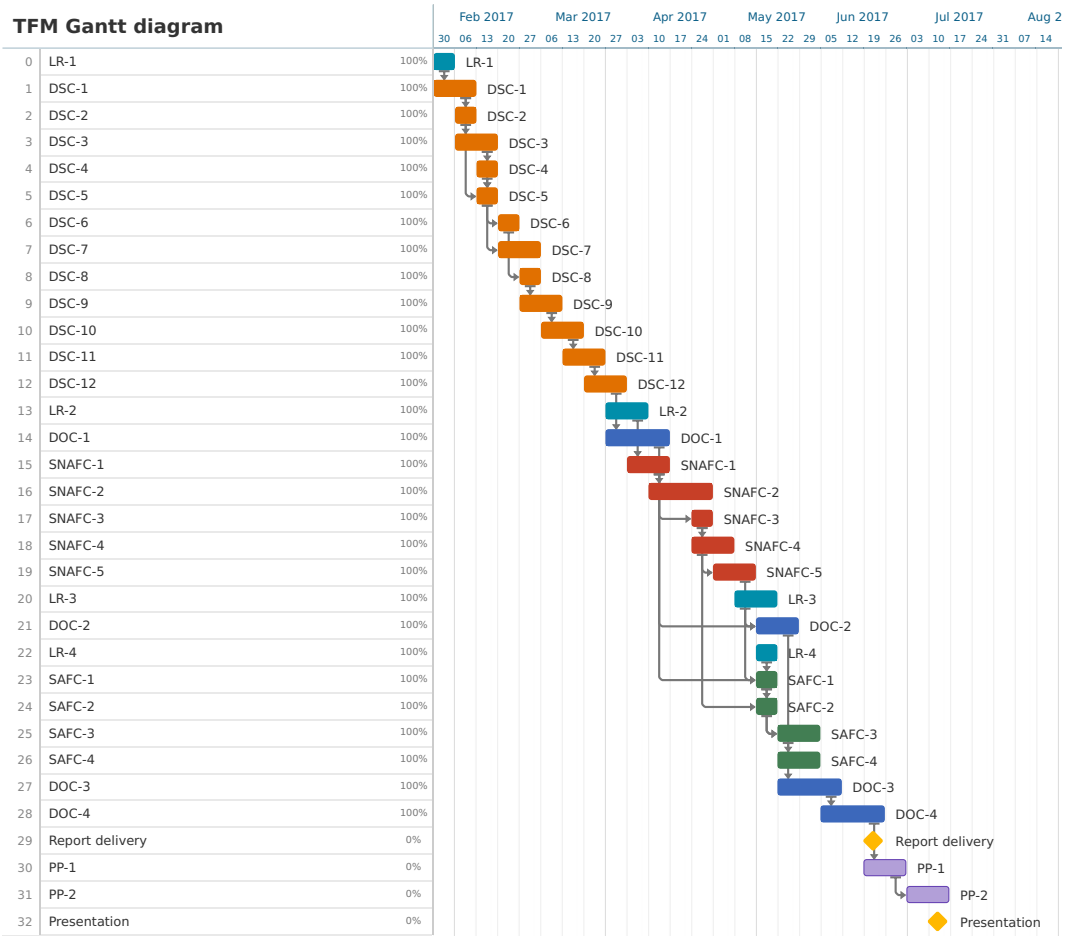

Figure 8.1: Gantt diagram of the project

WBS-ID	Description	Duration (h)
LR	**Literature Review**	**60**
LR-1	Formation on Navier-Stokes equations using spectro-consistent scheme	15
LR-2	Research on boundary layer control	20
LR-3	Research on Active Flow Control	15
LR-4	Research on Synthetic Jets	10
DSC	**Development of the spectro-consistent code**	**180**
DSC-1	Implement a staggered discretization (including halos)	15
DSC-2	Implement the basic matrices (M, L, G, Ω)	10
DSC-3	Implement the diffusive and convective operators	20
DSC-4	Implement the upwind scheme	5
DSC-5	Verify all the operators and matrices	15
DSC-6	Implement the pressure-velocity coupling solver	10
DSC-7	Add the Fourier solver	20
DSC-8	Implement the time integration	5
DSC-9	Validate the code for different velocity distributions	25
DSC-10	Convert the code to 3D	30
DSC-11	Validate the 3D code	10
DSC-12	Prepare and postprocess the simulations for the Taylor-Green problem	15
SNAFC	**Simulations without Active Flow Control**	**160**
SNAFC-1	Design of different meshes	40
SNAFC-2	Unsuccessful trials with Code_Saturne	60
SNAFC-3	Preparation of the cases with Alya	20
SNAFC-4	Monitoring of all the simulations	10
SNAFC-5	Post-processing and results analysis	30

Table 8.1: Work Breakdown Structure of the project

WBS-ID	Description	Duration (h)
SAFC	**Simulations with Active Flow Control**	**75**
SAFC-1	Redesign of the meshes to include the actuator	5
SAFC-2	Modification of the cases to include AFC	10
SAFC-3	Monitoring of the AFC simulations	20
SAFC-4	Post-processing and results analysis	40
DOC	**Documentation writing**	**110**
DOC-1	Draft 1: Layout of the report, review of literature, mathematical formulation, spectro-consistent section, computational setup, NACA 0012 airfoil simulations without Active Flow Control	35
DOC-2	Draft 2: Comments of draft 1 implemented, figures improved, NACA 0012 airfoil simulations with Active Flow Control, new sections added	30
DOC-3	Draft 3: Introduction, Project Management, Environmental impact, Conclusions, Appendices and abstract	30
DOC-4	Final version: Latest improvements implemented	15
PP	**Presentation preparation**	**45**
PP-1	Writing of the different slides	30
PP-2	Preparation of the project defense	15

Table 8.1: Work Breakdown Structure of the project (cont.)

8.2 Cost Management: Budget

Project Cost Management is primarily related to the cost of the resources needed to complete project activities [36]. Since the scope of this project is not too big and most part of the project is finished, cost estimating and cost budgeting are tightly linked and can be viewed as a single process.

8.2.1 Cost estimating

The cost estimating is a fundamental part of the cost management. It is the responsible of the confidence level of the whole budget and it has to clearly specify the main constraints and assumptions. First of all, the level of accuracy is explained. Then, the worksheets used to estimate the budget are presented.

Level of accuracy

To set the level of accuracy, several factors have to be considered such as the scope of the activities or magnitude of the project. Bearing in mind that the costs given herein are estimations, it does not have any sense to have a precision of centimes.

Thus, the level of accuracy of the project is set to 1%. Hence, the activity cost estimates are rounded up or down with a precision of 1%. In Table 8.2, some examples for different orders of magnitudes are presented:

Original estimate (€)	Rounded estimate (€)
8.68	8.68
51.24	51.2
258.65	259
4,521.15	4,520

Table 8.2: Examples of the level of accuracy

Finally, it is worth noting that the budget at completion follows the same criterion presented above.

Cost estimation worksheets

The estimation of the costs have been carried out with two tables: a list of parametric estimates, which it has a cost per unit, (see Table 8.3) and a list of three-point estimates (see Table 8.5). Then, the combination of these tables leads to the final budget of the project (see Table 8.6).

It is important to note that the depreciation method that has been used is **straight-line** for simplicity (other more complex methods, such as double declining-balance, could be also used).

Item	Cost per unit	Number of units	Cost estimate (€)
Human resources			
Junior engineer	14 €/h	630 h	8,820
Software			
Matlab Academic License	500 €/3y[1]	1/3 y	55.6
ANSYS Academic Research License	400 €/y[2]	1/3 y	133
Alya	0 €/y[3]	1/3 y	0
Electricity power			
Personal laptop	0.228 €/kWh [4]	53.55 kWh	12.2
Desktop PC 1 (simulations)	0.103 €/kWh [5]	243 kWh	25.0
Desktop PC 2 (simulations)	0.103 €/kWh	243 kWh	25.0
Depreciation			
Personal laptop	600 €/6y[6]	1/3 y	33.3
Desktop PC 1	2000 €/6y	1/3 y	111
Desktop PC 2	1500 €/6y	1/3 y	83.3

Table 8.3: List of parametric estimates

In order to compute the power consumption for the personal laptop and desktop PC, the items left in Table 8.4 have been considered.

For the personal laptop, a total of 80 W are consumed. Thus, considering that the laptop has been used during the entire duration of the project (630 h), a total of

[1] https://es.mathworks.com/pricing-licensing.html?prodcode=ML&intendeduse=edu

[2] https://webstore.illinois.edu/Shop/product.aspx?zpid=2564

[3] Permission has been granted due to an agreement between the *Alya* development team and the TUAREG (UPC)

[4] Households price at 2016 according to Eurostat: http://ec.europa.eu/eurostat/statistics-explained/index.php/File:Half-yearly_electricity_prices_(EUR).png

[5] Industry price at 2016 according to Eurostat: http://ec.europa.eu/eurostat/statistics-explained/index.php/File:Half-yearly_electricity_prices_(EUR).png

[6] According to IRS Publication 946 (https://www.irs.gov/uac/about-publication-946), computers have a class life of 6 years.

53.55 kWh have been consumed.

For the desktop PCs, a total of 135 W are consumed for each one. Approximately, each PC has been used uninterruptedly during half the project (75 days or 1800 hours). Thus, a total of 194.4 kWh have been consumed per computer.

Item	Power consumption (W)
Personal laptop	**80**
Laptop	45
LCD monitor	30
Router	5
Related cables	5
Desktop PC	**135**
Computer (8 cores)	120
Related cables	15

Table 8.4: Power consumption

Item	Optimistic cost (o €)	Most likely cost (m €)	Pessimistic cost (p €)	Weighting equation	Expected cost (€)
External hard disk for simulations	40	55	70	$\frac{o+4m+p}{6}$	55
USB stick (16 GB)	15	20	30	$\frac{o+4m+p}{6}$	20.8
Printing	80	130	200	$\frac{o+4m+p}{6}$	133

Table 8.5: List of three point estimates

8.2.2 Cumulative and total costs

Once the cost estimating is done (via the list of parametric estimates and three point estimates), hereafter the cumulative curve and budget at completion is presented. Then, the costs are also distributed into the main areas of the project by using percentages.

Area	Cost (€)
Human resources	8,820
Software	188.6
Electricity power	62.2
Depreciation	227.6
Others	208.8
Indirect Costs (25%)	2,376.8
Total	**11,884**

Table 8.6: Project budget divided by areas

Cumulative cost curve

The cumulative cost curve of the project can be seen in Figure 8.2. The main assumptions of this curve have been:

- Human resources, software and personal laptop consumption costs have been equally distributed among the total duration of the project (160 days).
- The punctual costs given in Table 8.5 are considered on the day when the purchase has been ordered.
- The power consumption of the desktop PCs has been imposed on the last part of the project.
- An indirect cost (25% of all the direct costs) has been added (distributed among the entire duration of the project).

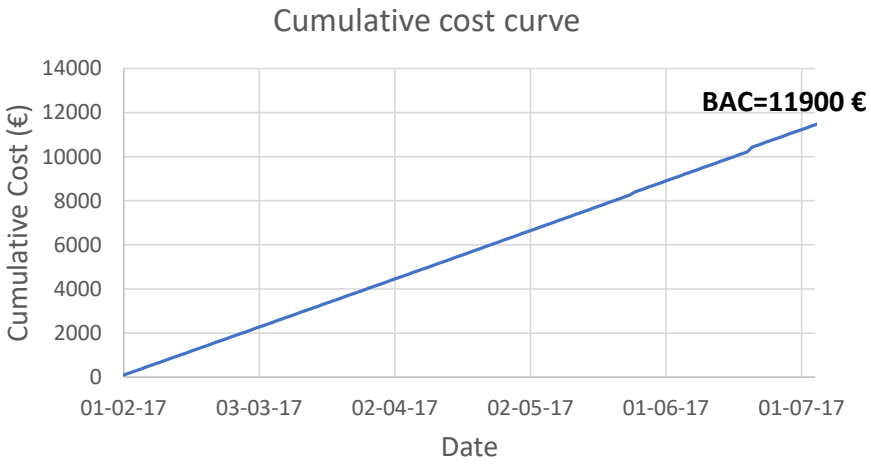

Figure 8.2: Cumulative cost curve

Budget at completion

To sum up, at the end of the project, a budget of 11,900€ has been expended. The main part of this budget corresponds to the human resources (74%) as it can be seen in Figure 8.3. Human resources is always one of the main contributors to any project/business. It is worth noting that no contingency reserve has been assumed since the project is already completed.

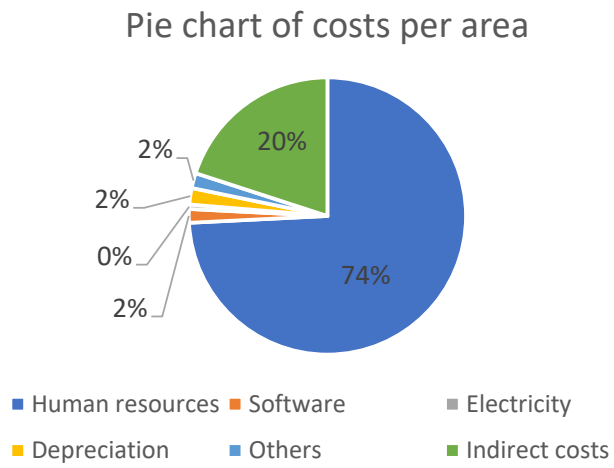

Figure 8.3: Pie chart of the costs per area

8.3 Communications Management

As said in reference [36], effective communication creates a bridge between the members of a project, who may have different background, levels of expertise, perspectives and interests.

The types of communication involved in this project have been:

- **Informal**: The information transmitted in this kind of communications is crucial for the day-to-day work to ensure correct development of the project.
  - E-mail (~ 100)
  - Face to face conversations
  - Phone calls
  - Messaging/mobile apps ($\sim 2,500$)
- **Formal**: This type of communication is adequate to provide information on regular intervals so that all the members of the team know the status and progress of the project.

- Status meetings
- Status/technical reports

Based on the needs and requirements of the advisors and author of this project, the plan communications management can be summarized in Table 8.7.

Communication Type	**Objective of the communication**	**Medium**	**Frequency**
Kick-off meeting	Introduce the project and review the main objectives and approaches	Face to face	Once
Status meetings	Review status of the project	Face to face/-Conference call	Monthly
Technical meetings	Discuss and develop technical solutions	Face to face	Weekly
Technical reports	Inform about partial results	E-mail	Weekly
Eventualities	Inform about eventual issues	E-mail, phone calls or mobile apps	As needed
Mid-term review	Evaluate the status of the project in terms of scope	Face to face	Once
Final meeting	Conclusion and evaluation of the project	Face to face	Once

Table 8.7: Communication management plan matrix

Chapter 9: Environmental impact

Reducing the environmental impact of air transportation is one of the most important public concerns in the aviation community. The USA with NextGen project [37] and NASA research activities [10], and Europe with SESAR [38] and Clean Sky [39] programs are pioneers in research projects aiming to address capacity, environmental impact, safety and economic aspects of aviation.

Active Flow Control is still a novel technology and there are few real-world applications implemented nowadays. However, it is expected that AFC applications will dramatically increase in the near future. As a consequence, several benefits regarding the environment will be obtained.

Active Flow Control enables optimization at off-design conditions and it has the potential for revolutionary advances in aerodynamic performance and maneuvering. Since the drag is reduced and there is more lift and circulation control, it is possible to reduce the noise and weight of the aircraft. An immediate consequence of the weight reduction is less fuel consumption, which enables to produce less emissions of dangerous substances for the environment.

To sum up, the technology studied in this project will produce benefits for the environment in the near future. However, no predictions of the actual environmental impact have been performed in this study since they are outside of the main scope.

Chapter 10: Future development planning

The results presented in this study are promising, but the scope of the current project is not limitless. However, it is strongly recommended to continue the study in a future project. This chapter aims to give some guidance on the future tasks and planning.

10.1 Description of the tasks

In order to achieve the aim of completely study the interaction of active flow control with the boundary layer of NACA airfoils, the following steps are foreseen to contribute towards this goal:

- **FS-1**: **3D simulations** for the NACA 0012 airfoil. This step is important since, at high angles of attack, the physics of the problem is not completely solved by using 2D simulations.
- **FS-2**: Implement some **turbulence models**. The current project has been centered on a laminar flow, but on some cases, turbulent models can produce different results.
- **FS-3**: Study the effect of the **Reynolds number** for the level of flow control over the NACA 0012 airfoil. It is expected that quite different results are obtained for higher values ($Re > 10^5$).
- **FS-4**: Analyze other **types of NACA airfoils**. For thicker airfoils, the type of stall is completely different: trailing edge stall is observed on these types of airfoils.
- **FS-5**: Include the **geometry of the synthetic jet** on the performed simulations. So far, synthetic jets have been simulated by implementing a certain boundary condition, but more exact results could be obtained by inserting the exact geometry of the synthetic jet. Obviously, this will imply a dramatic increase of computer power/time.
- **FS-6**: Test and validate the results of the numeric simulations with **wind tunnel experiments**.

10.2 Future schedule

While some of the tasks mentioned above are feasible within the following months, others require to invest a huge amount of hours. Thus, it is quite difficult to forecast how much time the aforementioned tasks will consume, but, in Figure 10.1, the reader can observe an approximate Gantt diagram of the future development of the study. The same nomenclature of previous section has been used.

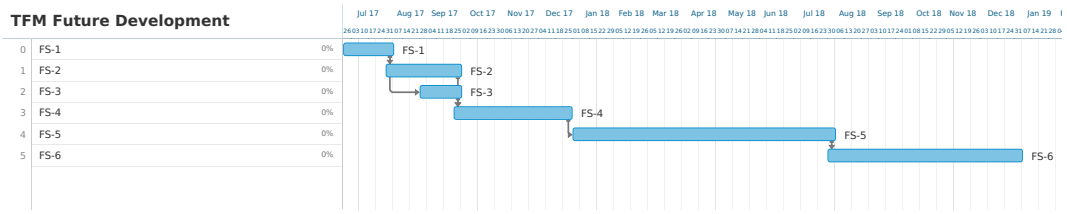

Figure 10.1: Gantt diagram of the future development of the study

Note that the end of the schedule lays on December 2018, which means that future developments could last up to one and a half year or more.

Conclusions and recommendations

This project shows that it is possible to apply active flow control (by means of synthetic jets) in order to reduce the size of the boundary layer. A systematic parametrization of the synthetic jet has been performed showing the optimal frequency and momentum coefficient in order to obtain the maximum level of flow control over the NACA 0012 airfoil.

Results demonstrate that by correctly positioning the jet actuator and, setting the optimal dimensionless frequency and momentum coefficient, the lift coefficient increases while the drag coefficient decreases producing a better lift-to-drag ratio. Achieving higher C_l/C_d ratios has multiple benefits such as better aerodynamic performance and circulation control, less fuel consumption and noise reduction.

It has been also shown that, for high angles of attack, it is necessary to perform 3D simulations in order to capture the entire physics of the problem. 2D simulations produce an excessive lift coefficient when dealing with high angles of attack.

Besides the aforementioned improvements due to the active flow control, it has been shown that spectro-consistent discretizations are one of the best options in the CFD field. Not only they preserve the energy between physical scales, but they also need less degrees of freedom than other schemes (i.e. upwind) to achieve the correct solution. The validity of spectro-consistent discretizations has been proved both developing a code from scratch, which is able to solve the Taylor-Green Vortices problem, and using *Alya* code to simulate the NACA 0012 airfoil with and without active flow control.

Although the promising results obtained in this study, the scope of the project is not limitless. Thus, it is strongly recommended to continue developing the study since several improvements can be implemented in the near future. From the steps mentioned in chapter 10, the most immediate and interesting one is to perform more 3D flow simulations, which will enable to correctly solve the flow at high angles of attack. It would be also interesting to simulate other types of airfoils and Reynolds numbers. These parameters could considerably affect the level of flow control over the boundary layer.

To sum up, the present study has enabled to analyze the interaction of a modeled synthetic jet with the laminar boundary layer of a NACA 0012 airfoil by using spectro-consistent discretizations. The results are promising for the nearest future and they lead to think that AFC will be certainly a prominent field of study for the next decade.

Bibliography

[1] Mark Sheplak and Louis N. Cattafesta III. Actuators for Active Flow Control. *Annual Review of Fluid Mechanics*, 43(1):247–272, 2011.

[2] Manel Soria. Notes to develop a spectroconsistent Navier-Stokes code. Technical report, Universitat Politècnica de Catalunya, 2017.

[3] Manel Soria. Solution of pressure-correction equations using discrete Fourier transform methods. Technical Report 2, Universitat Politècnica de Catalunya, 2001.

[4] CFD Online. https://www.cfd-online.com/, April 2017.

[5] Mariano Vázquez, Guillaume Houzeaux, Seid Koric, Antoni Artigues, Jazmin Aguado-Sierra, Ruth Arís, Daniel Mira, Hadrien Calmet, Fernando Cucchietti, Herbert Owen, Ahmed Taha, Evan Dering Burness, José María Cela, and Mateo Valero. Alya: Multiphysics engineering simulation toward exascale. *Journal of Computational Science*, 14:15–27, 2016.

[6] Ryoji Kojima, Taku Nonomura, Akira Oyama, and Kozo Fujii. Large-Eddy Simulation of Low-Reynolds-Number Flow Over Thick and Thin NACA Airfoils. *Journal of Aircraft*, 50(1):187–196, 2013.

[7] Jf Donovan, Ld Kral, and Aw Cary. Active flow control applied to an airfoil. *AIAA paper*, 1998.

[8] J. L. Gilarranz, L. W. Traub, and O. K. Rediniotis. A New Class of Synthetic Jet Actuators—Part II: Application to Flow Separation Control. *Journal of Fluids Engineering*, 127(2):377, 2005.

[9] J. L. Gilarranz, L. W. Traub, and O. K. Rediniotis. A New Class of Synthetic Jet Actuators—Part I: Design, Fabrication and Bench Top Characterization. *Journal of Fluids Engineering*, 127(2):367, 2005.

[10] Scott G Anders, William L Sellers, Anthon-E Washb, William L Sellers Illt, and Anthony E Washburn. Active Flow Control Activities at NASA Langley. *2Nd Aiaa Flow Control Conference*, (July 2004):1–21, 2004.

[11] Fang-Jenq Chen, Chungsheng Yao, George B. Beeler, Robert G. Bryant, and Robert L. Fox. Development of Synthetic jet actuators fof active flow control at NASA langley.pdf. *AIAA paper*, pages 1–12, 2000.

[12] John C. Lin, Marlyn Y. Andino, Michael G. Alexander, Edward A Whalen, Marc A Spoor, John T Tran, and Israel J. Wygnanski. An Overview of Active Flow Control Enhanced Vertical Tail Technology Development. *54th AIAA Aerospace Sciences Meeting*, (January):1–13, 2016.

[13] D. You and P. Moin. Active control of flow separation over an airfoil using synthetic jets. *Journal of Fluids and Structures*, 24(8):1349–1357, 2008.

[14] D C Mccormick. Boundary Layer Separation Directed Synthetic Jets Control with 38th Aerospace Sciences Meeting & Exhibit. In *38th Aerospace Sciences Meeting & Exhibit*, number AIAA 2000-0519, 2000.

[15] Avi Seifert and Latunia G Pack. Oscillatory Excitation of Unsteady ressible Flows over Airfoils at Flight Reynolds Numbers 37th AIAA Aerospace Sciences Meeting and Ex. *AIAA*, (c), 1999.

[16] Stephen B Pope. *Turbulent Flows*. Cambridge University Press, 2001.

[17] Charles L. Fefferman. Existence and smoothness of the Navier-Stokes equation. *The millennium prize problems*, (1):1–5, 2000.

[18] R. W. C. P. Verstappen and A. E. P. Veldman. Spectro-consistent discretization of Navier-Stokes : a challenge to RANS and LES. *Journal of Enginnering Mathematics*, 34:163–179, 1998.

[19] M. Soria, F. X. Trias, C. D. Pérez-Segarra, and A. Oliva. Direct numerical simulation of a three-dimensional natural-convection flow in a differentially heated cavity of aspect ratio 4. *Numerical Heat Transfer, Part A: Applications*, 45(7):649–673, 2004.

[20] A Mastellone, F Capuano, S Di Benedetto, and L Cutrone. Problem C3 . 5 Direct Numerical Simulation of the Taylor-Green Vortex at Re = 1600. Technical Report 1.

[21] J C R Hunt, a a Wray, and P Moin. Eddies, streams, and convergence zones in turbulent flows. *Center for Turbulence Research, Proceedings of the Summer Program*, (1970):193–208, 1988.

[22] Andrea D Beck and Gregor J Gassner. Numerical Simulation of the Taylor-Green Vortex at Re=1600 with the Discontinous Galerkin Spectral Element Method for well-resolved and underresolved scenarios. *1st International Workshop on High-Order CFD Methods*, 2012.

[23] J R Bull and A Jameson. Simulation of the Compressible Taylor Green Vortex using High-Order Flux Reconstruction Schemes. (June), 2014.

[24] James DeBonis. Solutions of the Taylor-Green Vortex Problem Using High-Resolution Explicit Finite Difference Methods. *51$ˆ{st}$ AIAA Aerospace Sciences Meeting including the New Horizons Forum and Aerospace Exposition*, (February):1–9, 2013.

[25] Frédéric Archambeau, Namane Méchitoua, and Marc Sakiz. Code Saturne: A Finite Volume Code for the Computation of Turbulent Incompressible Flows - Industrial Applications. *International Journal on Finite Volumes*, 1(1):http://www.latp.univ–mrs.fr/IJFV/spip.php?article3, 2004.

[26] Jordi Amat. Study for the Validation of Code_Saturne for Turbulent Flow Simulations. Bachelor's final project, Universitat Politècnica de Catalunya, June 2017.

[27] Md Mahbub Alam, Y. Zhou, H. X. Yang, H. Guo, and J. Mi. The ultra-low Reynolds number airfoil wake. *Experiments in Fluids*, 48(1):81–103, 2010.

[28] Dilek Funda Kurtulus. On the Unsteady Behavior of the Flow Around NACA 0012 Airfoil with Steady External Conditions at Re = 1000. 7(3):301–326, 2015.

[29] Y. Hoarau, M. Braza, Y. Ventikos, D. Faghani, and G. Tzabiras. Organized modes and the three-dimensional transition to turbulence in the incompressible flow around a NACA0012 wing. *Journal of Fluid Mechanics*, 496:63–72, 2003.

[30] Lluís Jofre, Oriol Lehmkuhl, Jordi Ventosa, F. Xavier Trias, and Assensi Oliva. Conservation Properties of Unstructured Finite-Volume Mesh Schemes for the Navier-Stokes Equations. *Numerical Heat Transfer, Part B: Fundamentals*, 65(1):53–79, 2014.

[31] O. Lehmkuhl, G. Houzeaux, M Avila, H. Owen, M.Vazquez, and D. Mira. A low dissipation finite element scheme for the large eddy simulation on complex geometries. *In 19h International Conference on Finite Elements in Flow Problems - FEF 2017*, 2017.

[32] OpenFOAM Foundation. Open FOAM. *URL: http://creativecommons.org/licenses/by-sa/3.0/(la st accessed 07.08. 2012)*, (February):212, 2014.

[33] I Rodríguez, O Lehmkuhl, R Borrell, and A Oliva. Direct numerical simulation of a NACA0012 in full stall. *International Journal of Heat and Fluid Flow*, 43:194–203, 2013.

[34] D. Duran, I. Rodríguez, M. Soria, and O. Lehmkuhl. Boundary layer flow control using synthetic jets on the flow over a NACA 0012 airfoil. In *Proceedings of the 17th International Conference on Computational and Mathematical Methods in Science and Engineering, CMMSE 2017*, number 4-8 July, 2017.

[35] Sebastian D. Goodfellow, Serhiy Yarusevych, and Pierre E. Sullivan. Momentum coefficient as a parameter for aerodynamic flow control with synthetic jets. *AIAA Journal*, 51(3):623–631, 2013.

[36] Project Management Institute. *A guide to the project management body of knowledge (PMBOK ® guide)*. 2013.

[37] FAA. NextGen Implementation Plan. *Vasa*, (August), 2013.

[38] SESAR Consortium. European ATM Master Plan - Edition 2. *The Roadmap for Sustainable Air Traffic Management*, (October):1–100, 2012.

[39] Eurocontrol. Clean sky joint undertaking. annual implementation plan 2014. Technical Report CS-GB-2013-13-12, December 2013.

[40] J Scheffel. On Analytical Solution of the Navier-Stokes Equations On Analytical Solution of the. Technical report, 2001.

[41] C Ross Ethier and D A Steinman. Exact fully 3d navier-stokes solutions for benchmarking. 19(March):369–375, 1994.

[42] G. I. Taylor. On the Decay of Vortices in a Viscous Fluid. *Philosophical Magazine*, (January 2014):37–41, 1923.

Appendix A: Mathematical derivations

This chapter is devoted to prove some mathematical relations of the Navier-Stokes equations, which, because of space restrictions, are not included in the main body of the report.

A.1 Derivative of energy

As said in section 4.1, the total discrete kinetic energy can be defined as:

$$|\boldsymbol{u}|^2 = \boldsymbol{u}^t \Omega \boldsymbol{u} \tag{A.1.1}$$

Using the Chain rule, the derivative of the total discrete kinetic energy is:

$$\frac{d}{dt}(\boldsymbol{u}^t \Omega \boldsymbol{u}) = \boldsymbol{u}^t \left(\Omega \frac{d\boldsymbol{u}}{dt}\right) + \left(\frac{d\boldsymbol{u}^t}{dt}\Omega\right)\boldsymbol{u} = \boldsymbol{u}^t \left(\Omega \frac{d\boldsymbol{u}}{dt}\right) + \left(\Omega \frac{d\boldsymbol{u}}{dt}\right)^t \boldsymbol{u} \tag{A.1.2}$$

By using Equation 4.1.1, it is known that:

$$\Omega \frac{d\boldsymbol{u}}{dt} = -C(\boldsymbol{u})\boldsymbol{u} - D\boldsymbol{u} - \Omega G\boldsymbol{p} \tag{A.1.3}$$

Replacing this expression on Equation A.1.2 and bearing in mind that Ω is a diagonal matrix:

$$\frac{d}{dt}(\boldsymbol{u}^t \Omega \boldsymbol{u}) = -\boldsymbol{u}^t \left(C\boldsymbol{u} + D\boldsymbol{u} + \Omega G\boldsymbol{p}\right) - \left(C\boldsymbol{u} + D\boldsymbol{u} + \Omega G\boldsymbol{p}\right)^t \boldsymbol{u} \tag{A.1.4}$$

Using the algebraic property that $(AB)^t = B^t A^t$, the following expression can be obtained:

$$\frac{d}{dt}(\boldsymbol{u}^t \Omega \boldsymbol{u}) = -\boldsymbol{u}^t C\boldsymbol{u} - \boldsymbol{u}^t C^t \boldsymbol{u} - \boldsymbol{u}^t D\boldsymbol{u} - \boldsymbol{u}^t D^t \boldsymbol{u} - \boldsymbol{u}^t \Omega G\boldsymbol{p} - (\Omega G\boldsymbol{p})^t \boldsymbol{u} \tag{A.1.5}$$

Thus, the derivative of the total discrete kinetic energy can be expressed as follows:

$$\frac{d}{dt}(\boldsymbol{u}^t \Omega \boldsymbol{u}) = -\boldsymbol{u}^t (C + C^t)\boldsymbol{u} - \boldsymbol{u}^t (D + D^t)\boldsymbol{u} - (\boldsymbol{u}^t \Omega G\boldsymbol{p} + \boldsymbol{p}^t G^t \Omega^t \boldsymbol{u}) \tag{A.1.6}$$

A.2 Proof of the relation between kinetic energy dissipation rate and enstrophy

From the Navier-Stokes equations (see Equation 3.0.5), the kinetic energy dissipation rate ϵ is obtained as:

$$\epsilon = -\frac{dE_k}{dt} = 2\frac{\mu}{\rho}\frac{1}{\Omega}\int_\Omega \boldsymbol{S} : \boldsymbol{S} d\Omega \tag{A.2.1}$$

The aim of this section is to verify that the kinetic energy dissipation rate can be also expressed with the following expression for an incompressible flow:

$$\epsilon = 2\frac{\mu}{\rho}\varepsilon \tag{A.2.2}$$

Where the enstrophy ε can be expressed as:

$$\varepsilon = \frac{1}{\Omega}\int_\Omega \frac{\boldsymbol{\omega}\cdot\boldsymbol{\omega}}{2} d\Omega \tag{A.2.3}$$

Thus, in the end, the following statement has to be proved:

$$\boldsymbol{S} : \boldsymbol{S} \stackrel{?}{=} \frac{\boldsymbol{\omega}\cdot\boldsymbol{\omega}}{2} \tag{A.2.4}$$

A.2.1 Expression of the strain rate tensor

First of all, the left-hand side of Equation A.2.4 has to be developed. Each component of the strain rate tensor is defined as follows:

$$S_{ij} = \frac{1}{2}\left(\frac{\partial u_i}{\partial x_j} + \frac{\partial u_j}{\partial x_i}\right) \tag{A.2.5}$$

Then, the strain rate tensor can be expressed with the following tensor:

$$\boldsymbol{S} = \frac{1}{2}\begin{bmatrix} 2\frac{\partial u}{\partial x} & \frac{\partial v}{\partial x}+\frac{\partial u}{\partial y} & \frac{\partial w}{\partial x}+\frac{\partial u}{\partial z} \\ \frac{\partial u}{\partial y}+\frac{\partial v}{\partial x} & 2\frac{\partial v}{\partial y} & \frac{\partial w}{\partial y}+\frac{\partial v}{\partial z} \\ \frac{\partial u}{\partial z}+\frac{\partial w}{\partial x} & \frac{\partial v}{\partial z}+\frac{\partial w}{\partial y} & 2\frac{\partial w}{\partial z} \end{bmatrix} \tag{A.2.6}$$

The operation $\boldsymbol{S} : \boldsymbol{S}$ is equivalent to the trace (sum of diagonal elements) of $S \cdot S^T$. It is also equivalent to $S_{ij}S_{ij}$. In any case, the result of such operation is:

$$\begin{aligned}\boldsymbol{S} : \boldsymbol{S} = \left(\frac{\partial u}{\partial x}\right)^2 + \left(\frac{\partial v}{\partial y}\right)^2 + \left(\frac{\partial w}{\partial z}\right)^2 + \frac{1}{4}\Bigg[\left(\frac{\partial v}{\partial x}+\frac{\partial u}{\partial y}\right)^2 + \left(\frac{\partial w}{\partial x}+\frac{\partial u}{\partial z}\right)^2 + \\ \left(\frac{\partial u}{\partial y}+\frac{\partial v}{\partial x}\right)^2 + \left(\frac{\partial w}{\partial y}+\frac{\partial v}{\partial z}\right)^2 + \left(\frac{\partial u}{\partial z}+\frac{\partial w}{\partial x}\right)^2 + \left(\frac{\partial v}{\partial z}+\frac{\partial w}{\partial y}\right)^2\Bigg]\end{aligned} \tag{A.2.7}$$

Further developing the expression leads to:

$$\begin{aligned}\boldsymbol{S} : \boldsymbol{S} = \left(\frac{\partial u}{\partial x}\right)^2 + \left(\frac{\partial v}{\partial y}\right)^2 + \left(\frac{\partial w}{\partial z}\right)^2 + \frac{\partial u}{\partial y}\frac{\partial v}{\partial x} + \frac{1}{2}\left(\frac{\partial u}{\partial y}\right)^2 + \frac{\partial u}{\partial z}\frac{\partial w}{\partial x} + \frac{1}{2}\left(\frac{\partial u}{\partial z}\right)^2 + \\ \frac{1}{2}\left(\frac{\partial v}{\partial x}\right)^2 + \frac{1}{2}\left(\frac{\partial v}{\partial z}\right)^2 + \frac{\partial v}{\partial z}\frac{\partial w}{\partial y} + \frac{1}{2}\left(\frac{\partial w}{\partial x}\right)^2 + \frac{1}{2}\left(\frac{\partial w}{\partial y}\right)^2\end{aligned} \tag{A.2.8}$$

Since, in an incompressible flow, the continuity equation can be expressed as $\frac{\partial u}{\partial x}+\frac{\partial v}{\partial y}+\frac{\partial w}{\partial z}=0$, computing the square power of continuity equation leads to the fact that the first three terms of the previous equation can be expressed as:

$$\left(\frac{\partial u}{\partial x}\right)^2+\left(\frac{\partial v}{\partial y}\right)^2+\left(\frac{\partial w}{\partial z}\right)^2=-2\frac{\partial u}{\partial x}\frac{\partial v}{\partial y}-2\frac{\partial u}{\partial x}\frac{\partial w}{\partial z}-2\frac{\partial v}{\partial y}\frac{\partial w}{\partial z} \tag{A.2.9}$$

Thus, the final expression of $\boldsymbol{S}:\boldsymbol{S}$ is:

$$\begin{aligned}\boldsymbol{S}:\boldsymbol{S}=-\frac{\partial u}{\partial y}\frac{\partial v}{\partial x}+\frac{1}{2}\left(\frac{\partial u}{\partial y}\right)^2-\frac{\partial u}{\partial z}\frac{\partial w}{\partial x}+\frac{1}{2}\left(\frac{\partial u}{\partial z}\right)^2+\frac{1}{2}\left(\frac{\partial v}{\partial x}\right)^2-\frac{\partial v}{\partial z}\frac{\partial w}{\partial y}+\\ \frac{1}{2}\left(\frac{\partial v}{\partial z}\right)^2+\frac{1}{2}\left(\frac{\partial w}{\partial x}\right)^2+\frac{1}{2}\left(\frac{\partial w}{\partial y}\right)^2\end{aligned} \tag{A.2.10}$$

A.2.2 Expression of the enstrophy

After having developed the left-hand side of Equation A.2.4, the right-hand side is computed. The vorticity is defined as follows:

$$\boldsymbol{\omega}=\nabla\times\boldsymbol{u}=\begin{vmatrix}\hat{i} & \hat{j} & \hat{k}\\ \frac{\partial}{\partial x} & \frac{\partial}{\partial y} & \frac{\partial}{\partial z}\\ u & v & w\end{vmatrix}=\left(\frac{\partial w}{\partial y}-\frac{\partial v}{\partial z},\frac{\partial u}{\partial z}-\frac{\partial w}{\partial x},\frac{\partial v}{\partial x}-\frac{\partial u}{\partial y}\right) \tag{A.2.11}$$

Then, the product to compute is equal to:

$$\begin{aligned}\frac{\boldsymbol{\omega}\cdot\boldsymbol{\omega}}{2}=-\frac{\partial u}{\partial y}\frac{\partial v}{\partial x}+\frac{1}{2}\left(\frac{\partial u}{\partial y}\right)^2-\frac{\partial u}{\partial z}\frac{\partial w}{\partial x}+\frac{1}{2}\left(\frac{\partial u}{\partial z}\right)^2+\frac{1}{2}\left(\frac{\partial v}{\partial x}\right)^2-\frac{\partial v}{\partial z}\frac{\partial w}{\partial y}+\\ \frac{1}{2}\left(\frac{\partial v}{\partial z}\right)^2+\frac{1}{2}\left(\frac{\partial w}{\partial x}\right)^2+\frac{1}{2}\left(\frac{\partial w}{\partial y}\right)^2\end{aligned} \tag{A.2.12}$$

The above expression is exactly the same as the one derived in subsection A.2.1. Thus, we have proved that $\boldsymbol{S}:\boldsymbol{S}=\frac{1}{2}\boldsymbol{\omega}\cdot\boldsymbol{\omega}$ for an incompressible flow, which is the same as stating that $\epsilon=2\frac{\mu}{\rho}\varepsilon$.

Appendix B: Implementation of the Fourier solver

In this section, the Fourier solver mentioned in subsection 4.2.2 is explained. The aim is to solve an equation of the following type of equation (Poisson equation):

$$L \cdot X = B \tag{B.0.1}$$

Since the grid is uniform in the three directions, the matrix L can be expressed as:

$$L = [a, c, d, b, a, c, d]_p \tag{B.0.2}$$

Where a represents the east-west two diagonals (1st component), b the main diagonal, c the north-south diagonals (2nd component) and d the up-down diagonals (3rd component).

In order to have a full-working 3D Fourier solver, three main Fourier functions have been implemented:

- Fourier 1D
- Fourier 2D
- Fourier 3D

All these steps have been tested and validated for random B vectors, which verify that the sum of all their components is 0. The obtained X vector has been compared to the one obtained by doing the inverse of L.

Fourier 1D solves a tridiagonal matrix $A = [a, b, a]_p$, whose eigenvalues can be computed as follows:

$$\begin{gathered} \lambda_1 = b + 2a \\ \lambda_{2i} = \lambda_{2i+1} = -4a \sin^2\left(\frac{i\pi}{N}\right) + b + 2a \qquad i = 1 \ldots N/2 - 1 \\ \lambda_N = b - 2a \end{gathered} \tag{B.0.3}$$

Then, we can apply the following transformation that allows to express the compo-

nents of x in the basis of the eigenvectors of A [3]:

$$\begin{aligned}
\bar{x}_1 &= \frac{2}{N}\sum_{i=1}^{N} x_i \\
\bar{x}_{2\nu} &= \frac{2}{N}\sum_{i=1}^{N} x_i \cos\left(\nu i \frac{2\pi}{N}\right) \qquad \nu = 1 \ldots N/2-1 \\
\bar{x}_{2\nu+1} &= \frac{2}{N}\sum_{i=1}^{N} x_i \sin\left(\nu i \frac{2\pi}{N}\right) \qquad \nu = 1 \ldots N/2-1 \\
\bar{x}_n &= \frac{2}{N}\sum_{i=1}^{N} x_i (-1)^i
\end{aligned} \tag{B.0.4}$$

The previous transformation is called the *direct transformation*, which can be evaluated with a cost $\mathcal{O}(N)$ using the Fast Fourier Transform. The expression of the *direct transformation* is:

$$\bar{x} = Q^{-1}x \tag{B.0.5}$$

The details of the *inverse transformation* can be found in [3], but it can be expressed as:

$$x = Q\bar{x} \tag{B.0.6}$$

Then, the steps to implement the Fourier solver in one-dimensional problems are:

1. Obtain $\bar{B}$, so that the system is transformed into:

$$A \cdot x = B \rightarrow Q^{-1}Ax = Q^{-1}B = \bar{B} \tag{B.0.7}$$

   This can be also expressed as:

$$Q^{-1}AQ\bar{x} = \bar{B} \tag{B.0.8}$$

2. Find the eigenvalues of A with Equation B.0.3. It is known that $Q^{-1}AQ = \lambda$, so:

$$\lambda\bar{x} = \bar{B} \tag{B.0.9}$$

3. Since the previous system is already diagonalized, we can go row by row doing the following operation:

$$\bar{x}_i = \frac{\bar{B}}{\lambda_i} \tag{B.0.10}$$

4. Since the sum of B is 0, there is a singularity. This can be solved by imposing the first component of $\bar{x}$ to be 0, for instance.

5. Finally, x is obtained applying the inverse transformation:

$$x = Q\bar{x} \tag{B.0.11}$$

When more than one dimension is solved using Fourier, we can choose if one dimension is solved with TDMA while the other with Fourier. In the current code, the option to mix solvers is available. However, herein, the pure Fourier solver is explained.

For solving **Fourier 2D**, the following steps are taken:

1. Loop through rows (y direction) computing $\bar{B}$ and the eigenvalues of each row. Parameters a (east-west neighbors) and b (main diagonal) are necessary. By doing this step, the dependency with east-west neighbors has been removed. We are left with a block tridiagonal matrix depending on the north-south neighbors.

2. Call the subroutine 'fourier1D' (explained above) with the found eigenvalues, $\bar{B}$ and the parameter c (north-south neighbors) for each column. Thus, we have completely diagonalized the matrix. $\bar{x}$ is obtained.

3. Apply the inverse transformation for each row.

An analogous procedure (with more loops) is followed for **Fourier 3D**:

1. Loop through $z-y$ planes removing the dependency with east-west neighbors by computing $\bar{B}$ and λ from parameters a and b.

2. Call the subroutine 'fourier2D' (explained above) with the found eigenvalues, $\bar{B}$, and parameters c (north-south neighbors) and d (up-down neighbors). This is called iterating through the x direction. $\bar{x}$ is obtained.

3. Apply the inverse transformation for each $z-y$ plane.

As it can be seen, though the procedure is similar when increasing dimensions, things get complex when an extra dimension is added. Thus, it is of great importance to develop the code step by step and testing that each piece is working separately.

In Figure B.1, the cost per time step of the Fourier solver can be seen depending on the mesh size. These results have been obtained from an implementation of Fourier solver in C code. In Matlab, the CPU time is slower. However, it can be clearly observed that the cost is $\mathcal{O}(N)$, while without using Fourier solver would be $\mathcal{O}(N^3)$.

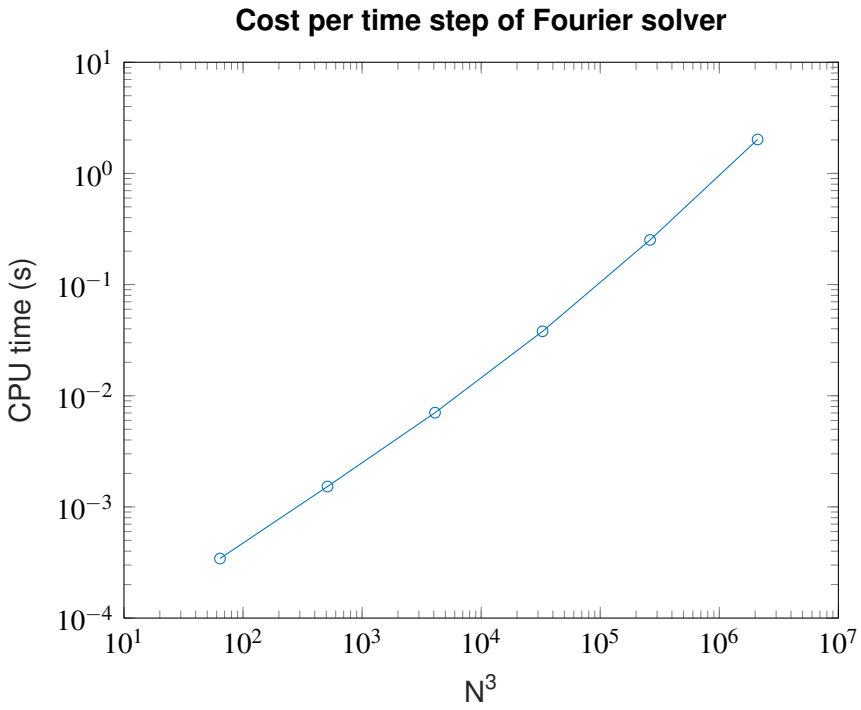

Figure B.1: Cost per time step of Fourier solver (Source: [3])

Appendix C: Validation of the spectro-consistent CFD code

The aim of this section is to validate the spectro-consistent CFD code developed from scratch, which is explained in chapter 4.

In a 3D flow, it is really complicated to find an analytical solution for a periodic velocity distribution (see [40] for a detailed study on analytical solution of NS equations). Thus, to validate the implemented code, it is necessary to use a 2D velocity distribution, which is known to have an analytical solution. The following initial velocity distribution is such that the unsteady, convective, pressure and diffusive terms in the Navier-Stokes equations are all non-zero (see [41]):

$$\begin{aligned} u &= \cos(2\pi x)\sin(2\pi y) \\ v &= -\sin(2\pi x)\cos(2\pi y) \\ w &= 0 \end{aligned} \tag{C.0.1}$$

The analytical solution of such velocity distribution is:

$$\begin{aligned} u_{an} &= e^{-8\pi^2 \nu t}\cos(2\pi x)\sin(2\pi y) \\ v_{an} &= -e^{-8\pi^2 \nu t}\sin(2\pi x)\cos(2\pi y) \\ w_{an} &= 0 \\ p_{an} &= -e^{-16\pi^2 \nu t}\rho\frac{\cos(4\pi x)+\cos(4\pi y)}{4} \\ E_{an} &= \frac{e^{-16\pi^2 \nu t}}{4} \end{aligned} \tag{C.0.2}$$

As said in reference [41], Equation C.0.2 constitutes a 2D Navier-Stokes solution in which the unsteady terms balance the diffusive terms, while the convective terms balance the pressure gradient. This solution has been used for 2D benchmarking since Taylor derived it [42].

C.1 2D validation

The first validation consists on obtaining the analytical solution for the full 2D velocity distribution mentioned above. To do so, the following inputs are given:

- 16x16x16 mesh
- Domain from 0 to 1 meters in all directions

- $\rho = 1.225 kg/m^3$
- $\mu = 0.01 Pa \cdot s$
- $\mathbb{S} = 0$
- $CFL = 0.1$
- Fourier solver used
- Consistent convective scheme

The simulation is finished when the squared mean error of velocities between the current iteration and the previous one is less than $10^{-8} m/s$.

After 960 iterations, the comparison of the basic variables respect to the analytical solution can be seen in Figure C.1. Note that there is no velocity in the z direction. Thus, there is only vorticity in that direction (it goes out of the plane where velocities have some value). **Although the mesh is coarse, the numerical values are quite similar to the analytical solution.**

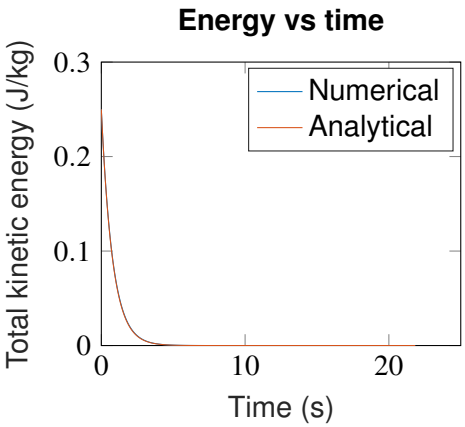

(a) Total kinetic energy

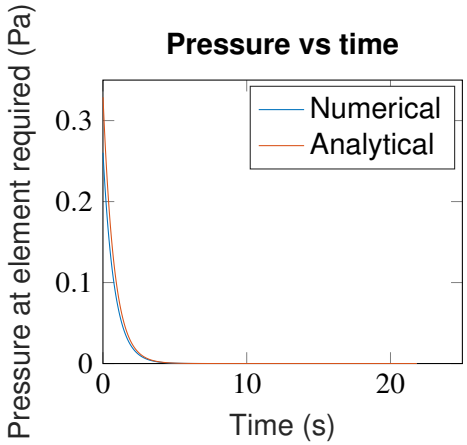

(b) Pressure at index (2,2,2)

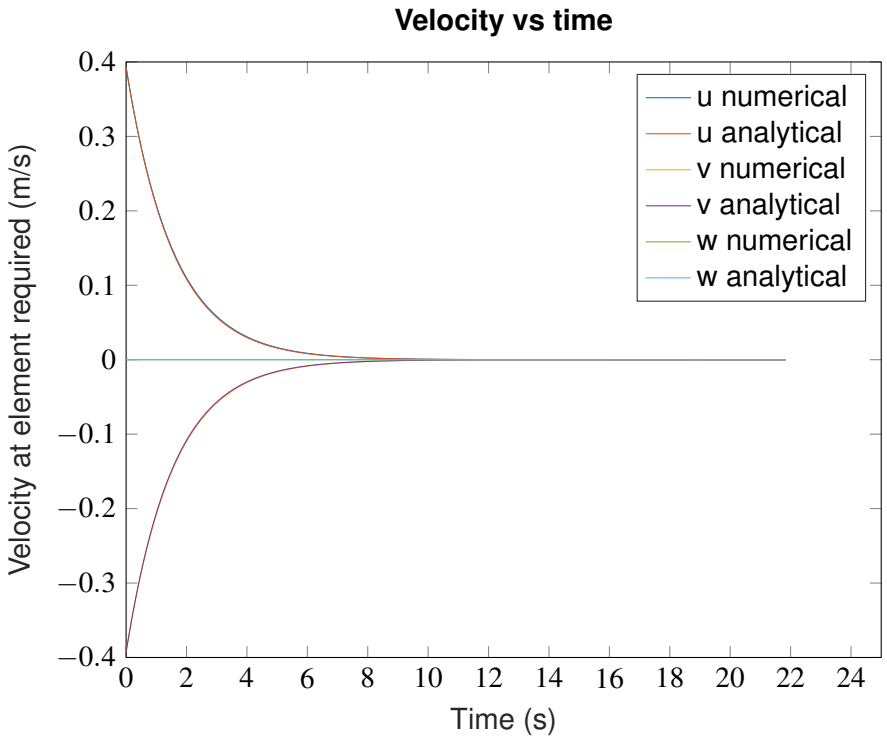

(c) Velocity at staggered indeces (2,2,2)

Figure C.1: Comparison of numerical and analytical solution for a full 2D flow

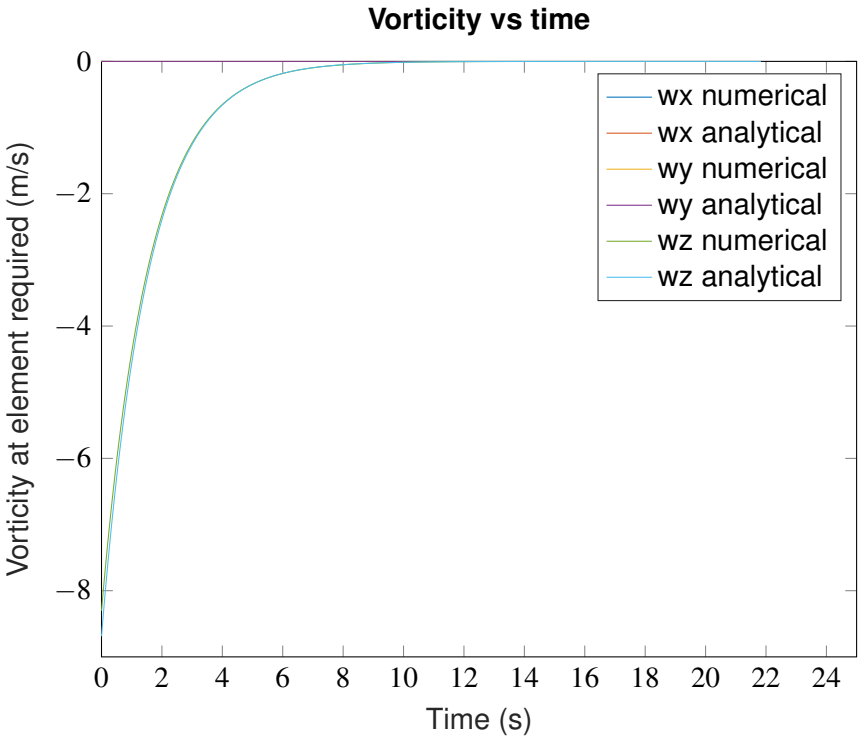

(d) Vorticity at centered index (2,2,2)

Figure C.1: Comparison of numerical and analytical solution for a full 2D flow (cont.)

C.2 3D validation through 2D rotations

So far, only a 2D solution has been validated. It could be the case that when setting a full 3D velocity distribution, some error arises. In order to avoid these errors, the previous 2D solution is rotated in all the possible directions.

A code has been developed so that these rotations are automatized via a rotation matrix on both position and velocity. The first column represents the rotated x component (position or velocity), the second one is the rotated y component and the last one is the rotated z component:

$$T_{pos} = \begin{bmatrix} x & y & z \\ x & z & y \\ y & x & z \\ y & z & x \\ z & x & y \\ z & y & x \end{bmatrix} \tag{C.2.1}$$

$$T_{vel} = \begin{bmatrix} u & v & w \\ u & w & v \\ v & u & w \\ v & w & u \\ w & u & v \\ w & v & u \end{bmatrix} \tag{C.2.2}$$

Where the non-rotated velocity distribution is the same as the one indicated in section C.1. There are two loops: i_v and i_p. First, the velocity is rotated as follows:

$$\begin{aligned} u_{rot} &= T_{vel}(i_v, 1) \\ v_{rot} &= T_{vel}(i_v, 2) \\ w_{rot} &= T_{vel}(i_v, 3) \end{aligned} \tag{C.2.3}$$

Then, the positions are rotated:

$$\begin{aligned} x_{rot} &= T_{pos}(i_p, 1) \\ y_{rot} &= T_{pos}(i_p, 2) \\ z_{rot} &= T_{pos}(i_p, 3) \end{aligned} \tag{C.2.4}$$

Finally, the positions are input as arguments of the velocity functions:

$$\begin{aligned} u_{rot} &= u_{rot}(x_{rot}, y_{rot}, z_{rot}) \\ v_{rot} &= v_{rot}(x_{rot}, y_{rot}, z_{rot}) \\ w_{rot} &= w_{rot}(x_{rot}, y_{rot}, z_{rot}) \end{aligned} \tag{C.2.5}$$

Note that, theoretically, 36 rotations are possible (a double loop through the two aforementioned rotation matrices). However, not all rotations verify the necessary condition of *divergence-free* neither they are momentum solutions. In these cases, the rotation is discarded. In the end, a total of **12 rotations are valid**. These 12 rotations should give the same error if compared with the analytical 2D solution (in absolute value). This means, that all the rotations should fit in one of the three possible lines (corresponding to each velocity component) regardless the size of the grid.

To record the absolute difference with the analytical solution, probes on the staggered indices (2,2,2) are used. The same conditions as section C.1 have been used.

As it can be seen in Figure C.2a, Figure C.2b and Figure C.2c, all the differences (absolute value) in time go in one of the three possible lines. Note that there is always a null curve corresponding to the non-rotated w component, which is 0. The other two curves correspond to the rotated x or y component of the velocity.

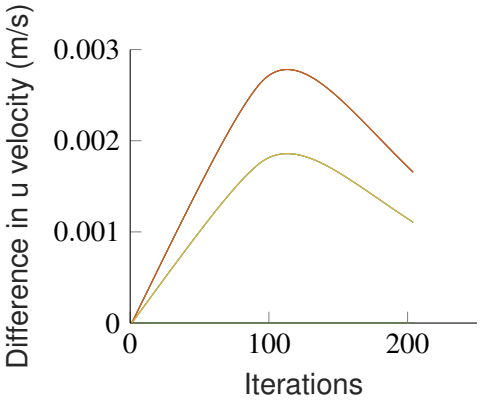

(a) Difference in u velocity for the different rotations

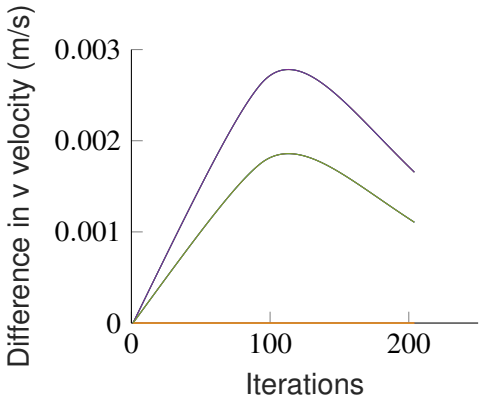

(b) Difference in v velocity for the different rotations

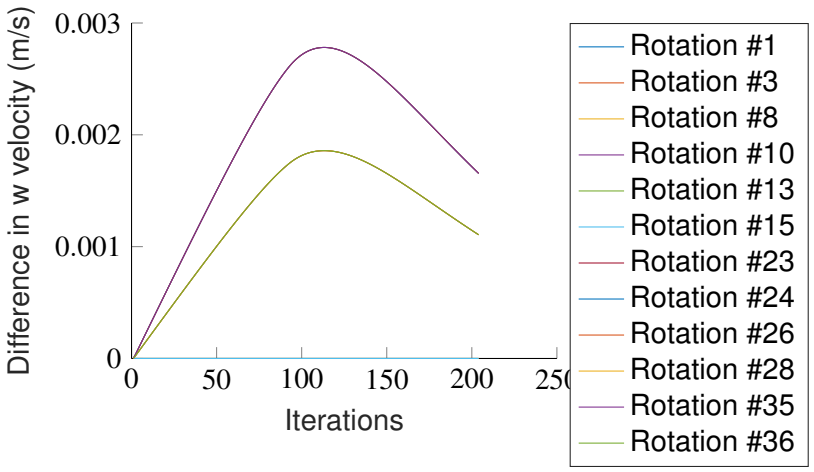

(c) Difference in w velocity for the different rotations

Figure C.2: Differences between numerical and analytical velocities for different rotations

C.3 Comparison of convective schemes

Finally, in order to see that the scheme is really spectro-consistent, we have to verify that, independently of the mesh size, the different terms of Equation 4.1.1 (multiplied by the velocity and integrated in the whole domain) are as follows:

- Term arising from pressure must be 0.
- Convective term has to be 0 since no energy is lost because of convection.
- Diffusive term has to be equal to the temporal term.

As it can be seen in Figure C.3, all the above statements are verified when using the spectro-consistent scheme. On the other hand, when using an upwind scheme (see Figure C.4), the convective term is not 0 since energy is lost when changing scale size.

Then, in an upwind scheme, the convective and diffusion term have to compensate the temporal one. These simulations have been run with a coarse 4x4x4 mesh to show that this is independent of the mesh size.

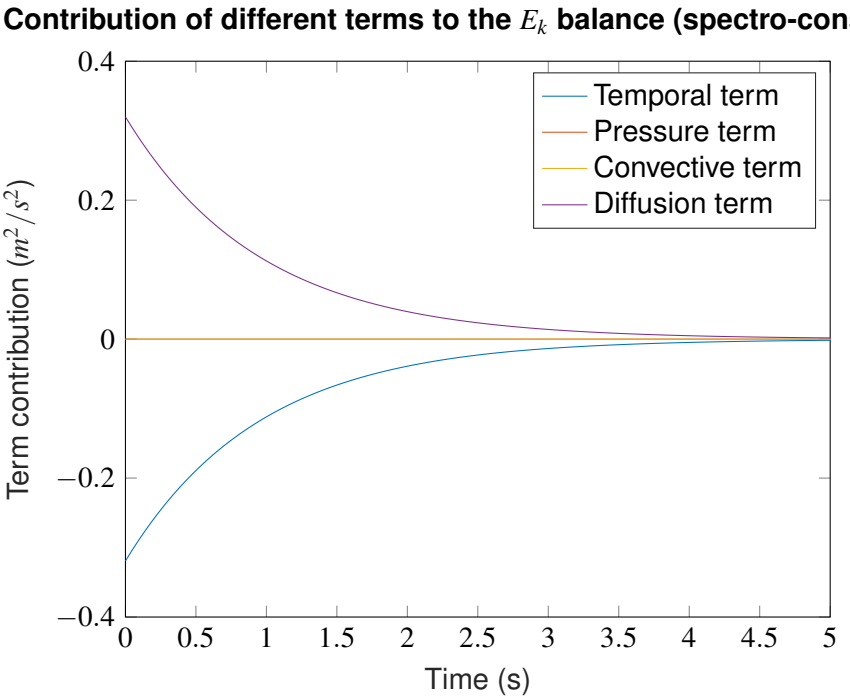

Figure C.3: Contribution of the different terms (Spectro-consistent scheme)

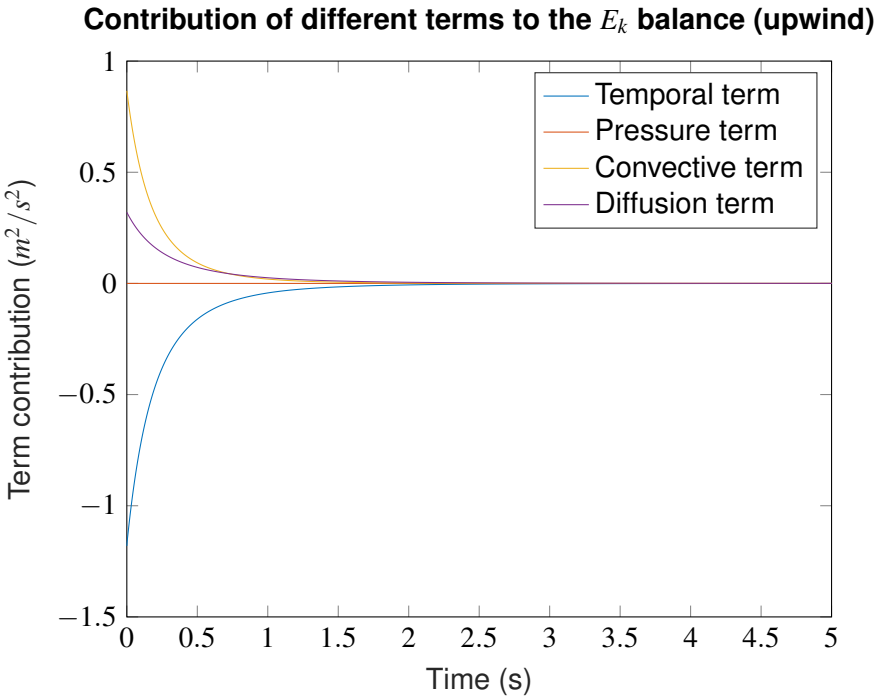

Figure C.4: Contribution of the different terms (Upwind scheme)